Spatio-temporal observation of dynamical structures in order-disorder phenomena and phase transitions via Ultrafast Electron Diffraction

PAR

Francesco PENNACCHIO

EPFL

ÉCOLE POLYTECHNIQUE
FÉDÉRALE DE LAUSANNE

Suisse
2018

DECLARATION

I, the undersigned, declare that this thesis has been composed by me alone, and that the work presented in this thesis is my own, or where it is the work of others, they are duly credited. Furthermore I confirm that this work has not been submitted for any other degree or professional qualification than this doctorate. Some of the research herein has already been published or it is undergoing a revision process, as detailed at the beginning of each chapter.

Lausanne, February 2018

Francesco Pennacchio

It is impressed on our minds in infancy that a certain arbitrary symbol indicates an existing fact; if this same association of emblem and reality is reiterated at the preparatory school, insisted upon at college, and pronounced correct at the university; symbol and fact - or supposed fact - becomes so intimately blended that it is extremely difficult to disassociate them, even when reason and personal observation teaches us they have no true relationship.

So it is with the conventional galloping horse. We have become so accustomed to see it in art that it has imperceptibly dominated our understanding, and we think the representation to be unimpeachable, until we throw all our preconceived impressions on one side, and seek the truth by independent observations from Nature herself.

Eadweard Muybridge – Animals in motion [1]

Dedicated to the loving memory of Emanuela Cucchi.
02.07.1956 – 18.11.1991

To be is to be perceived.
And so to know thyself is only possible through the eyes of the other.
The nature of our immortal lives is in the consequences of our words and
deeds that go on apportioning themselves throughout all time.

Our lives are not our own.
From womb to tomb, we are bound to others,
past and present, and by each crime and every kindness
we birth our future.

Sonmi 451 – The Cloud Atlas [2]

ACKNOWLEDGMENTS

Figure 0.1: Forest - Cascades du Herisson - Jura. © Francesco Pennacchio

On a more personal note. I would love to say my special thanks to Sash, Pauline and Justine. To Curdin, Dora, Margaux, Jérémy, Mélanie and Suzanne - and to photography. And an affectionate thank is addressed to Caterina, Maria and Beatrice: a joyful dinner on a balcony or a shared breakfast after a nightshift can make a day. Thank you all because mighty trees need good fellows to share the horizon with.

To Marta, Federico, Luca, Camilla, Berardo, Cecilia, Maria, Beatrice and Michael: there is always a place in the world where we can arrange a beer or a road trip, and that's precious. Thank you because we shaped our branches and trunks together all along these years.

I would like to send some loving thanks to Giulia, Giulia, Marta, Lorenzo, Andrea, Tommaso, Valentina, Davide, Letizia, Elisabetta and Emanuele, because healthy trees need solid roots.

Dulcis in fundo: family. I would like to thank my parents, Angelo e Maria whose silent presence gave me much more strength they could imagine. To Emanuela: I really hope you're proud of the person I have become. A tribute is due to my grandmother Maria, because you are the strongest and most inspirational person I have ever met. To my siblings Elia, Giuditta & Giulia, because I have missed you so much. Thank you all because even the tallest among the redwoods had been a sprout once.

ABSTRACT

The development of ultrafast time-resolved techniques in the last decades allowed the direct observation of out-of-equilibrium transient states and dynamical processes up to then hidden in many different fields, ranging from chemistry to solid state physics and biology. Amongst them, Ultrafast Electron Diffraction (UED) allows the retrieval of direct information on the structural dynamics of solids, surfaces, nanostructures and molecular crystals with femtosecond (10^{-15} s) and atomic (Å, 10^{-10} m) temporal and spatial resolution.

The UED setup implemented at EPFL is characterised by 30 keV, 20 kHz pulses containing up to 10^5 electrons each and can work in both transmission and reflection geometry. A sub-500 fs time resolution in transmission geometry is achieved by means of a radio frequency compression cavity for electrons. This time resolution, combined with the high transverse coherence of our electrons, allowed the observation of order-disorder phenomena in 2D-supracrystals of functionalised gold nanoparticles. The insurgence of ligand-dependent photomechanical stiffness phenomena was observed and characterised in the aforementioned systems. In reflection geometry, the time resolution suffered severe limitations - especially when probing mm^2-sized samples - due to the velocity mismatch between the pump and the probe beam. To overcome this limitation, an optimal optical front tilt scheme for the pump pulse was designed, implemented and characterised, thus disclosing a sub-500 fs temporal resolution also in reflection geometry.

The newly achieved time resolution allowed the direct visualisation of ultrafast structural dynamics in two systems of current interest: graphite and magnetite. In graphite, the selective excitation via electron-phonon coupling of a subset of phonon modes called Strongly Coupled Optical Phonons - with a characteristic timescale of $\approx$ 500 fs - was experimentally resolved. In magnetite, the photoinduction of the Verwey phase transition was achieved, unveiling phase segregation intermediate states during the transformation and disclosing structural differences between the photoinduced and the thermal phase transition mechanism.

KEYWORDS:

Ultrafast Electron Diffraction, order-disorder phenomena, functionalised Au nanoparticles, 2D-supracrystals, pulse front tilting, graphite, Strongly Coupled Optical Phonons, magnetite, Verwey transition, phase segregation.

RESUMÉ

Au cours des dernières décennies, le développement de techniques ultra-rapides a permis l'observation directe d'états transitoires et de processus dynamiques dans différents domaines allant de la chimie à la physique de l'état solide et la biologie. Parmi ces techniques, la diffraction électronique ultra-rapide (DEU) a permis d'obtenir des informations sur la dynamique structurelle de solides, surfaces, nanostructures et cristaux moléculaires avec une résolution temporelle de l'ordre du femto secondes et spatiale de l'ordre atomique. L'installation DEU mise en place à l'EPFL est caractérisée par des impulsions de 30 KeV, 20 kHz, chacune contenant jusqu'à 10^5 électrons, et peut fonctionner en géométrie de transmission et de réflexion. Une résolution temporelle inférieure à 500 fs est obtenue au moyen d'une cavité de compression pour électrons à radio fréquence. Cette résolution temporelle a permis l'observation de phénomène d'ordre-désordre dans des supracristaux bidimensionnels de nanoparticules d'or recouvertes d'alcanothiols. L'apparition de phénomènes de rigidité photomécaniques dépendants de ligands a aussi été observée et caractérisée dans les systèmes déjà mentionnés. Au contraire, de sévères limitations de résolution temporelle ont été observés en géométrie de réflexion, spécialement avec des échantillons de taille de l'ordre du mm^2, à cause de la non-concordance entre la vitesse du pump et celle du probe. Pour palier à ce problème, un design expérimental pour l'inclinaison du front optique du pump a été développé, implémenté et caractérisé, ceci permettant d'obtenir une résolution temporelle inférieure à 500 fs aussi avec cette géométrie. La résolution temporelle nouvellement obtenue a permis la visualisation directe de dynamiques structurelles dans deux systèmes d'intérêt actuel : graphite et magnétite. Dans le graphite, l'excitation sélective par couplage électron-phonon d'un sous-ensemble de modes phononiques appelés Strongly Coupled Optical Phonons, caractérisés par une échelle temporelle de $\sim$ 500 fs, a été vérifiée. Dans la magnétite, la photo-induction de la transition de phase de Verwey a été observée, révélant des états intermédiaires de ségrégation de phase pendant la transformation et dévoilant des différences structurelles entre les mécanismes de transition de phase thermiques et photo-induits.

MOTS CLÉS :

Ultrafast Electron Diffraction, phénomènes d'ordre-désordre, Au NPs recouvertes d'alcanothiols, 2D-supracrystaux, tilting du front optique, graphite, Strongly Coupled Optical Phonons, magnétite, transition de Verwey, segregation de phase.

ZUSAMMENFASSUNG

Die Entwicklung von zeitaufgelösten Techniken in den letzten Jahrzehnten hat es ermöglicht, aus dem Gleichgewicht geratene Zustände und bis danhin unbekannte dynamische Prozesse in verschiedenen Forschungsgebieten von Chemie bis zu Festkörperphysik und Biologie zu erforschen. Ultrafast Electron Diffraction (UED) ermöglicht einen faszinierenden Einblick in die Strukturdynamik von Feststoffen, Oberflächen, Nano- und Kristallstrukturen mit zeitlicher und räumlicher Auflösung von Femtosekunden (10^{-15} s) und atomaren Grössen (Å, 10^{-10} m).

Der experimentelle UED Aufbau an der EPFL verwendet 30 keV, 20 kHz Impulsen mit je bis zu 10^5 Elektronen und kann sowohl in einer Transmissions- als auch in einer Reflektionsgeometrie benutzt werden. Eine zietliche Auflösung unter 500 fs in Transmissionsgeometrie wird durch den Einsatz eines Hochfrequenzkompressionshohlraums erreicht. Zusammen mit einer hohen transversalen Kohärenz erlaubt diese zeitliche Auflösung das Beobachten von Ordnung-Unordnung Phänomenen in 2D-Suprakristallen von Gold-Nanopartikeln mit Alkanthiolbeschichtungen. In den zuvor genannten Systemen wurde ebenfalls die Erscheinung von mechanischer Steifigkeit erforscht und charakterisiert.

Im Vergleich zeigt eine typische Reflektionsgeometrie starke Einschränkungen in der zeitlichen Auflösung - insbesondere bei der Analyse von Proben im mm^2 Bereich - aufgrund der Geschwindigkeitsdiskrepanz zwischen dem Pump - und Probe-Puls. Diese Einschränkung wurde durch die Entwicklung, Implementierung und Optimierung eines optischen front tilt Schemas für die Pumppulse gelöst, wodurch eine temporäre Auflösung von weniger als 500 fs auch in der Reflektionsgeometrie erreicht wurde.

Die so erreichte zeitliche Auflösung ermöglichte die direkte Visualisierung von ultraschnellen Strukturdynamiken von zwei besonders relevanten Systemen: Graphit und Magnetit. In Graphit wurde so die selektive Anregung einer Teilgruppe von Phonon Formen namens Strongly Coupled Optical Phonons mittels Elektron-Pho- non Kopplung experimentell aufgelöst. In Magnetit, die Photoinduktion des Verwey Phasenübergangs erzielt werden und so intermediäre Zustände der Phasensegragation während der Umwandlung sowie strukturelle Unterschiede zwischen dem photoinduzierten und dem thermischen Phasenübergangsmechanismus enthüllt werden.

CONTENTS

ACRONYMS

UED   Ultrafast Electron Diffraction

URHEED   Ultrafast Reflection High-Energy Electron Diffraction

LT   Low Temperature

MRI   Magnetic Resonance Imaging

MRT   Magnetic Resonance Tomography

LUMES Laboratory for Ultrafast Microscopy and Electron Scattering

EPFL   École Polytechnique Fédérale de Lausanne

CCD   Charge-Coupled Device

MCP   Micro Channel Plate

UV   UltraViolet

FWHM   Full Width at Half Maximum

NPs   nanoparticles

SFG   Sum Frequency Generation

TEM   Transmission Electron Microscopy

SLM   Sphere Lattice Model

SuNMiL Supramolecular Nanomaterials and Interfaces Laboratory

CCF   Cross-Correlation Function

FT   Fourier Transform

RAI   Radial Average Intensity

INTRODUCTION

Paris, Musée du Louvre, 2nd floor, room 61.

Here we can admire the profuse production of Théodore Géricault, the author of the renowned painting *The Rate of the Medusa*. Among the exposed artworks, a painting realised in 1821 represents a party of jockeys riding their horses, racing for the Derby of Epsom. There, the horses are portrayed with both front and hind legs extended outwards, as it was common habit in that period.

June 19, 1878. Palo Alto, California.

The British photographer Edward Muybridge succesfully resolves the movement of a galloping horse and unveils the instant where the horse's legs are simultaneously lifted, which happens at a different configuration than the one represented in the painting. It is the first time in history where a time resolution better than the human eye is achieved.

The object of his observation - how the horse's legs are lifted - is certainly not reminded as a scientific breakthrough. The developed technique, instead, is considered as a milestone in imaging technology and it gave the input toward new media able to access information hidden to the human eye, due to its limited time resolution. In the wake of this development, a technological effort toward the achievement of progressively shorter observable time resolutions have been made during the last 150 years.

In the last decades, the technological development in pulsed lasers drastically pushed time resolution limits down to the femtosecond timescale (10^{-15} s) and allowed the direct observation of ultrafast phenomena in many different fields, ranging from chemistry to solid state physics and biology. The direct visualisation of phenomena happening at this timescale allowed a strong deepening in their comprehension, and thus the possibility to exert a control over them. Ultrafast Electron Diffraction occupies a primary role in this research for the visualisation of ephemeral states of matter, due to its surface sensitivity and high cross section as respect to light elements.

In this thesis, I demonstrate the extreme versatility of Ultrafast Electron Diffraction, whose insight have ranged from the characterisation of 2D-supracrystals of alkanethiol-capped gold nanoparticles and the disclosure of order-disorder phenomena to the observation of phase transitions in crystals. I present the design, implementation and characterisation of a pulse front tilt scheme able to enhance the time resolution of our experimental setup, now able to resolve phenomena in the sub-500 fs regime. Finally, the thesis contains the results of

UED investigation on two systems of actual interest: graphite and magnetite.

OUTLINE

The outline of the material presented in this thesis is the following:

- In Chapter 1 a general introduction on the technique is provided. Some principles of diffractive phenomena are reported, with a focus on Ultrafast Electron Diffraction. A complete description of our experimental setup is also contained.

- Chapter 2 focuses on the time resolved experiment performed with UED in transmission geometry on 2D-supracrystals of alkane-thiol-capped gold nanoparticles. The possibility to unveil hidden symmetries and to probe order-disorder and local stiffness phenomena is also reported.

- Chapter 3 contains the design, implementation and characterisation of the optimal pulse front tilting for our setup, developed in order to enhance the time resolution of our experimental setup in the sub-500 fs regime in reflection geometry for $\lambda = 800$ nm. A complete overview of the application of tilting schemes is provided, together with an innovative iterative approach, aimed to identify the best parameter configuration during the design of the system. The design of a tilting scheme for $\lambda = 400$ nm is also contained.

- In Chapter 4, we present the result of photoexcitation in a graphite bulky sample. We report the observation of the ultrafast population of a subset of phonons, the so-called Strongly Coupled Optical Phonons and their successive phonon-phonon relaxation. The direct observation of the ∼500 fs decay in the intensity confirms the newly achieved time resolution of our setup.

- Chapter 5 focuses on the Verwey transition in magnetite. A general panoramic over the research oriented on the topic is provided. UED studies at room temperature and below the Verwey temperature are presented, together with an experiment where the phase transition was thermally induced. Evidence of the photoinduced phase transition are shown, and a discrepancy between the photoinduced and the thermal transition is observed. A model is also proposed to explain this discrepancy.

ULTRAFAST ELECTRON DIFFRACTION

1.1 PRINCIPLES OF DIFFRACTION

When a radiation is characterized by a wavelength λ which is comparable to the interatomic distances in a crystalline structure, every atom in the structure behaves as a scattering centre of the incident radiation. The scattered radiation can be described as a spherical wave originating from the scatterer atom (see figure 1.1).

These spherical waves interact mutually, creating constructive or destructive interferences according to their propagation direction. The sum of the constructive interactions of the scattered waves composes a diffraction pattern, which is the fingerprint of the probed material and it strongly relates to its crystallographic features, *e.g.* the unit cell geometry, the interatomic distances and the distribution of atoms in the cell. In mono-crystalline samples, the pattern is characterised by well defined and localised diffraction features, called Bragg peaks, while polycrystalline substrates, or powders, show a diffraction pattern composed by concentrical circumferences. Those features are due to the statistical distribution of the families of planes with respect to the probing wave, whose interaction originates cones of constructive interference. Their intersection with the plane of the detector is the reason of the circular features called Debye-Scherrer rings.

A geometrical explanation of these phenomena was provided by Lawrence and Henry Bragg in 1913 [4] as follows: for an interference to be constructive, the difference in the pathway among waves
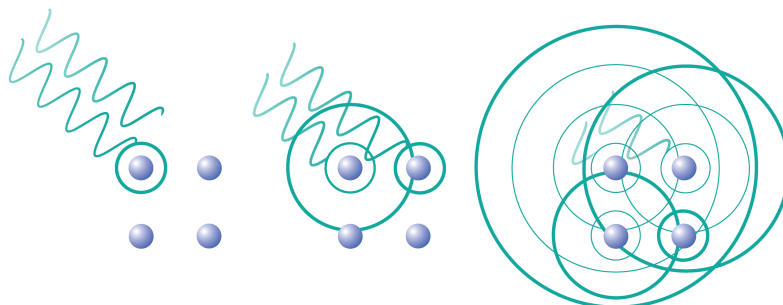
Figure 1.1: Schematic of spherical waves originated by the interaction between matters and radiation of wavelength comparable to the interatomic distances in the investigated sample. Reprinted with modification from Christophe Dang Ngoc Chan, under GNU Free Documentation Licence.
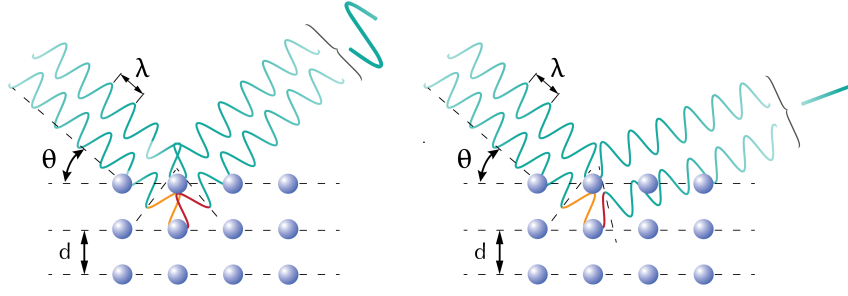
Figure 1.2: Visual representation of the Bragg diffraction condition, with a comparison among constructive and destructive interference. Reprinted with modification from Christophe Dang Ngoc Chan, under GNU Free Documentation Licence.

diffracted by different lattice planes of the same family has to be equal to an entire multiple of the incoming radiation wavelength λ. This concept is rendered in fig. 1.2, where the geometrical conditions for both the constructive and the destructive interference case are reported. The mathematical relation describing this principle, called Bragg condition, is

$$2d \sin \theta = n\lambda \tag{1.1}$$

where d is the spacing among lattice planes belonging to the same family, θ is the angle between the incident radiation and the crystallographic planes and n is an integer number $\in \mathbb{N}$ and defines the considered order of diffraction.

In the three dimensional real space, the position of atoms in a unit cell is defined by a given vector $\vec{r_g} = m\vec{a} + n\vec{b} + o\vec{c}$ where $\{m,n,o\} \in \mathbb{Z}$, and $\vec{a}$, $\vec{b}$ and $\vec{c}$ are the primitive vectors that describe the periodicity of the crystal.

In reciprocal space vectors $\vec{g}$ are defined by $e^{i\vec{g}\cdot\vec{r_g}} = 1$ and $\vec{g} = h\vec{a}^* + k\vec{b}^* + l\vec{c}^*$, where $\{m,n,o\} \in \mathbb{Z}$ and $\vec{a}^*, \vec{b}^*$ and $\vec{c}^*$ are the primitive vectors of the reciprocal lattice. Reciprocal lattice vectors are normal to the lattice planes, which have a spacing $d_{hkl} = 2\pi / |\vec{g}|$.

Defining then the quantities $\Delta\vec{k} = \vec{k} - \vec{k_0}$ where $\vec{k_0}$ is the wavevector of the incoming wave and $\vec{k}$ the wavevector of the outgoing wave, and the so-called shape factor

$$S(\vec{\Delta k}) = \sum_{\vec{r_g}}^{lattice} e^{-i\vec{\Delta k}\cdot\vec{r_g}} \tag{1.2}$$
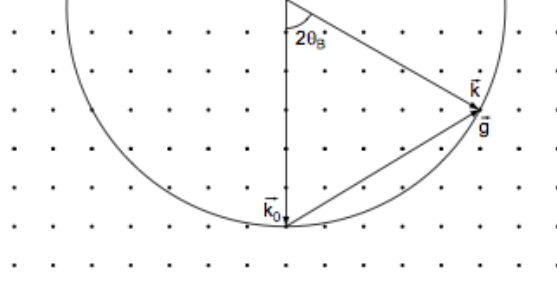
Figure 1.3: Ewald sphere construction in the reciprocal space that shows when the Laue condition is fulfilled. Picture taken from [6].

generated from the quantum mechanic theory of scattered waves, the Laue condition for constructive interference can be defined as [5]

$$\Delta \vec{k} = \vec{g} \tag{1.3}$$

This condition can be explained by the construction of the Ewald sphere. The tip of the incoming wavevector $\vec{k_0}$ is placed over a point of the reciprocal lattice, and the tail of the same vector is the center of the Ewald sphere. The radius of the sphere equals $|\vec{k_0}| = 2\pi/\lambda$, where λ is the wavelength of the incoming radiation. In elastic scattering conditions, *i.e.* $|\vec{k_0}| = |\vec{k}| = k$, the tip of every possible scattered vector $\vec{k}$ will also lie on the Ewald sphere. However, constructive interference phenomena only happen for determined value of $2\theta_B$, when the Laue condition is fulfilled - in geometrical terms, when the Ewald sphere intersects a node of the reciprocal lattice, as rendered in in fig. 1.3.

Despite their different origin, the equivalence of the two aforementioned formulations can be demonstrated, using $|\vec{g}| = 2\pi/d$, $\Delta k = 2k \sin \theta_B$, $|\vec{k}| = 2\pi/\lambda$ and applying the opportune substitutions.

1.2 ULTRAFAST ELECTRON DIFFRACTION

The advent of femtosecond laser sources made dynamical studies with femtosecond timescale resolution accessible, opening the possibility to investigate transitional nonequilibrium structures which are critical to the understanding of dynamic phenomena and systems, e.g. transition state in chemical reaction, structural transformation in biomolecules or phase transitions in solids [7–9]. Many different complementary techniques have been developed, to further investigate these transitory states of matters, ranging from optical spectroscopies [10, 11] to electron microscopy [12, 13] and many others.

Amongst them, Ultrafast Electron Diffraction (UED) employs an optical pump and electron probe configuration and exhibits a temporal resolution of hundreds of femtoseconds and a spatial resolution down to the atomic scale. Experiments in UED can be performed

in transmission and reflection geometries. In transmission geometry both the pump pulse and the probing electrons are directed to the nm-thin sample at a perpendicular geometry, with the electrons collected behind the sample. In reflection geometry, the probing electron beam is sent on the sample surface with a grazing angle, while the pump impinges almost perpendicularly on the sample. So far, UED has been successfully used in a variety of systems and configurations [14–16]. For example, it allowed to unveil the intermediate structures involved in many transitional phenomena in condensed matter, such as phase transitions [17–21], interfacial phase transition [22], electron-lattice coupling [23, 24] and anisotropic lattice excitation [25]. More recently, it allowed the investigation and characterisation of low dimensional nanoscale systems, unveiling order-disorder interplay in organic-inorganic 2D supracrystals [26], anisotropic expansion in carbon nanotubes [27], energy transport and dissipation in nanostructures [28–30], rippling dynamics of free-standing graphene [31] and to probe bulk and surface heating mechanisms [32].

1.2.1 *Information from a time-resolved diffraction experiment*

In time-resolved diffraction experiments, changes in intensity, position, width and shape of the diffraction features contain the signature of structural dynamics in the observed sample [14]. The intensity of a diffraction feature is directly related to the scattering centers in the unit cell through the structure factor

$$I \propto |F_{hkl}|^2 \tag{1.4}$$

defined as

$$F_{hkl} = \sum_{1}^{n} f_n e^{2\pi i (hx+ky+lz)} \tag{1.5}$$

where n is the number of atoms in the unit cell, f_n is the atomic scattering factor, h, k and l are the indexes of the considered reflections and x, y and z are the fractional coordinates of each atom in the unit cell. Thus, the intensity of a diffraction feature can be subject to variation as a result of incoherent thermal motions, coherent lattice vibrations or phase transitions.

Incoherent thermal motion of the atoms in a crystalline structure can be described by the Debye-Waller DW factor $W(T)$, formulated as:

$$ln\frac{I}{I_0} = -2W(T) = -\mathbf{s}^2\langle u^2\rangle/3 \tag{1.6}$$

where I and I_0 are the observed diffraction intensity with and without thermal displacements, $\mathbf{s}$ the scattering vector for a particular diffraction feature, and $\langle u^2\rangle$ the mean-square harmonic displacement of the atoms in a unit cell.

The position of the peak in electron diffraction is given by the aforementioned Bragg condition:

$$2d^{[hkl]}\sin\theta = n\lambda_e \tag{1.7}$$

where λ_e is the de Broglie wavelength associated to the electrons ($= 6.98 \times 10^{-12}$ m for 30 keV electrons) and $d^{[hkl]}$ is the interplane separation along the $[hkl]$ direction. Thus, homogeneous deformations (expansion/contraction) of the lattice will be mirrored in the position of the observed diffraction feature. The consequent modification of the scattering vector s of the Bragg peak can be described according to the relation:

$$\frac{s(t) - s_0}{s_0} \approx \frac{d^{[hkl]}(t) - d_0^{[hkl]}}{d_0^{[hkl]}} = \epsilon^{[hkl]} \tag{1.8}$$

where the subscript o indicates the corresponding quantities before the lattice modifications, and $\epsilon^{[hkl]}$ denotes the lattice deformation along the $[hkl]$ direction.

Change of width and/or shape of Bragg spots in time-resolved experiments is usually due to the emergence of structural rearrangments induced by the optical excitation. For example, it is a good first approximation signature of dynamical changes in polycrystalline samples. Average size or orientation of crystallites is subject to modification after photoexcitation due to annealing or ordering phenomena. This results in the broadening or narrowing of the observed diffraction features. Experimental evidence of what here mentioned will be investigated further during the thesis.

1.3   ULTRAFAST ELECTRON DIFFRACTION SETUP AT EPFL

This section is based on the scientific publication by G. F. Mancini *et al.*, *Design and implementation of a flexible beamline for femtosecond electron diffraction experiments* [33]. Only the main features of the experimental setup are reported. Additional information about the design and implementation of the experimental setup can be find also in [34] and references therein.

1.3.1   *Experimental layout*

The overall layout of EPFL UED beamline is presented in figure 1.4. In panel A the design of the experiment is shown, while its implementation is depicted in panel B.

The UED apparatus is powered by a KMLabs Wyvern Ti:sapphire amplified laser delivering 50 fs pulses at a wavelength of 800 nm and with an energy of 700 μJ per pulse at a repetition rate of 20 kHz. The shot-to-shot noise on the energy per pulse in this system is below 0.2%. The amplified fs laser beam is used to generate the pump and the probe of the experiment. The pump is responsible for the photoexcitation of the sample at 800 nm. The pulse in the probe line is frequency-tripled by third harmonic generation in nonlinear crystals, and the 266 nm beam thus obtained is used to generate the probing electron pulses inside a DC gun. The DC gun is composed by a high voltage cathode (30 kV) on top of which a silver-coated sapphire window is glued to guarantee electrical connection. The cathode is isolated from the anode, which is grounded to the UHV shield of the DC gun. Electrons are photoemitted by back-illuminating the photocathode with the 266 nm optical pulses, and are accelerated to 30 keV and directed through a Pt-Ir pinhole of 150 μm diameter.

Two solenoids are employed to collimate and focus the propagating electron beam, while two steering plates to deflect it in the two orthogonal direction. A Radio-Frequency cavity is placed right before the experimental chamber and is responsible for the temporal compression of the electron probe pulses. In figure 1.4 C, the temporal and spatial evolution of the electron beam is reported.

A high-precision goniometer allows the motion of the sample along three axis (x,y,z) and one angle θ (the rotation around the z axis). When working in reflection geometry, a fifth degree of freedom ϕ is added, *i.e.* the angular rotation of the sample around its surface normal, obtained by means of a piezo-electric support in thermal contact with the sample manipulator. A cryogenic helium flow system allows to explore a range of temperatures from 1.8 K up to 300 K.

A delay line allows to control the reciprocal arrival time on the sample of pump and probe pulses. The electrons scattered from the sample are detected by a Princeton Charge-Coupled Device (CCD) ca-
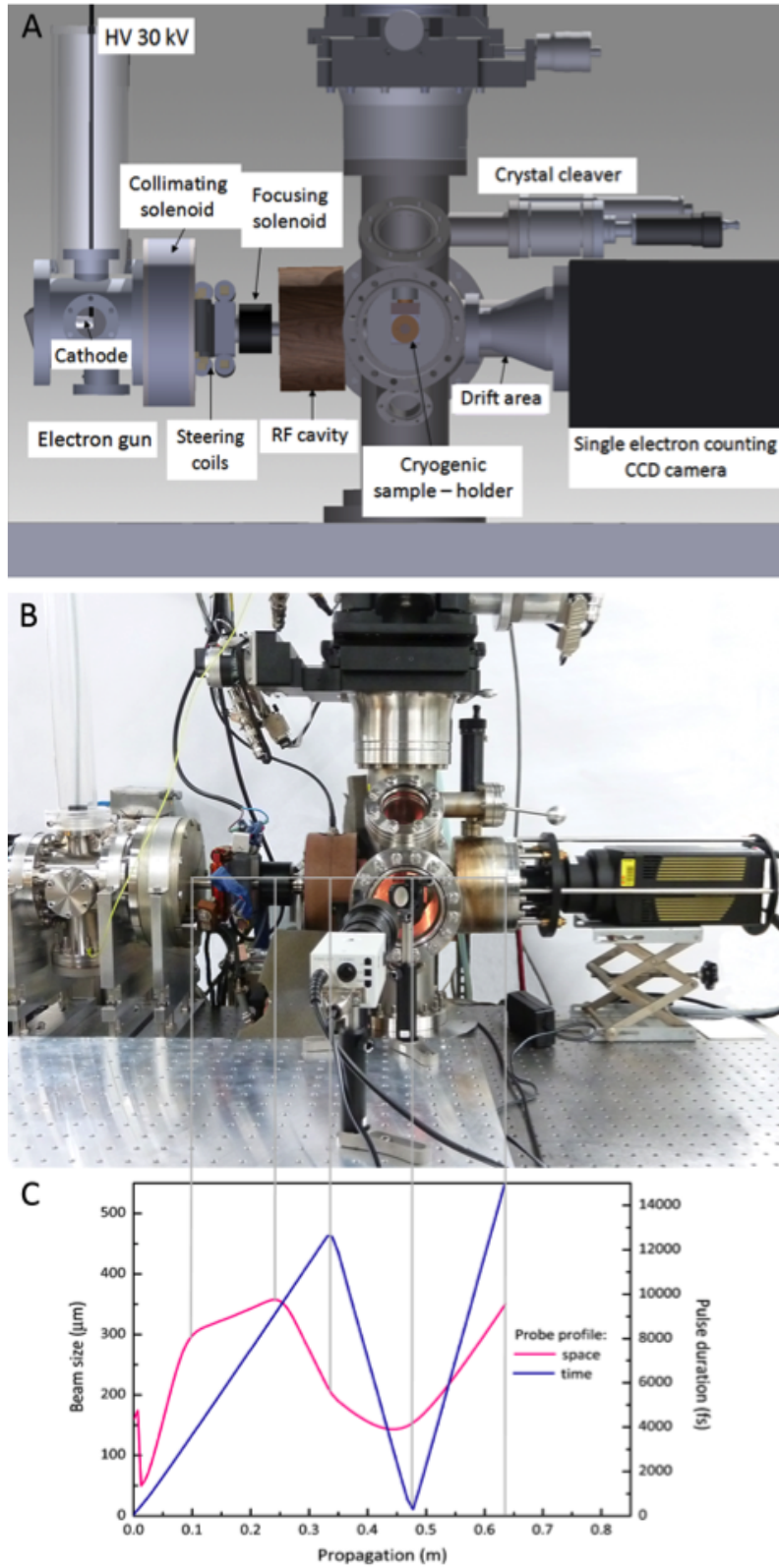
Figure 1.4: Schematics of the UED setup in use at EPFL: design (A) and implementation (B). In panel C the longitudinal evolution of the electron beam is visible (blue line) and of its transverse profile (pink line) displayed as function of the distance from the cathode. As shown, the best in-time and in-space focalization of the electron beam is at the sample position. Picture taken from [33].

pable of a one-to-one conversion efficiency between electrons and output counts. The automation of the experimental setup is performed via a Labview interface on a computer.

1.3.2   *The RF cavity and the synchronization system*

The RF cavity is used in a TM_{010} mode, with a resonant frequency of 3 GHz. It is made out of two Oxygen-Free High thermal Conductivity (OFHC) copper half cells that are brazed together in an oven to a temperature of 750°C for vacuum compatibility. The brazing procedure causes no significant change in the resonant frequency and does not influence the on-axis field profile [6]. The stability of the resonant frequency value is controlled by an AccTec temperature control system with a precision of 4 mK: temperature stability is a crucial parameter for an efficient bunch compression, which is deeply linked to the dimension of the copper cells.

The RF cavity allows the storage of up to 10^5 electrons per pulse by compensating the chirp caused by the Coulomb repulsion among electrons in a single bunch. The TM_{010} mode of the RF field decelerates the faster electrons and accelerates the slower ones, resulting in an efficient temporal recompression of the electron pulse at the sample coordinate. An effective synchronisation system between the cavity and the laser is accomplished by the cooperative interaction of a Phase-Looked Loop (PLL), a Microwave Amplifier and a Bergman pulse generator. A detailed explanation of the synchronisation system can be found in [35].

In figure 1.4 C the longitudinal evolution of the electron beam (blue line) and the transverse profile (pink line) are shown. They are displayed as function of the distance from the photo-cathode. As shown, the best in-time and in-space focalization of the electron beam is at the sample position. Experimental evidence from [33] shows a 160 μm spotsize on the sample with few nm coherence length and less than 300 fs time resolution with 10^5 electrons per pulse at 30 keV.

ORDER-DISORDER PHENOMENA IN
ALKANETHIOL-CAPPED GOLD NANOPARTICLES

This chapter is based on the articles by GF Mancini, F Pennacchio *et al.*, *Order/disorder dynamics in a dodecanethiol-capped gold nanoparticles supracrystal by small-angle Ultrafast Electron Diffraction* [26] and *Local photo-mechanical stiffness revealed in gold nanoparticles supracrystals by ultrafast small-angle electron diffraction* [36]. An extended introduction is added.

The author acknowledges Dr. Giulia Fulvia Mancini for leading this research and for the achievements all along the development of the project.

2.1 ABOUT DIONYSUS AND DICHROIC GLASSES

Wandering around the halls of the British Museum, London, one can easily stumble on a Roman cage cup dated the beginning of the 4th century and called the Lycurgus cup [37]. Its openwork decoration comprises a mythological frieze depicting the triumph of Dionysus over Lycurgus, King of Thrace. Legend has it that Lycurgus, hostile to the god of wine and ritual madness, attacks one of Dionysus maenads, Ambrosia, who turns into a vine. She then coils herself about the king and holds him captive for Dionysus and his fellows to torture him to death. The cup shows the very moment of Lycurgus being captive of the metamorphosed nymph Ambrosia before the arrival of the Dionysus and his fellows [38]. However, despite the outstanding achievement of roman craftsmanship, the most interesting feature of this cup is its behaviour as respect to the direction of illumination: the glass of the cup appears as green-yellow toned jade while reflecting light, while when back-illuminated it turns to a vivid ruby colour (see Fig. 2.1) [38, 39]. This peculiar properties of the glass depends on the presence of a minute amount of silver ($\sim$ 300 ppm) and gold ($\sim$ 50 ppm) under the form of a colloidal system, *i.e.* nanoparticles with diameters in the range of 50-100 nm suspended in the glass. These nanoparticles (NPs) are characterised by an optical absorption whose spectrum is related to their size-dependent plasmon resonance [40]. The induced light-scattering phenomena give rise to the dichroic properties of the glass [38, 41, 42], and this cup is probably one of the first application of nanotechnology recorded in history.

The knowledge behind this naive application of nanotechnology was lost during the Middle Age, while the reputation of colloidal gold remained as having fabulous curative powers for various diseases,

(a) *The Lycurgus Cup. Reflected light on its surface give rise to a yellow-green toned jade appearance.*

(b) *The Lycurgus Cup. Transmitted light generates a ruby red translucence in the glass.*

Figure 2.1: First exemple of gold nanocolloid giving rise to dichroic properties: the Lycurgus Cup. Images courtesy of © The Trustees of the British Museum [37]

such as heart and venereal problems, dysentery, epilepsy, tumors, and - until the 20th century - it was used for the diagnosis of syphilis [43, 44].

The rediscovery of a synthetic pathway for actual gold nanoparticles happened only during the mid-seventeenth century by the German chemist Johannes Kunkell [45]. His protocol consisted into the heterocoagulation in *aqua regia* of gold particles and tin dioxide [46, 47], which were subsequently transferred to molten glass. This protocol was later standardised as the *Purple of Cassius* pigmentation, and it quickly spread around Europe and Asia, as we can find gold nanoparticles used as a pigment in Chinese porcelain at the beginning of the eighteen century [48].

In addition to their millenary history in arts, decoration and protomedicine, nowadays gold nanoparticles, due to their extreme versatility in shape and dimensions, find applications in many different fields ranging from chemical catalysis to biology, from material sciences to nanomedicine. Functionalized gold nanoparticles are used as liquid catalysis agents [49, 50], chemical [51] and biological sensors [52–54] and building blocks for photonic crystal [55]. In medicine [56], they have been successfully tested for biodiagnostics [57], cancer diagnostics, imaging and therapy [58–62] and drug delivery [63–65] applications. Figure 5.2 contains a panoramic of the versatility in synthetic processes, giving rise to different shapes and dimension of gold nanoparticles, whose potential application are being tested.

(a) *Small nanospheres* [66]

(b) *Large nanospheres* [67]

(c) *Nanorods* [68, 69]

(d) *Sharp nanorods* [70]

(e) *Nanoshells* [71]

(f) *Nanocages/frames* [72]

(g) *Hollow nanospheres* [73]

(h) *Tetrahedra / octahedra / cubes / icosahedra* [74]

(i) *Rhombic dodecahedra* [75]

(j) *Octahedra* [75]

(k) *Concave nanocubes* [76]

(l) *Tetrahexahedra* [77]

(m) *Rhombic dodecahedra* [78]

(n) *Obtuse triangular bipyramids* [78]

(o) *Trisoctahedra* [79]
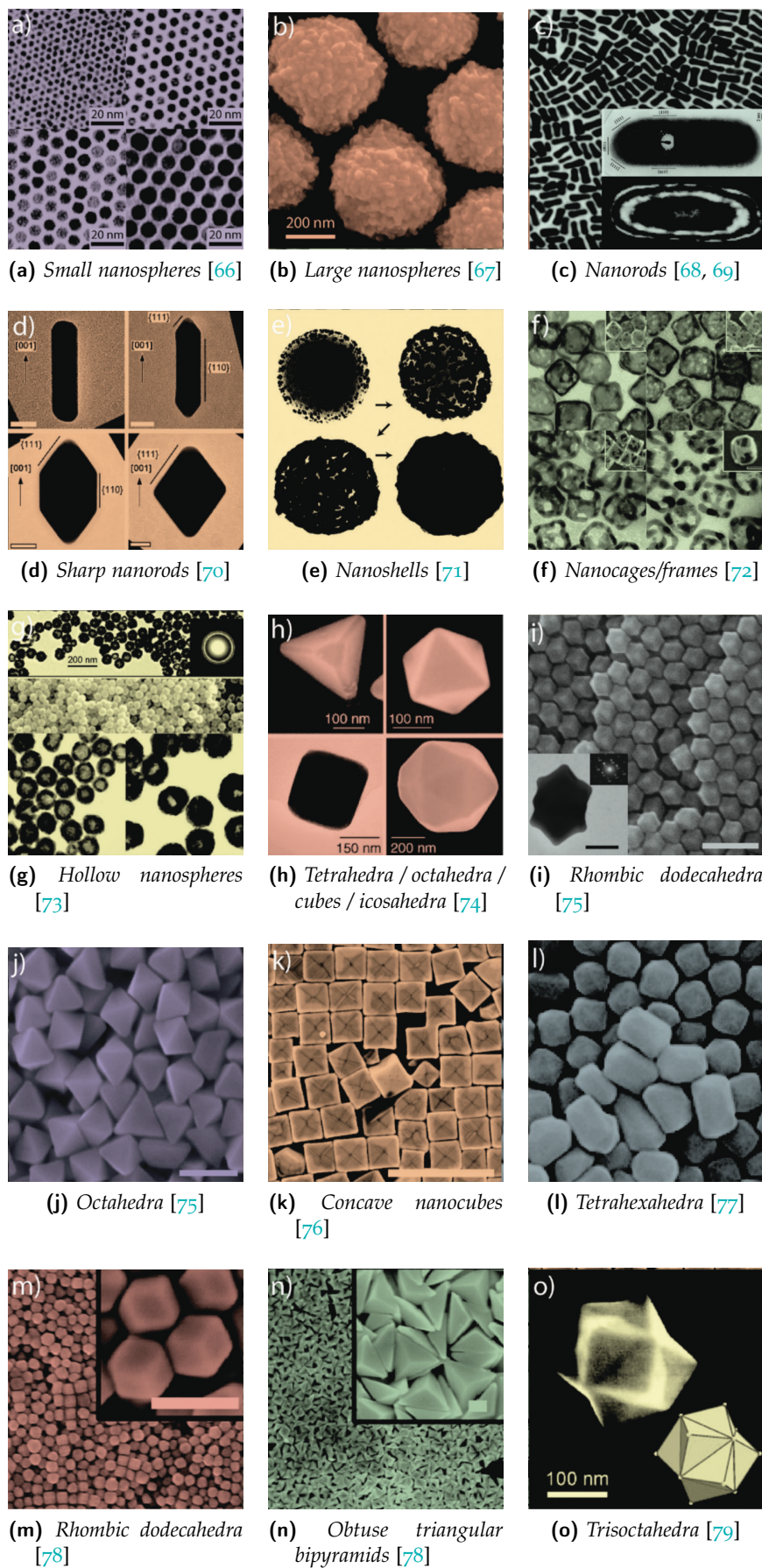
Figure 2.2: Gold nanoparticles of various size and shape with potential applications in biomedicine. From [80].

2.2   GOLD NANOPARTICLES 2D-ASSEMBLIES

Two-dimensional supracrystals created by self-assembly of nanoparticles (NPs) offer an efficient and flexible route toward engineering materials with specific functionalities that can be tailored for a wide range of applications [81, 82]. In these hybrid organic-inorganic materials the building blocks are metallic core NPs functionalised with a ligand shell of organic molecules which are chemically bound to the core surface. In these peculiar systems, both the metallic core and the ligand chemical composition are essential to tailor their macroscopic structural, electronic, optical and magnetic properties [83–86].

In alkanethiol-protected gold NPs supracrystals, the difference in length and composition of the ligand molecules can result in a different self-assembled final phase, ranging from crystalline to glassy, due to competition between thermodynamic driving forces [87]. The structural diversity and the stabilisation of these supracrystals are primarily affected by the level of ligand interdigitation [88, 89].

The simultaneous characterisation of the NPs cores and their ligands shell, as well as of the short-range properties of the NPs assembly, has proven challenging so far [81]. Mueggenburg *et al.* showed that monolayers of dodecanethiol-capped gold NPs display a mechanical strength comparable to glassy polymers, accompanied by robustness and resilience at higher temperatures [90]. In this work, however, only macroscopic (i.e., long range) properties of the overall colloidal crystal were analysed.

In alkanethiol-capped NPs colloidal crystals, the local (i.e., short-range) mechanical properties are primarily affected by the local arrangement of NPs cores and organic ligands within single grains. To effectively analyse these system, a technique which can combine Ångstroms (Å) spatial resolution with sensitivity to light elements is needed. Effects of ligand chain length on NPs packing density or disorder have recently been explored in two-dimensional ligand-stabilized NPs supracrystals by Kim et al. [87]. There, equilibrated monolayers were produced by cyclic compression and relaxation in Langmuir trough [91]. Their phase transition from crystalline to liquid through a hexatic phase was interpreted as an entropy-driven phenomenon associated with steric constraints between ligand shells.

In this chapter, we report how ultrafast small-angle electron diffraction has enabled to resolve both their static ordering properties and their photo-induced motions with both femtosecond (fs) temporal and Ångstroms (Å) spatial resolution [26].

With this technique, light pulses can be used to set the supracrystals out of equilibrium. The transfer of energy from the electronic excitation to the underlying structural degrees of freedom leads to motions of both the NPs and the ligands that can be monitored by diffracting ultrashort electron pulses. This electron-lattice energy trans-
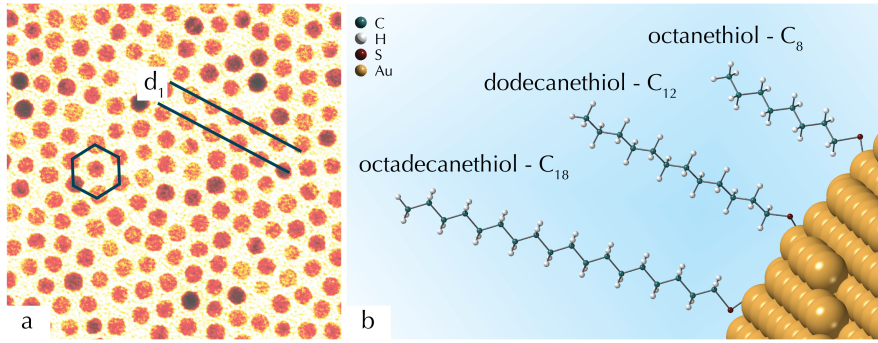
Figure 2.3: Au NPs 2D supracrystal description. (a) Picture of the C_{12} sample, where the hexagonal arrangement of the nanoparticles is evidenced. Crystallographic planes of the superlattice with distance d_1 are also highlighted. The parameter d_1 is strongly depending on the ligand length. Image courtesy of SuNMiL group / EPFL. (b) Qualitative rendering of the three involved alkanethiols capping one NP surface, aiming to display their structure and different lengths.

fer results in the Debye-Waller effect, visible in the loss of intensity of a diffraction feature due to thermal agitation of the scattering objects.

2.3 MATERIALS AND METHODS

Three different 2D nanoparticles supracrystals were studied. Each sample is consisting of monodisperse gold NPs of the same size ($\sim$5 nm diameter) coated with different alkanethiols (R-SH, R = C_nH_{2n+1}): 1-octanethiol (n = 8), 1-dodecanethiol (n = 12) and 1-octadecanethiol (n = 18). Within the text, we will refer to these samples as C_8, C_{12} and C_{18}, respectively. Au NPs present an atoms arrangement in a face-centered cubic (fcc) lattice [92]. The chemical structure of each ligand (n = 8, 12, 18) is displayed in figure 2.3. The ligand lengths and the average core-core NPs distances for each supracrystal, retrieved experimentally with electron diffraction, are summarized in Table 1. We analysed the transient changes in the NPs hexagonal arrangement at s_1 for the C_8 and the C_{12} supracrystals and compared their time responses (Fig. 2.5b).

The main results of the experiments are summarised in the following table :

Sample	s_1 [Å^{-1}]	ligand length [nm]	interparticle distance [nm]	time scale τ [ps]
C_8	0.118	1.28	6.1	2.6 $\pm$ 0.3
C_{12}	0.095	1.78	7.2	12.1 $\pm$ 0.9
C_{18}	0.098	2.54	7.4	-

2.3.1 *Sample preparation*

Gold NPs coated with 1-octanethiol (C_8), 1-decanethiol (C_{12}), or 1-octanedecanethiol (C_{18}) were synthesised using a modification of the Brust-Schriffin method [93, 94] called Stucky method and described in [95]. The synthesis was performed by the Supramolecular Nano-materials and Interfaces Laboratory (SuNMiL) group at École Polytechnique Fédérale de Lausanne (EPFL).

The synthetic protocol is the following: 0.125 mmol of AuPPh$_3$Cl (chloro(triphenylphosphine)gold(I)) and 0.375 mmol of the corresponding alkanethiol were mixed in 20 mL of benzene at room temperature for 10 min and then introduced in a heating bath at 90°C until reaching reflux conditions. Then, 1.25 mmol of the reducing agent tert-butylamino-borane complex dissolved in 20 mL of benzene was added to the solution, left for reaction during 1h, and cooled at room temperature. The coated nanoparticles were successively precipitated with methanol and cleaned five times in acetone by centrifugation and redispersion in a sonication bath. They were then dried in vacuum for storing and redissolved in toluene before use (C_{18}-coated nanoparticles needed a mild heating ($\sim$30°C) to completely dissolve).

NPs monolayers were prepared by dropwise deposition of a toluene solution with suspended NPs onto the water subphase of a Langmuir trough [91], which enables the control over the longitudinal pressure applied. The layer was compressed up to a pressure value of 18 mN/m^2, and then transferred to an amorphous carbon-coated copper grid through a Langmuir-Schaefer deposition [96, 97], which preserves the the monolayer density, thickness and homogeneity.

Transmission Electron Microscopy (TEM) images of the obtained 2D-monolayers are shown in figure 2.6a-c. The images analysis allowed the following dimensional characterisation:

- 1-octanethiol Au NPs: core diameter of 4.4 $\pm$ 0.5 nm and interparticle distance of 6.1 $\pm$ 0.6 nm;

- 1-dodecanethiol Au NPs: core diameter of 5.16 $\pm$ 0.58 nm with 9% polydispersity and an interparticle distance of 7.2 $\pm$ 0.68 nm;

- 1-octadecanethiol Au NPs: core diameter of 4.8 $\pm$ 0.3 nm and an interparticle distance of 7.4 $\pm$ 0.5 nm.

Only information concerning the Au NPs cores is retrievable in TEM images taken with 200 keV electrons, since the ligands do not provide enough contrast and they are thus are not visible. The TEM analysis was performed with the software package ImageJ. The projected area of the nanoparticles was calculated by standard particle analysis and default graylevel threshold. The diameter was calculated assuming spherical nanoparticles and averaging to all nanoparticles (>1000). The interparticle distance was obtained by the calculation of the cen-
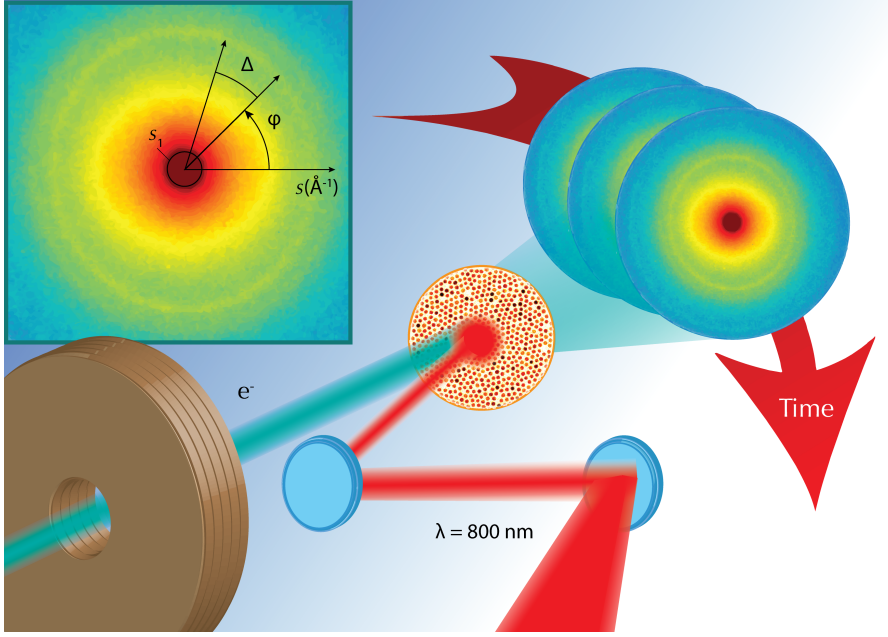
Figure 2.4: Graphical rendering of the ultrafast small-angle electron scattering experimental layout. Ultrashort electron bunches are focused onto each supracrystal, while dynamical transitions in the sample are initiated by 1.55 eV light pulses. The electrons scattered from the sample are collected on an single electron CCD. The top-left inset shows a diffraction pattern recorded in the experiment and the concept involved in angular cross-correlation analysis (see section 5.3). The Debye-Scherrer rings from polycrystalline gold are detected at large angle. The information related to the NPs symmetry in each supracrystal is contained at small angle.

ter of mass of every nanoparticle and avereging to all nanoparticle neighbour pairs. The results from the TEM image analysis are consistent with the ones obtained with electron diffraction (see Table 1).

2.3.2   *The experiment*

A KMLabs Wyvern Ti:sapphire amplified laser generating 50 fs (Full Width at Half Maximum (FWHM)), 700 µJ pulses, 800 nm central wavelength, 20 kHz repetition rate, is the light source for both the photoexciting pump pulses and to generate the probing electrons at 30 keV. The temporal spread of the 30 kV probe electron pulses is controlled by means of a radiofrequency (RF) compression cavity [98, 99], allowing to store up to 6×10^5 electrons in $\sim$300 fs bunches [33].

Experiments were performed in transmission geometry at room temperature. In order to reduce the reciprocal spatiotemporal mismatch, an almost collinear arrangement between the pump and probe pulses was implemented. The photoexciting pulses with 1.55 eV energy are focused to a spot of 220 µm and provide an incident fluence of 10 mJ/cm^2. Dynamics are then probed by an electron beam focused with a set of magnetic lenses to a $\sim$ 160 µm diameter spotsize. Considering the optical reflectivity of gold in a layer of 7 nm thickness, the penetration depth, assessed around 7-8 nm at 1.5 eV [100]

and the sample density, the effective fluence absorbed by the sample is estimated around 100 $\mu J/cm^2$.

The diffraction pattern, shown in the top-left inset of figure 2.4, is formed on a phosphor screen and recorded by a CCD camera capable of single electron detection. Diffraction patterns from the NPs supracrystal are recorded at different time-delays between the pump photoexcitation and the probe, allowing to reconstruct the composite dynamics in the sample.

Also, the very low duty cycle allows a large relaxation time between subsequent pulses. For these reasons, radiation damage was not observed in these experiments. The background pressure in the experimental vacuum chamber was below 10^{-9} mbar.

2.4 STRUCTURE RETRIEVAL

The structure retrieval method is based on the calculation of the angular Cross-Correlation Function (CCF), which have been proved effective in retrieving local symmetries hidden within disordered structures [26, 101–103].

In our experiment, information concerning the local arrangement of NPs is contained in the small-angle region of the diffraction patterns from each supracrystal, at the scattering vector s_1 marked in the inset of figure 2.4. For each sample, the diffraction feature at the scattering vector s_1 is related to the real space distance d_1 of crystallographic planes originated by the nanoparticles arrangement in the supracrystal (see Fig. 2.3a). The values of s_1 retrieved via UED for each sample are reported in Table 1. The normalized CCF is defined as [101–105]:

$$C_{norm}(\Delta) = \frac{\langle I(s_1,\varphi)I(s_1,\varphi+\Delta)\rangle_\varphi - \langle I(s_1,\varphi)\rangle_\varphi^2}{\langle I(s_1,\varphi)\rangle_\varphi^2} \qquad (2.1)$$

where $I(s_1,\varphi)$ represents the scattered intensity at the scattering vector s_1 and the angle φ; Δ is the shift between the two angles, (inset of Fig. 1) and $\langle\rangle_\varphi$ denotes an averaging over φ. Following the approach described in [26], the normalized CCF at the scattering vector s_1 for each sample was obtained from the one-dimensional Fourier spectrum of the scattered intensity $I(s_1,\varphi)$. As mathematically derived in [106], characteristic symmetries in such dense systems of identical particles can be detected in the CCF when - as in our case - the coherence length of the probing wave is comparable to the size of the single particle.

Figure 2.5a displays the CCF profiles retrieved at equilibrium (i.e. before photoexcitation) for the C_8 (red), C_{12} (orange) and C_{18} (pink) supracrystals at the scattering vector s_1, which is the scattering vector
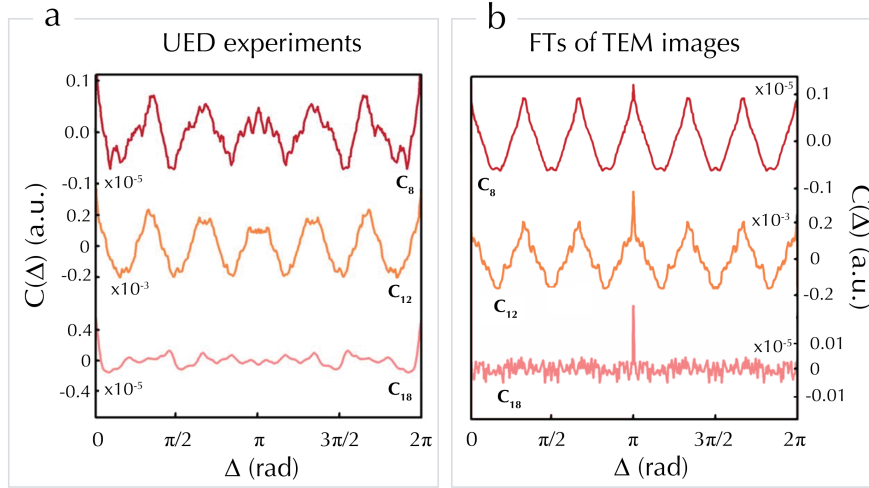
Figure 2.5: Ligand length-dependent structural arrangement of alkanethiol-coated Au NPs. (a) The degree of hexagonal symmetry of the NPs within the supracrystal is unraveled by angular cross-correlation analysis. The electron diffraction data show a clear hexagonal arrangement of the NPs in the C_8 (red) and C_{12} (orange) supracrystals, whereas a disordered, liquid phase is found for the C_{18} (pink) sample. (b) Angular cross-correlation function analysis at s_1 from the Fourier transform of the TEM images of the three samples. The location of s_1 in the two-dimensional simulation is reported in Fig. 2.6a-c. For each curve, s_1 refers to the first order of diffraction from the crystallographic planes with distance d_1 displayed in Fig. 2.3. The angular cross-correlation reflects the degree of disorder in the hexagonal distribution of the NPs in the sample, and it is in agreement with the CCF profiles extracted with small-angle electron diffraction. Figure readapted from [36].

related tho the d_1 spacing of the supracrystal planes. The 6-fold modulation of the CCF from the C_8 and C_{12} samples reflects the hexagonal close-packed arrangement of the NPs in the supracrystals (Fig. 2.3a). This unveils the presence of a supracrystalline structural phase in which neighbouring NPs are held together within single grains by attractive Van der Waals forces that lead to the favourable interdigitation of the ligands [87–89]. Thus, NPs in each grain arrange in crystallographic-like planes with distance $d_1 = \frac{2\pi}{s_1}$ (Fig. 2.3a). The absence of recognizable symmetries for the C_{18} sample suggests the absence of short-range order in the NPs self-assembly, and thus the similarity of the C_{18} monolayer to a polycrystalline phase. This disordered final arrangement of NPs is probably due to the increased ligand length, to repulsive forces winning over Van der Waals attractive interactions [87] and to lower NPs solubility and mobility at room temperature.

2.5 ORDER-DISORDER PHENOMENA

To better understand the correlation between the retrieved difference in small-angle scattering and the symmetry of the NPs monolayers, ligand length-dependent order-disorder correlations in the three supracrystals were explored in a series of simulations.
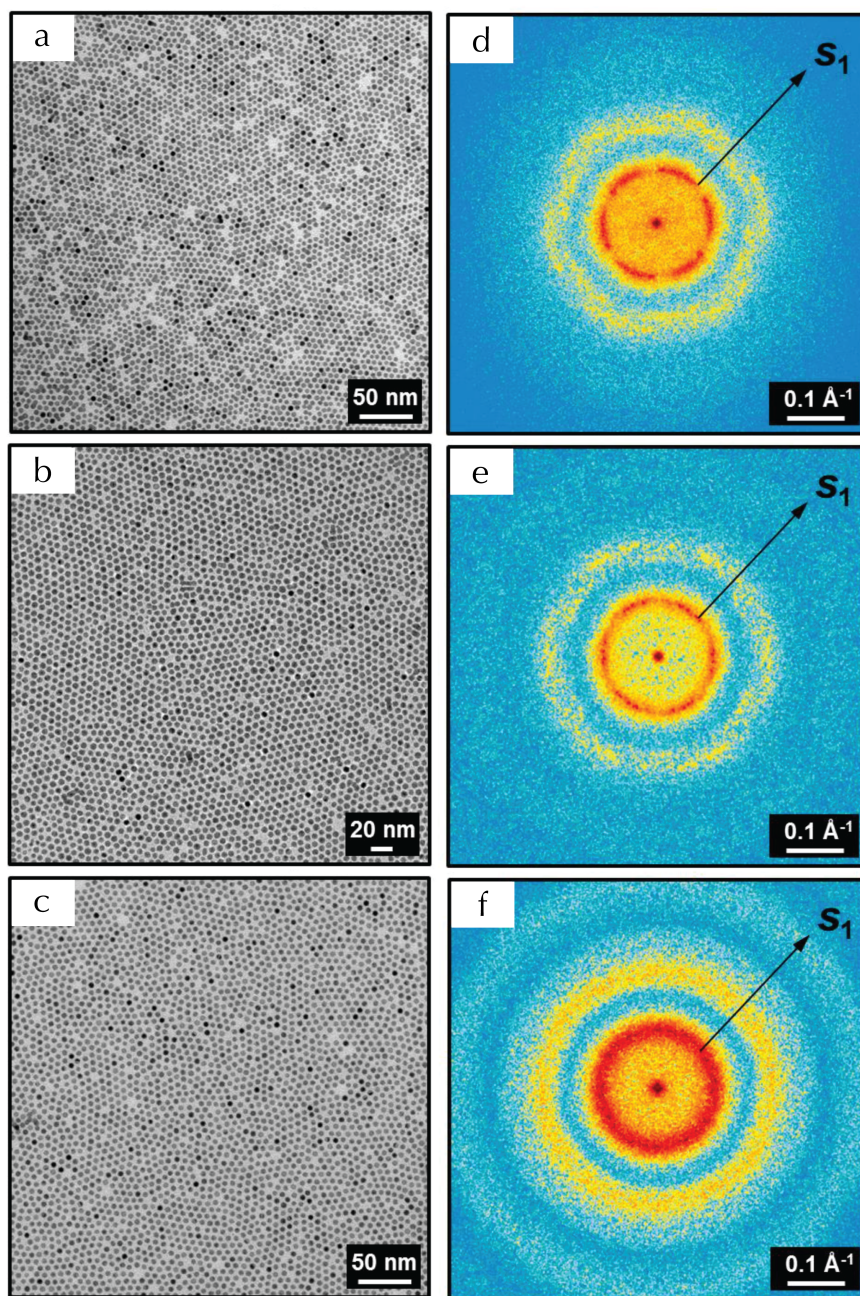
Figure 2.6: TEM images and Fourier transforms of the three considered samples. (a, b, c) TEM images of the C_8, C_{12} and C_{18} supracrystals (top to bottom). (d, e, f) Diffraction patterns simulated as the squared amplitude of the Fourier transform of the three TEM images in (a, b, c) respectively, confirming the increasing disorder as a function of the ligand length (top to bottom). In each simulation, s_1 marks the first order of diffraction from the crystallographic planes with distance d_1 displayed in Fig. 2.3a. Each two-dimensional Fourier transform is normalised to the number of nanoparticles detected in the corresponding TEM image. From [36].

The TEM images of the C_8, C_{12} and C_{18} samples are displayed in Fig. 2.6. The corresponding diffraction patterns are retrieved as the squared amplitude of the Fourier Transform (FT) of the TEM images.

The TEM images and the simulations (Fig. 2.6a-c and Fig. 2.7a, b) cover an area of 390 nm x 390 nm. The area in the TEM images is included within the one probed experimentally with UED. Artifacts in all two-dimensional Fourier transforms associated with image re-scaling were avoided by converting image to a binary (black and white) image, followed by multiplication with an apodizing cosine function to smooth the edges of the images [107]. Each two-dimensional Fourier transform is normalized to the number of nanoparticles detected in the corresponding TEM or simulated image.

The patterns in Fig. 2.6 directly visualise a hexagonal order at s_1 in the C_8 and C_{12} samples. The core-to-core distance values extracted from the FTs of the TEM images are in agreement with the values retrieved experimentally with electron diffraction (Table 1). These direct observations are supported by the analysis of the CCF profiles retrieved from the Fourier transforms of the TEM images. (TEM images and related FT simulation: figure 2.6, CCF profiles : figure 2.5b).

To assign the different local distribution of the NPs within supracrystal grains, we simulated our samples by means of the so-called Sphere Lattice Model (SLM) (see Fig. 2.7). The models are created from a two-dimensional lattice of opaque spheres ($\sim$ 5 nm diameter) arranged in a hexagonal lattice. Then, circular domains with a diameter of 60 nm and a centre-to-centre distance of 80 nm are defined and rotated by the angle η, which is Gaussian distributed with the mean = 0 and standard deviation σ.

Two NPs distributions are simulated and shown in figure 2.7:

- σ = 10° with a perfectly ordered spheres arrangement preserved within each domain (a);

- σ = 10°, with disorder of individual NPs positions introduced by adding a random shift up to $\Delta r = \pm 1$ nm (b).

From the models, the diffraction pattern are simulated as the squared amplitude of the Fourier transform, as previously done for the TEM images (see Fig. 2.7c,d) . The scattering vector s_1 is indicated in figure 2.6 for the experimental and Fig. 2.7 for the simulated Fourier transforms. In each, s_1 marks the first order of diffraction from the crystallographic planes with distance d_1 displayed in Fig. 2.3a. We evidence two different similarities between:

- the [10°, 0] Sphere Lattice Model with the C_8 and C_{12} samples, and

- the [10°, ± 1 nm] Sphere Lattice Model with the C_{18}.

Differences in contrast at s_1 between the FTs from TEM experimental images and the FTs from the corresponding SLM simulations and

$\sigma = 10°, \Delta r = 0$ $\sigma = 10°, \Delta r = \pm 1$ nm
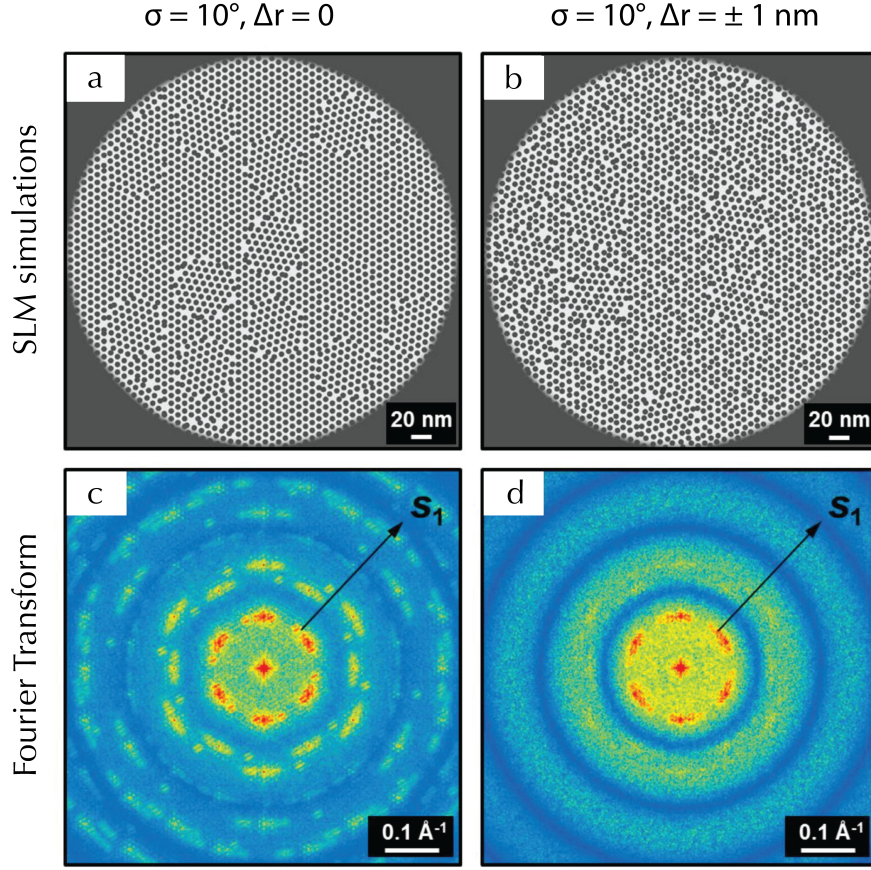
Figure 2.7: Sphere Lattice Model (SLM) simulations of the supracrystal and corresponding Fourier transforms. Simulations of the TEM images considering each NP as a spherical opaque object. Circular domains with a diameter of 60 nm and a centre-to-centre distance of 80 nm are defined and rotated by the angle η, which is globally Gaussian distributed with the mean = 0 and standard deviation σ (a) SLM with σ = 10° with a perfectly ordered NPs positional arrangement preserved within each domain. (b) SLM with σ = 10°, with disorder of individual NPs position introduced by adding a random shift up to $\Delta r = \pm 1$ nm. (c) Diffraction patterns simulated as the squared amplitude of the Fourier transform of (a). (d) Diffraction patterns simulated as the squared amplitude of the Fourier transform of (b). Each two-dimensional Fourier transform is normalised to the number of nanoparticles in the corresponding SLM simulation. From [36].

in the more evidenced periodicity in the [10°, ±1 nm] SLM as respect as the C_{18}-FT diffraction pattern are mostly due to a lower degree of disorder of NPs - and thus to the lack of random additional noise - in the SLM simulated data.

These similarities are further confirmed by the Radial Average Intensity (RAI) analysis, a,b, where the RAI at s_1 is calculated as:

$$I(s_1) = \frac{1}{2\pi} \int_0^{2\pi} I(s_1, \varphi) d\varphi \tag{2.2}$$

As visible in the RAI plots in figure 2.8, multiple orders of diffraction from the family of crystallographic planes defined at s_1 characterise locally symmetrical systems (C_8, C_{12}). These diffraction orders
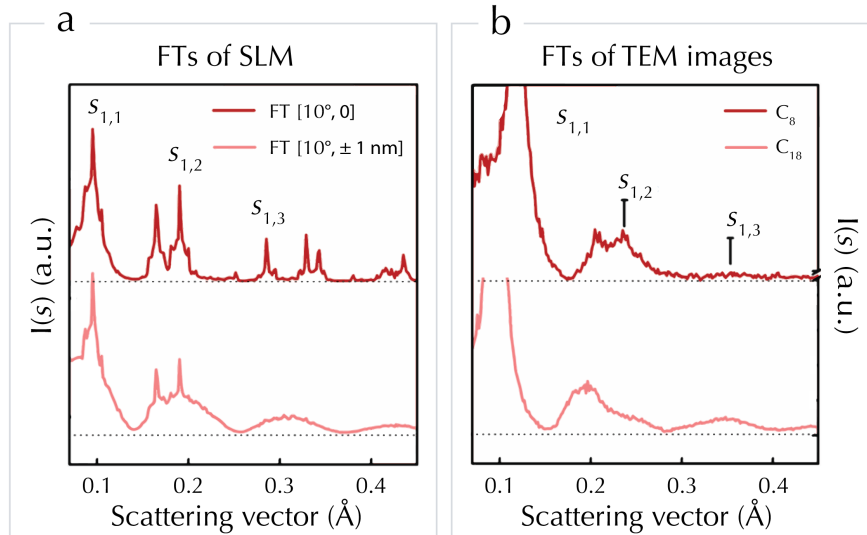
Figure 2.8: Compared intensity profiles from experimental and simulated Fourier Transforms of the C_8, C_{18} TEM images. (a) Radial averaged intensity of the Fourier Transform of the $[10°, 0]$ simulation (red) and of the $[10°, \pm 1 \text{ nm}]$ simulation (pink). (b) Radial averaged intensity of the Fourier transform of the TEM images for C_8 (red) and C_{18} (pink). From [36].

progressively smear into a pattern from distributed objects by increasing the positional disorder of the NPs (C_{18}). This confirms the identified scenario where the local short-range order would be a function of the chosen capping ligand.

2.6 TIME-RESOLVED RESPONSE

The transient change of $I(s_1)$ for the C_8 (red circles) and the C_{12} (orange squares) supracrystals have been analysed and is reported in figure 2.9. Each intensity trace was normalised to the average value at negative times ($t < t_0$) and fitted to a mono-exponential curve (solid lines). As confirmed by the CCF static analysis (Fig. 2.5a), the distribution of NPs in the C_{18} sample is comparable to a polycrystalline phase and no recognisable local symmetry is evidenced. Thus, due to the lack of easily identifiable diffraction features, no correlation between transient changes and NPs arrangement can be unraveled. For this reason, the temporal dependence of the scattered intensity $I(s_1)$ for the C_{18} supracrystal is not reported in figure 2.9.

Photoinduced thermal disorder in the NPs hexagonal arrangement is evidenced in both C_8 and C_{12} samples by the transient decrease of $I(s_1)$. Remarkably, the $I(s_1)$ decay time-scale for C_8, $\tau = 2.6 \pm 0.3$ ps, is significantly shorter than the one for C_{12}, $\tau = 12.1 \pm 0.9$ ps. The $I(s_1)$ suppression for C_8 and C_{12} is attributed to the energy transfer between the light-initiated electronic excitation and the underlying structural degrees of freedom of the supracrystal.
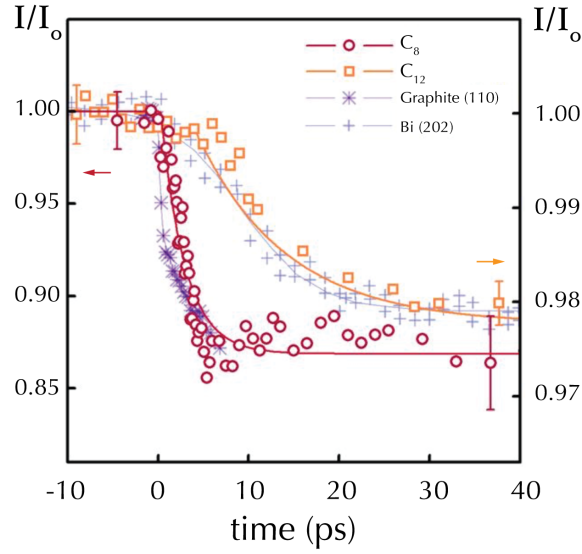
Figure 2.9: NPs dynamics for the C_8 and C_{12} supracrystals are compared to the time-response of graphite and bismuth in UED transmission experiments. The C_8 supracrystal (red circles) shows a decay in diffracted intensity comparable to graphite (purple stars), suggesting a strong coupling of the electronic and lattice degrees of freedom. When the ligand length increases (C_{12}, orange squares) the system is characterized by a softer electron-phonon coupling, similar to soft metals such as bismuth (grey crosses). Graphite data were digitized from [24], bismuth data from [108]. Figure readapted from [36].

Similar experiments are routinely carried out in solids, where the rate of the energy transfer between the electronic and structural subsystems is governed by the electron-phonon coupling [109]. Conventionally, in stiffer solids having hard and strongly coupled phonons such as graphite, a fast decay of the Bragg peaks intensity is observed [24, 25, 110]. In graphite, characterised by strong homonuclear covalent bonding, the fast bi-exponential decay of $I(s_{110})$ reveals strong coupling between the electronic structure with a small subset of lattice degrees of freedom as fast as $\tau = 250$ fs, followed by carriers cooling through electron-phonon and phonon-phonon scattering happening on a longer timescale $\tau = 6.5$ ps [24]. Conversely, in softer materials having a weaker electron-phonon coupling, such as bismuth [108, 111] or gold [100, 112], the energy transfer from the electronic excitation to the lattice takes longer time, yielding a slower decay of the Bragg peaks intensity.

In figure 2.9, the two retrieved intensity decay traces are compared to the ones detected in transmission ultrafast electron diffraction in the two aforementioned solid state systems: graphite [24] (purple asterisks) and bismuth [108] (grey crosses).

Intuitively, in nanostructured systems such as the ones investigated in this work, the presence of attractive Van der Waals interactions among ligands should act as a glue to hold the NPs in the supracrystal together via interdigitation. Such non-covalent bonding and its dynamical response to energy transfers should lead to a disordering

of the NPs local arrangement on time scales comparable if not slower to those of a soft solid, such as bismuth.

While our observations suggest that this scenario applies for the C_{12} supracrystal, where the relaxation follows a timescale τ = 12.1 ps, the dynamics observed in the C_8 supracrystal show substantial differences. In the C_8 supracrystal, the intensity drop of the diffracted beam undergoes a quench whose time constant is comparable to what observed in graphite - to date the fastest ever unveiled with Ultrafast Electron Diffraction (UED) [24, 25, 110].

The velocity of the $I(s_1)$ suppression is thus directly related to the coupling strength between the electronic and structural degrees of freedom in each supracrystal, and undergoes significant changes as a function of the ligand length. The actual rapidity in the suppression of the diffracted intensity for C_8 suggests that the interdigitation of shorter ligands provides a very efficient channel for energy transfer between the initial electronic excitation to structural motions of the NPs.

The photoinduced disorder observed in both C_8 and C_{12} supracrystals is accompanied by annealing of NPs grains [26], evidenced by a transient increase in the signal-to-noise ratio of the CCF profiles at different time delays. This behaviour indicates that local order is impulsively triggered, within the relevant time-scales, in supracrystals where the NPs distribution is stabilised by ligand interdigitation.

A 14% and a 10% transient $I(s_1)$ suppression is reported in Fig. 2.10a,c for C_8 and C_{12}. In each panel, three time delays (t1 < t0, t2 $\sim$ t0, t3 > t0) are selected to evaluate the cross-correlation functions. The CCF profiles at the three time delays (t1, t2, t3) at s_1 are displayed in Fig. 2.10b for C_8 and Fig. 2.10d for C_{12}. The amplitude decrease of the CCF profiles as a function of time is consistent with the dynamics in the system retrieved from the time traces, evidencing a global photo-induced disorder in the monolayers. However, the six-fold CCF profiles are found to transiently become more evident as higher signal-to-noise ratio upon photo-excitation, despite decreasing in amplitude, indicating the annealing of the grains in both samples. Thus, local order in the grains arrangement is impulsively triggered for each supracrystal, within the relevant time-scales.

2.7 CONCLUSIONS AND PERSPECTIVES

In conclusion, we can assert that the combination of ultrafast electron diffraction and ultrafast small-angle scattering is the best candidate to study order-disorder phenomena in 2D-monolayers. This is due to the combination of its spatial (Å) and temporal (fs) resolution.

The proposed results are based on the observation of the light-induced decay of the intensity of the diffraction feature associated to the local (nearest to next-nearest neighbour) hexagonal arrange-
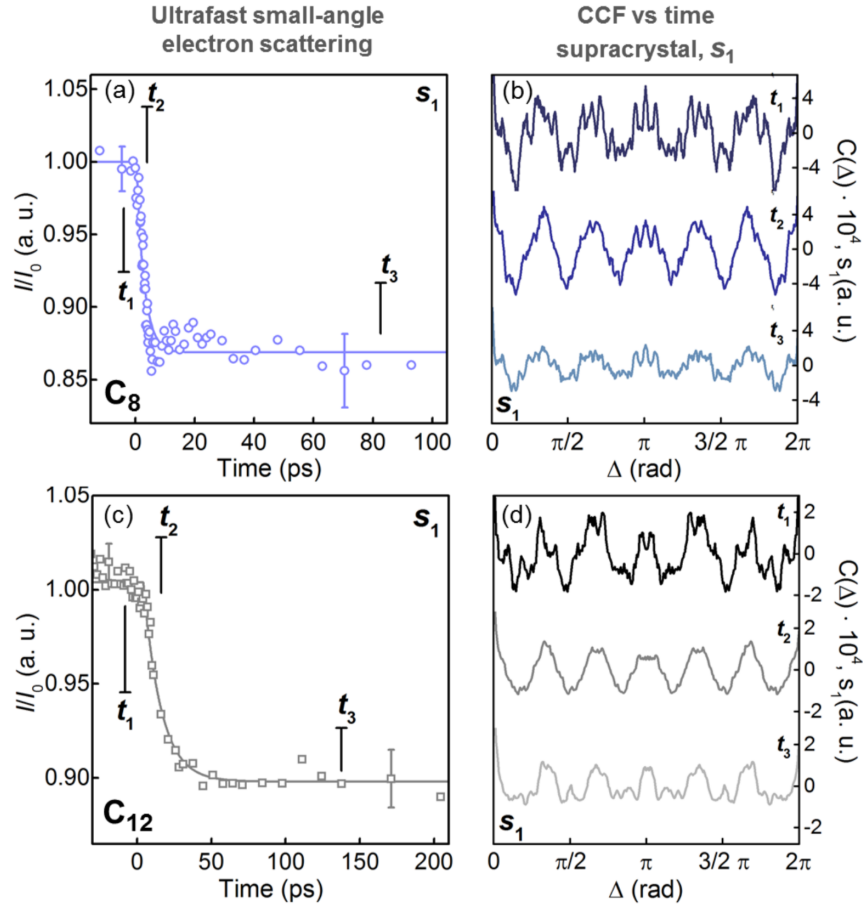
Figure 2.10: Grains transient annealing in C_8 and C_{12} samples. Left: dynamics of $I(s_1)$ for the C_8 (a) and C_{12} (c) supracrystals. Each intensity data set is normalised to its average value before time zero (I_0) and it has been fitted to a mono-exponential function. Right: CCF profiles at s_1 at three time delays (t1, t2, t3) for C_8 (b) and for C_{12} (d). The six-fold CCF profiles are found to transiently become more evident as higher signal-to-noise ratio upon photoexcitation, despite decreasing in amplitude, evidencing annealing of the grains in both samples. Data in (c, d) are adapted from [26].

ment of the gold NPs in each supracrystal. The rate of this decay for the octanethiol-capped nanoparticles supracrystal is as fast as what is observed in a very stiff solid such as graphite, characterised by strong homonuclear covalent bonding. The transient response from supracrystals of dodecanethiol-coated gold nanoparticles, instead, is found to be significantly slower, comparable to softer systems.

Our experimental results are supported by simulations which demonstrate that the local symmetry of the NPs within the supracrystal grains affects the short-range degree of coupling between the electronic and lattice degrees of freedom. Our observations provide a new insight in the local structural dynamics of soft matter suggesting that local stiffness can be created in a supramolecular assembly by Van der Waals forces to an extent comparable to a covalent assembly. Furthermore, the ability of our technique to assess the local photo-mechanical properties of such aggregates provides a valuable tool for future design of short-range properties in functionalised-NPs supracrystals characterised by discontinuities and grain boundaries. Thus, the proposed analysis could easily became an excellent candidate to assess the structural local and long-range properties in hybrid organic-inorganic 2D materials, which are nowadays the subject of a constantly growing interest in the scientific community.

In the light of our results, predictive models which could describe the energy transfer in soft matter upon photo-excitation are needed. Such analysis requires a complete microscopic description of phonons in colloidal matter. Accessing the local photo-mechanical properties of self-assembled supracrystals can be an important step towards the design of novel functional materials with large local stiffness and unique thermo-mechanical properties.

DESIGN AND IMPLEMENTATION OF AN OPTIMAL PUMP FRONT TILTING

This chapter is based on the article by F. Pennacchio *et al.*, *Design and implementation of an optimal front tilting scheme for ultrafast electron diffraction in reflection geometry with high temporal resolution* [113]. An extended introduction is added. Furthermore, additional experimental results can be found, together with the design and implementation of a tilting setup for laser pulses with wavelength λ = 400 nm.

3.1 GROUP VELOCITY MISMATCH IN REFLECTION GEOMETRY

In optics, when pulses with different polarization direction or wavelength propagate in transparent media they are have in general different *group velocities*. The direct consequence of the mismatch between velocities is that pulses which temporally overlap at a given position in space do not overlap anymore after some propagation distance. This phenomenon is named Group Velocity Mismatch (GVM).

In UED due to the different physical nature between the optical pump and the electron probe pulses and their consequential different group velocity, this phenomenon is enhanced as respect to light GVM at visible/infrared frequencies. At 30 keV, the electron velocity v_{el} is approximately one third of the light speed c (see Fig. 3.1a), and thus their GVM, when in collinear geometry can be evaluated as follows:

$$GVM = \frac{1}{c} - \frac{1}{v_{el}} \approx 10 \; ps/mm \tag{3.1}$$

Nevertheless, GVM does not affect the time resolution of UED experiments performed in transmission geometry. As the pump and probe beam impinge almost collinearly on the sample surface and because of a sample thickness generally below 100 nm, GVM effect becomes negligible due to the narrow spatial interaction volume between the light and the electron pulses at the sample.

On the contrary, in Ultrafast Reflection High-Energy Electron Diffraction (URHEED), the pump beam reaches the sample perpendicularly while the electron beam arrives with a grazing angle with respect to the sample. This causes the electrons to probe at different times different regions of the sample surface, which are conversely excited simultaneously by the pump pulse. Thus, a mismatch in group veloci-
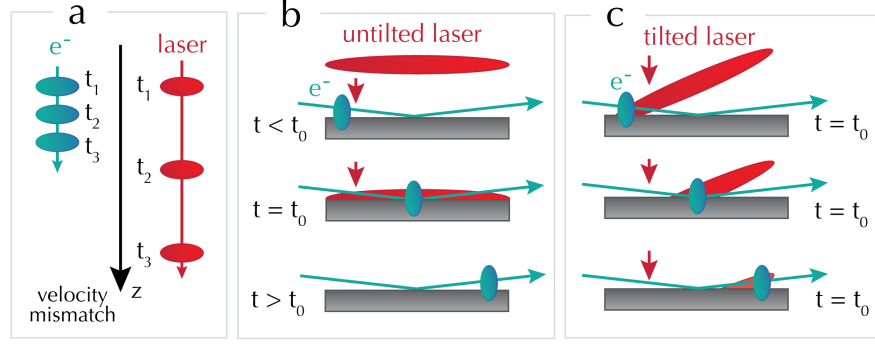
Figure 3.1: Group Velocity Mismatch (GVM) and tilting principles. Representation of the GVM (a) between the optical pump pulse (red) and the 30 keV electron probe (blue). During diffraction experiments in reflection geometry, the mismatch in group velocity causes the electrons to probe at different times regions of the sample surface, which are excited simultaneously by the pump pulse (b). This can be avoided with a proper tilt of the wavefront of the pump pulse (c).

ties affects and broadens the overall time resolution of the experiment (Fig. 3.1b). A possible solution for the aforementioned worsening of the time resolution is the employment of a pump pulse that is tilted by an angle α between the intensity front and the propagation direction. As represented in Fig. 3.1c, a tilted beam allows the pump and the probe beams to be synchronous on the whole sample surface, thus enhancing the accuracy of the collected information and the time resolution of the experiment.

3.2 TILTING SCHEME

The first evidence of pulse front tilting after beam dispersion in a prism was observed by Topp and Orner and dates back to 1975 [114], while the same phenomenon after diffracting from a grating was reported by Schiller and Alfano in 1980 [115]. It has later been implemented to generate amplified spontaneous emission pulses in dye solutions by Polland [116] and Bor [117] in 1983. Further on, pulse front tilt have been employed to better syncronize the pump excitation in extreme ultraviolet (XUV) [118] and X-rays lasers [119], to enhance achromatic phase matching [120–122] and to generate THz pulses by mean of optical rectification [123–126]. A further and more detailed reviews concerning the application of tilted pulse front and angular dispersion can be found in [127, 128].

The employment of a tilting scheme in Ultrafast Electron Diffraction in reflection geometry has been reported for the first time by Baum *et al.* in 2006 [129]. As shown there, the proper pulse front tilt α depends on both the electron velocity v_{el} and the light velocity c and

on some other geometrical considerations, according to the following equation:

$$\alpha = \frac{\pi}{2} - arctan\left(\frac{v_{el}cos(\beta)^{-1}sin(\gamma - \beta)}{c - v_{el}cos(\beta)^{-1}cos(\gamma - \beta)}\right)$$ (3.2)

where α is the front tilt angle, β the sample tilt and γ the incidence angle between the pump pulse and the sample surface. Considering v_{el} = 0.33 c, γ = 90°and β= 3°, the resulting proper tilting angle is α = 71.4°.

To achieve a properly tilted pulse wavefront, the employment of a dispersive element (a grating or a prism) combined with an imaging system (a mirror or a lens) is required [130–132]. For femtosecond laser applications, a grating is the better option to avoid the temporal broadening of the pulse.

A single wavelength λ impinging on a grating is diffracted following the so-called grating equation [115, 133]:

$$m\lambda = d(sin(\theta_{in}) - sin(\theta_{out}))$$ (3.3)

where d is the groove spacing of the grating (*i.e.* $\frac{1}{n}$ with n the number of grooves per unit of length) and m is the diffraction order. θ_{in} identifies the angle between the incoming direction of the light pulses and the normal to the grating surface, while θ_{out} is the angle between the normal to the surface of the grating and the outgoing direction of the beam. Due to the dispersion properties of the grating, different wavelengths λ are diffracted at different angles θ_{out}. In the whole dissertation, the angles related to the grating surface (θ_{in} and θ_{out}) are expressed as respect to the normal to the grating surface.

As direct consequence of eq. 3.3, the outgoing angle θ_{out} can be computed by the relation:

$$\theta_{out}(\lambda) = arcsin\left(\frac{m\lambda}{d} - sin(\theta_{in})\right)$$ (3.4)

As visible in Fig. 3.2, a front tilt is introduced in light pulses diffracting from a grating due to different path length amongst the different regions of the beam. This difference in path length Δy can be evaluated as:

$$\Delta y = y_2 - y_1 = D(sin(\theta_{in}) - sin(\theta_{out}))$$ (3.5)
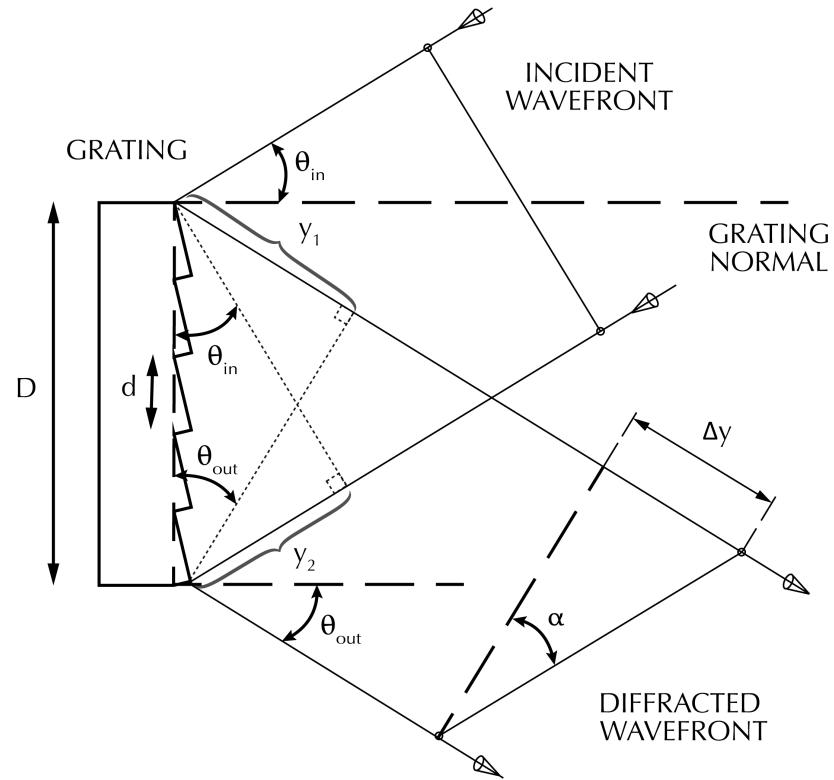
Figure 3.2: Pulse front tilt caused by the diffraction of a single wavelength component of an optical beam incident on a grating at an oblique angle of incidence. Readapted from [115].

Inserting eq. 3.3 in 3.5 we obtain:

$$\Delta y = D\frac{m\lambda}{d} \tag{3.6}$$

From which we can compute the tilting angle α as:

$$\alpha = arctan\left(\frac{m\lambda}{d \cdot cos(\theta_{out})}\right) \tag{3.7}$$

Generalising for the case of pulses with an associated bandwidth, and considering only the first order diffraction ($m = 1$) this pulse front tilt angle α is linked to the angular dispersion caused by the diffraction grating by the relation:

$$\alpha = arctan(\psi\lambda_0) \tag{3.8}$$

where ψ is equal to:

$$\psi = \left(M\frac{\partial\theta_{out}}{\partial\lambda}\bigg|_{\lambda_0}\lambda_0\right) \tag{3.9}$$

Here, M is the magnification factor of the imaging element and λ_0 is the central wavelength of the fs-laser pulses.

The subsequent spatial separation of the different wavelengths of the spectrum is compensated by the imaging element, which projects at a lens-to-sample distance the image of the pulse at the grating surface. This image can be magnified or demagnified, according to the value of M.

However, it has been demonstrated that dispersive elements such as gratings induce a substantial inhomogeneous temporal chirp in short pulses [131]. A tilted pulse with tilting angle $\alpha = 71.9°$, if produced at a grating configuration that is close to Littrow's conditions ($\theta_{in} = \theta_{out} \simeq 53°$ on the grating) and $M = 1$, acquires a temporal broadening $\tau \approx 1$ ps at already 1 mm distance from the centre of the beam - thus developing the so-called *bone shape*, as demonstrated in [134] and visible in Fig.3.3.

This temporal chirp should be compensated by the imaging element, but it has been observed in [134, 135] that this is only true for a small region of the tilted beam, when the grating and the object plane of the imaging element are not coplanar. In these conditions, not every point of the beam profile will enter the lens at the correct grating-to-lens distance, due to a small mismatch in the length of the
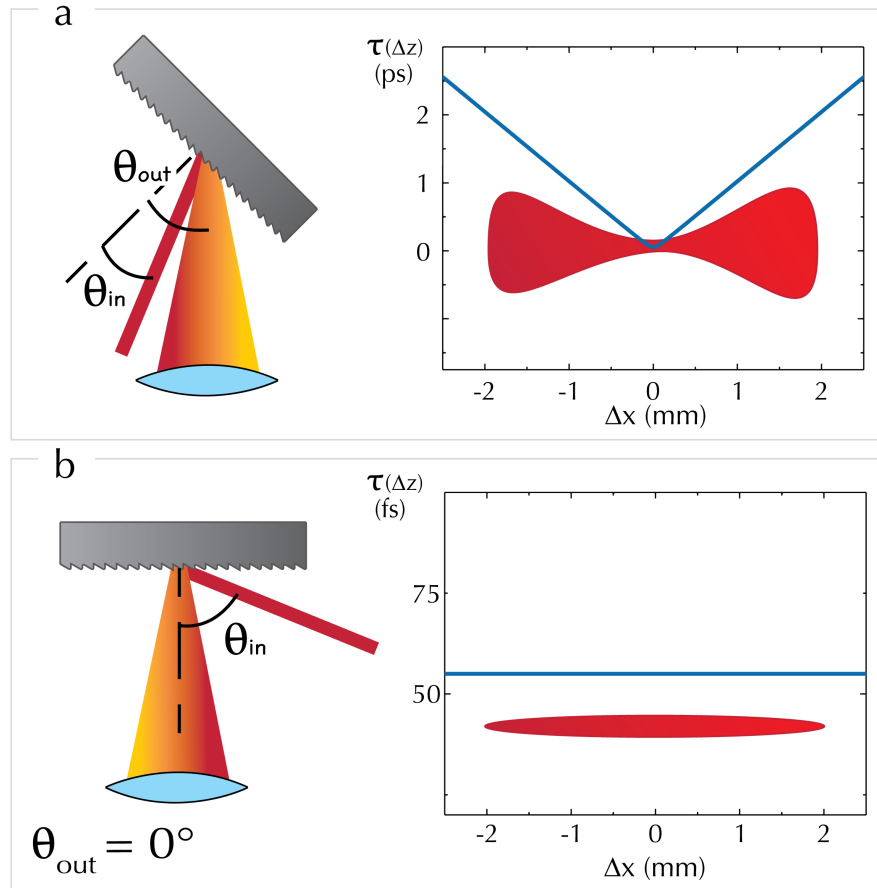
Figure 3.3: Temporal distortion as a function of the coplanarity between grating and object plane of the imaging system. (a) Geometric schematics and relative pulse temporal chirp for the so-called *bone shaped* beam. (b) Geometrical schematics and relative pulse temporal expansion of the beam in che case where the grating and the object plane of the imaging object is coplanar. As visible, the pulse duration remains the same all along the pulse dimension. Figure reinterpreted from [134].

pathways for the dispersed wavelengths. Assuming that the center of the beam enters the lens at the correct grating-to-lens distance, at a lateral position Δx from the centre of the pulse - which has a size of typically a few mm related to the required sample size in grazing-incidence diffraction experiments - the grating-to-lens distance is increased or reduced by a factor:

$$\Delta z = \Delta x \cdot tan(\theta_{out}) \tag{3.10}$$

At this acquired distance Δz, the pulse is concerned by a temporal chirp described as follows [131, 134]:

$$\tau(\Delta z) = \tau_0 \sqrt{1 + \frac{(2ln2)^2 \Delta z^2 \psi^4 \lambda_0^6}{\pi^2 c^4 \tau_0^4}} \tag{3.11}$$

where τ_0 is the Fourier-limited duration of the laser pulse before the dispersive element.

This temporal chirp can be avoided by maintaining the coplanarity between the grating surface and the object plane of the imaging element (*i.e.* having an outgoing angle from the grating $\theta_{out} = 0°$). As shown by Kreier and Baum in [134], with this configuration the imaging element can properly compensate for the temporal chirp all along its entire longitudinal dimension (See Fig. 3.3).

Nevertheless, the achieved tilting angle with this configuration is $\alpha \approx 61°$ and thus not optimal for the application in a UED setup in reflection geometry empowered by 30 keV electrons. Moreover, the higher deviation from Littrow's conditions on the grating surface is used, the less efficiency, defined as $\eta = P_{out}/P_{in}$ (where P_{in} and P_{out} are the incoming and outgoing beam power, respectively) is achieved. When practically implemented, this decrease in the system efficiency, combined with the relatively big footprint of the tilted beam, does not provide the sufficient fluence to photo-excite typical observable dynamics in condensed matter.

What we propose in this chapter is a modified tilting scheme which is able to deliver femtosecond light pulses with a pulse front tilt angle of $\approx 70.7°$ and an overall temporal width of better than 250 fs. This setup allows femtosecond resolution in U-RHEED experiments on mm-sized crystals. Its effectiveness has been proved by means of two characterizations, an optical cross-correlation measurement and a direct electron-laser temporal coincidence characterization based on a plasma lensing effect [136, 137], (see section 3.3.1 and 3.3.2).

Figure 3.4: Simulation of the temporal expansion of the tilted beam at $\sim$ 1.25 mm from its centre as a function of the entrance angle θ_{in} and the de-magnification factor M of the imaging object, for gratings with n = 1200 (panel a) and 2000 (panel b) grooves per millimetre. The black areas defines the sets of parameters that do not provide a tilting angle α = 71.4° $\pm$ 1° and a beam dimension fitting to the geometrical constraints of the experimental chamber. None of the two considered gratings provides a suitable sub-ps temporal chirp of the pulse.

3.2.1   *Iterative design approach*

As reported in chapter 1, the light source in our experiment is a KM-Labs Wyvern Ti:sapphire amplified laser, delivering 50 fs pulses with a pulse energy of 700 µJ at central wavelength $\lambda_0 \approx$ 800 nm with a bandwidth $\Delta\lambda \approx$ 40 nm and repetition rate of 20 kHz.

As explored in the previous section, multiple parameters can influence a pulse front tilt, such as the already mentioned θ_{in} and θ_{out} at the grating surface, its spacing parameter d, the consequent angular dispersion and the magnification factor M introduced by the imaging element. In addition, there are also other parameters to take into account, such as the efficiency of a given diffraction order and the mechanical limitations related to the experimental setup. In our case, a lens-to-sample distance compatible with the geometry of out experimental chamber and the dimension of the dispersed beam at the entrance of the vacuum chamber to fit through the window.

The only way to take into account the high amount of variables and constraints involved while identifying the best compromise between the sensitive parameters (*i.e.* a suitable tilt front α, a proper efficiency η and the shortest pulse temporal chirp possible $\tau(\Delta z)$) in the design of the optimal pulse front tilt is to perform an iterative calculation. Three gratings with different spacing parameters (n = 1200, 1800 and 2000 grooves/mm) have been evaluated.

For a given grating grooves spacing, the outgoing beam direction $\theta_{out} = f(\theta_{in})$ - as defined in eq. 3.4. This reduces the independent variables to two: θ_{in} and the magnification factor M. Thus, we considered all the possible combinations of θ_{in} and magnification M, and for each of them the resulting pulse front tilt α was computed. Suitable
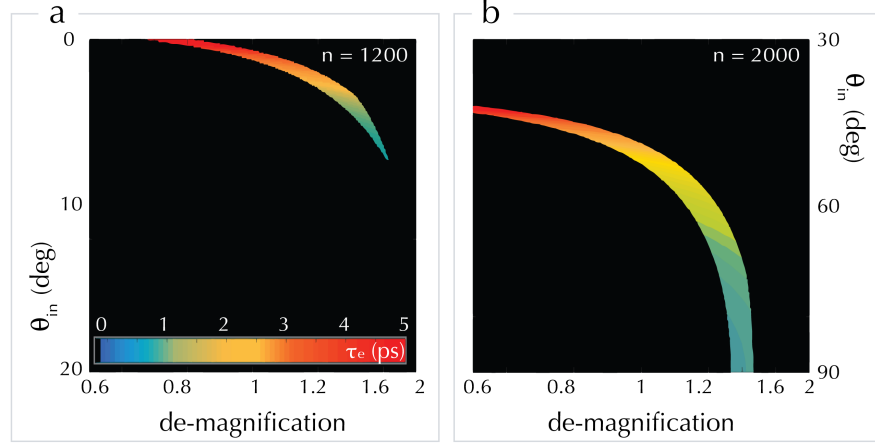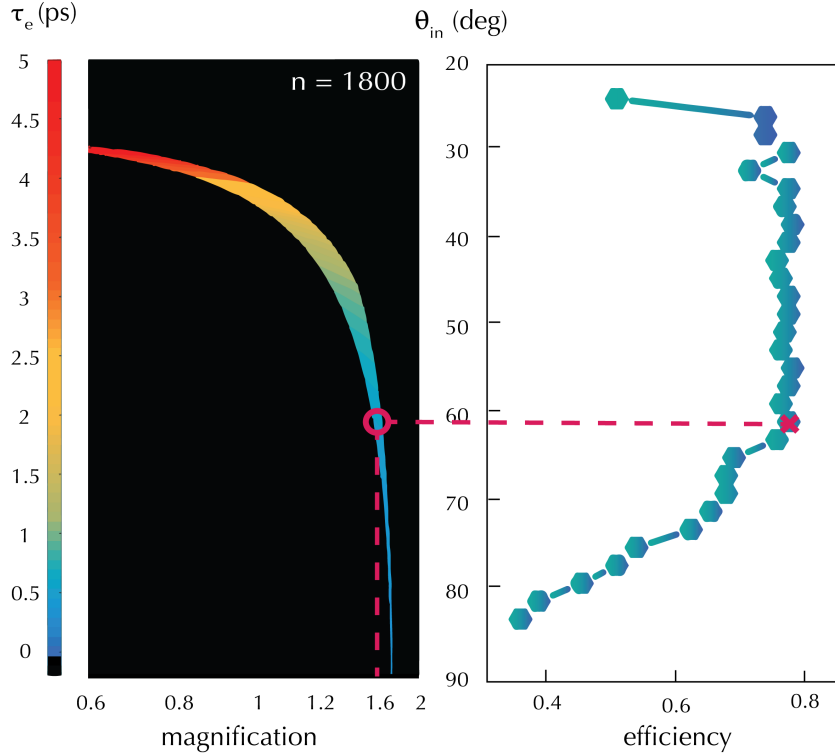
Figure 3.5: Simulation of the temporal expansion of the tilted beam at ∼ 1.25 mm from its centre as a function of the entrance angle θ_{in} and the de-magnification factor M of the imaging object, for a grating with n = 1800 grooves per millimetre and an imaging object with f = 200 mm (left-hand side). The black areas defines the sets of parameters that do not provide a tilting angle α = 71.4° ± 1° and a beam dimension fitting to the geometrical constraints of the experimental chamber. Since the grating with n = 1800 grooves/mm provides a suitable temporal chirp of the tilted beam, its efficiency as function of θ_{in} was measured (right-hand side). The parameters providing the best trade-off between temporal chirp and efficiency is defined by the red circle and constitutes the final parameters of our tilting scheme.

solution of this process were the ones fulfilling at the same time the three selected constraints: the desired tilting angle α = 71.4°±1°, the lens-to-sample distance $i \geq$ 22.5 cm, and the longitudinal dimension of the beam fitting the chamber window, 10 cm.

For each combination of the parameters, the temporal chirp τ_e at the extremity of the tilted beam ($\approx$ 1.25 mm from the pulse center) was computed by means of the equation 3.11, and it is reported as 3D map in figures 3.4 and 3.5. Black areas in the maps correspond to combinations of parameters not satisfying the aforementioned constraints. As shown in the figure, only few combinations of the two independent variables can provide a suitable pulse front tilt, and only employment of the grating with n = 1800 grooves/mm results in a sub-picosecond temporal chirp for the pulse.

Once selected the suitable grating, the power efficiency of the zero order diffraction was measured (see Fig. 3.5) and adopted as additional sensitive parameter. We have thus identified as the best compromise between the achievable time chirp of the tilted pulse (sub-500

fs at 1.25 mm from the center of the beam) and the power efficiency of the system (η = 0.8) the following parameters: an off-Littrow configuration with θ_{in} = 61° and θ_{out} = 35°, a grating-to-lens distance p = 52 cm, a lens-to-sample distance i = 32.5 cm and thus a demagnification factor M = 1.6 (this configuration is highlighted by the red circle in Fig. 3.5). The evaluated pulse front tilt for this parameters configuration is α = 70.7°.

During the design and optimization process, we only considered an imaging system with focal length f = 200 mm because of the geometrical constraints of the setup, as shorter focal lengths cannot comply with the lens-to-sample distance constraint while longer focal lengths cannot meet the windows opening dimension and need high-diameter imaging optics. A sketch of the final tilting scheme is presented in Figs. 3.6 and 3.8.

3.3   TILTING CHARACTERIZATION

3.3.1   *Optical Characterization*

The obtained tilted pulse has been optically characterized by means of the cross-correlation method demonstrated in [134]. As presented in Fig. 3.6a, a 50:50 beam splitter divides the collimated beam coming from the light source in two portions: one is used to generate the tilted beam, while the other is used as a reference beam. The first portion is directed through the cylindrical lens and subsequently on the grating to generate the tilted beam, according to the scheme explained above. It is delayed with respect to the non-tilted reference beam by means of a retroreflector mounted on a movable linear stage. A β-barium-borate (BBO) crystal with a thickness of 200 μm is positioned at the lens-to-sample distance in our experiment, i = 32.5 cm. The imaging lens (f = 200 mm) generates a 3.5x0.2 mm² FWHM spot size at the BBO surface. The non-tilted reference beam is directed through a cylindrical lens providing a linear focus with dimension 4.5x0.2 mm² on the BBO surface, in a slightly noncollinear geometry with an angle of 2-3° (y-z plane) with respect to the tilted beam (see Fig. 3.6b).

As the 800-nm pulses interact with the BBO crystal, two individual contributions at 400 nm are generated, corresponding to the second harmonic of both the reference and the tilted beams (Fig. 3.7a, above and below, respectively). The residual 800-nm light is filtered out by the use of a chromatic filter. When spatiotemporal overlap is achieved on the nonlinear crystal, a third contribution is generated, representing the cross-correlation of the two incoming beams. At a given time delay, only a small region of the tilted pulse is temporally overlapped with the untilted reference beam. Consequently, the spatial profile of the cross-correlation signal corresponds to a narrow stripe. The non-collinearity of the two incoming beams allows the cross-correlation signal to not overlap spatially with the individual
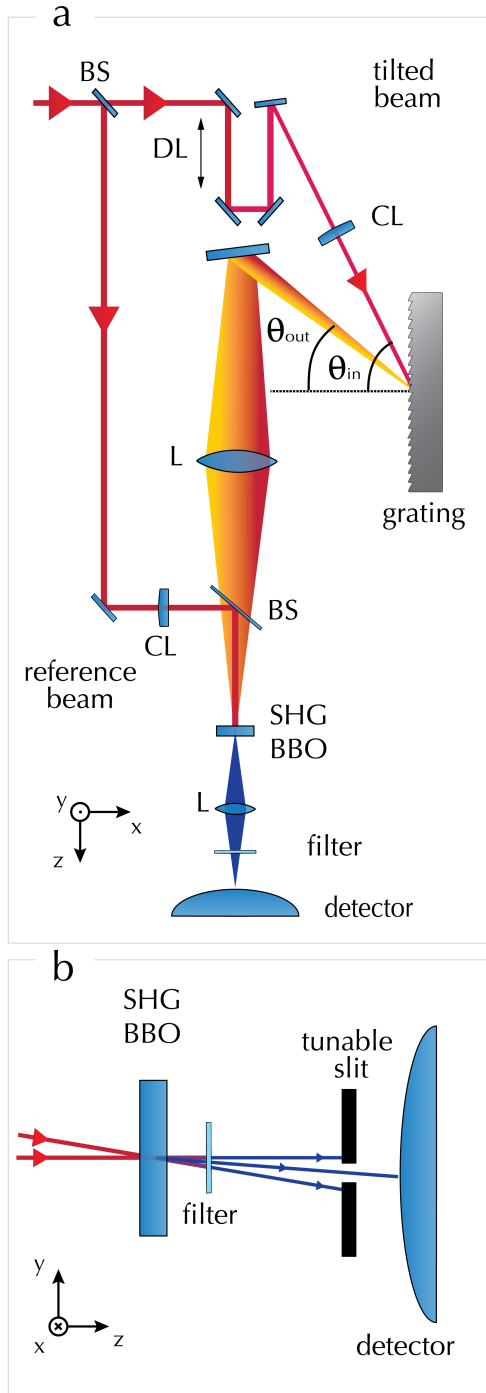
Figure 3.6: Optical characterization of the tilted laser pulse with λ_0 = 800 nm. (a) Experimental scheme to cross-correlate the tilted pulse with an untilted reference, as performed in [134]. BS represents a 50:50 beam splitter, CL cylindrical lens, DL the delay stage and SHG BBO the nonlinear crystal responsible for the generation of the second harmonic, λ = 400 nm. The two angles used in our tilting setup are θ_{in} = 61° and θ_{out} = 35°. The y-axis indicates the out-of-plane direction. (b) Detail of the Second Harmonic Generation (SHG) cross-correlation, reported on the y-z plane.
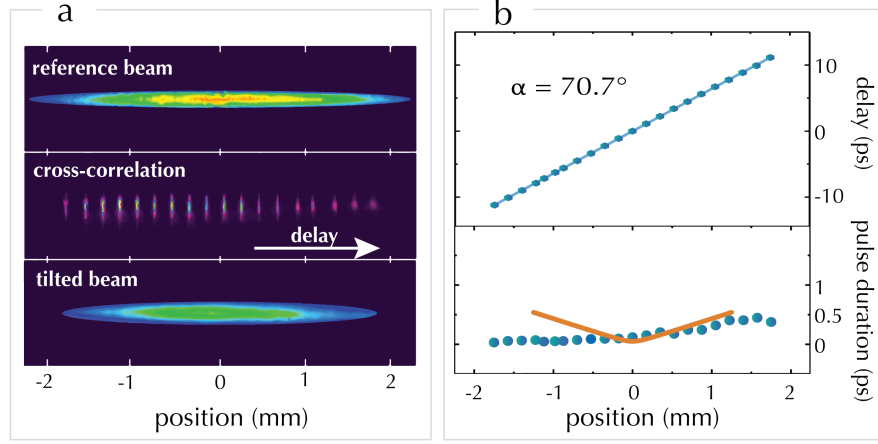
Figure 3.7: (a) Pictures of the 400 nm contributions taken by the camera: the second harmonic of the untilted beam (top), of the tilted beam (bottom) and their cross-correlation measured at different delays (middle panel). (b) Front tilt (top) and duration (bottom) of the pump beam from measured data (blue circles) and the calculation (orange solid line).

contributions, which are removed after the crystal making use of a tunable slit (see Fig. 3.6b).

A progressive delay scan provides a left-to-right shift of the cross-correlation signal. The cross-correlation signal obtained at different delays is shown in Fig. 3.7a, middle panel. The position and width of this signal during the scan provide information on the tilt angle and on the pulse duration at a defined longitudinal position, respectively [134]. Figure 3.7b (above) shows the measured pulse front tilt, that we observed to be a straight line with an angle of 70.7° with respect to the horizontal. Fig. 3.7b (below) contains the measured tilted pulse duration (blue circles) as a function of the distance from the centre of the beam toward the edges, as compared to the calculated pulse duration (orange solid line). Despite the small deviation from the ideal tilting angle (71.4°), a substantial agreement between experimental data and calculation is observed, confirming also that the temporal chirp of the tilted pulse is well compensated and it is smaller than 250 fs ($\simeq$ the time resolution of our electron probe [33]) for more than 80% of the tilted pulse longitudinal dimension. The mismatch between the data and the computation is imputed to the model implemented, which was not taking into account the depth of focus of the Gaussian beam, and its asymmetry to a slight deviation of the grating-to-lens distance to the optimal one.

3.3.2 *In Situ Characterization*

The tilting optics have been subsequently integrated into our UED set-up (see Fig. 3.8). In order to characterise the tilting at the sample position *in situ*, we adopted the method demonstrated by Baum *et al.* in [129]. A copper needle (apex size = 100 μm) is placed on the sample holder such that it crosses the propagation path of the elec-

trons. By changing the focus of the electron beam by means of the second magnetic lens, a shadow image of the needle is projected on the CCD camera, as visible in figure 3.9a. When hit by the pump pulse, a transient and localised plasma is generated on the needle surface by multiphoton ionisation and successive thermionic emission [136] and distorts the spatial profile of the incoming electron beam (so-called plasma lensing effect [137]).

A detailed study of the phenomenon have been reported in [136], where by means of electron shadowgraphy the authors reported the direct visualization of the electromagnetic field generated by the photoexcitation of a copper surface. However, in our case the light induced photoemission process have been used with the sole purpose of determining t_0 in the URHEED configuration in our experimental setup, without deepening the discussion into further detail about how the electromagnetic field is generated and evolve from the copper tip.

In our study, every image reported is obtained by averaging 20 acquisitions of 250 shots, containing $\sim 10^5$ electron each. Figure 3.9a contains a temporal sequence of the *plasma lensing effect*. A strong laser pulse is directed on a copper needle and thus generates a transient and localized plasma, which interacts with the propagating electron bunch inducing a sizeable distortion of its spatial profile. This distortion is recorded by our CCD camera as a shadow image of the photoemitted electron cloud. We evaluated the dynamics of the phenomenon by means of the cross-correlation factor reported in [136, 138] and formulated as follows :

$$\Gamma(t', t) = \frac{\sum_{x,y} C_{x,y}(t) C_{x,y}(t')}{\sqrt{\sum_{x,y} C_{x,y}(t)^2 \sum_{x,y} C_{x,y}(t')^2}} \tag{3.12}$$

where the contrast $C_{x,y}$ corresponds to:

$$C_{x,y}(t) = \frac{I_{x,y}(t) - \bar{I}(t)}{\bar{I}(t)} \tag{3.13}$$

with $I_{x,y}(t)$ being the intensity of the pixel at the position (x, y) and time t, and $\bar{I}(t)$ the average of $I_{x,y}(t)$ for the entire figure. This two-dimensional cross-correlation coefficient can effectively compare different intensity features at two different time delays while not being affected by absolute variations in intensity due to the noise of the laser. From the evolution of the retrieved cross-correlation factor, we can observe that in our experiment the maximum screening effect occurs at $t = 30$ ps, as visible in figure 3.9a, while subsequently the electron cloud continues its isotropic expansion. The complete recovery of the initial conditions is achieved only after ~ 150 ps.
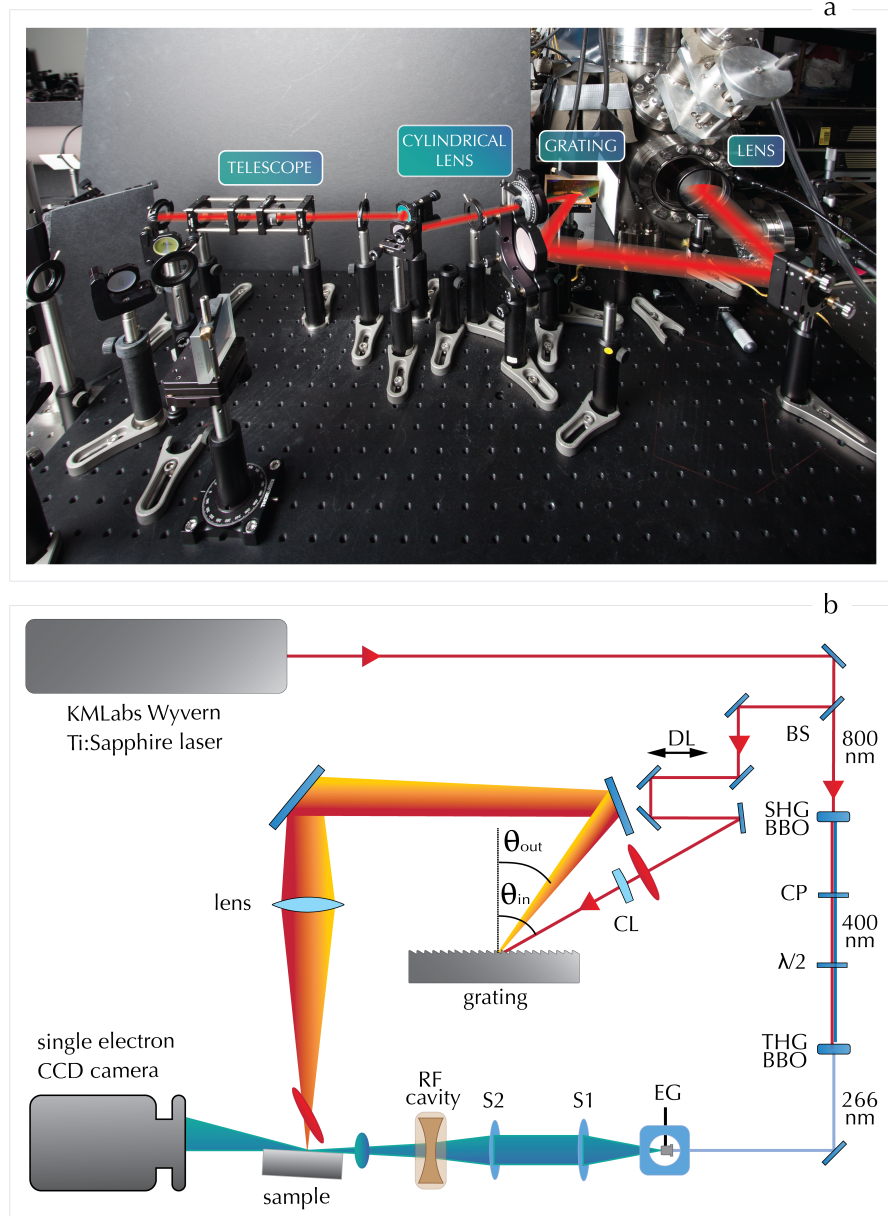
Figure 3.8: Actual implementation (a) and schematic representation (b) of the tilting scheme implemented in the UED setup. BS represents a 90:10 beam splitter, DL the delay stage, CL a cylindrical lens, SHG and THG BBO the nonlinear crystals responsible for second and third harmonic generation, CP the group delay compensation plate, $\lambda/2$ the dual wave-plate, EG the electron gun, S1 and S2 a collimating and a focusing electronic lens, RF cavity our radio-frequency cavity operating in TM_{010} mode.
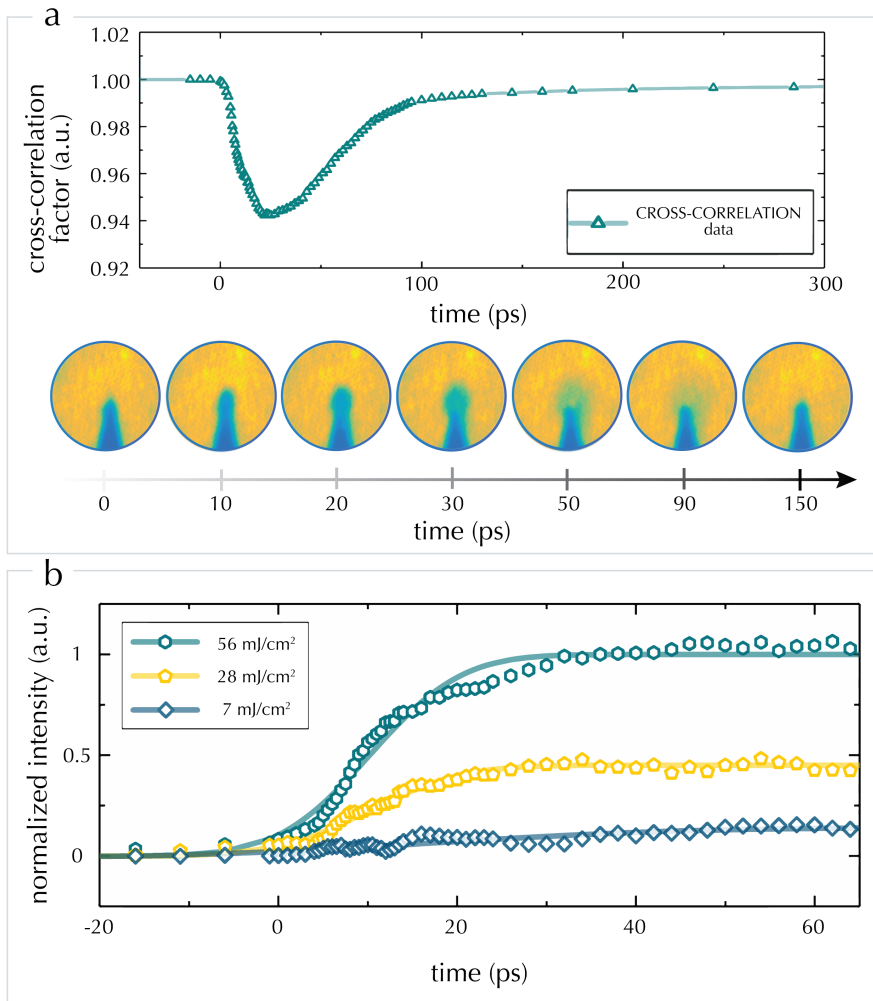
Figure 3.9: (a) Temporal evolution of the *plasma lensing effect* phenomenon on a copper tip. Cross-correlation function of the effect (above) and direct images (below) as a function of time. (b) Fluence dependence of the *plasma lensing effect*, evaluated for fluence values of 7 (blue), 28 (yellow) and 56 (green) mJ/cm². The considered parameter consists in the amplitude of the gaussian fit of the dip created by the plasma lensing effect in the images.
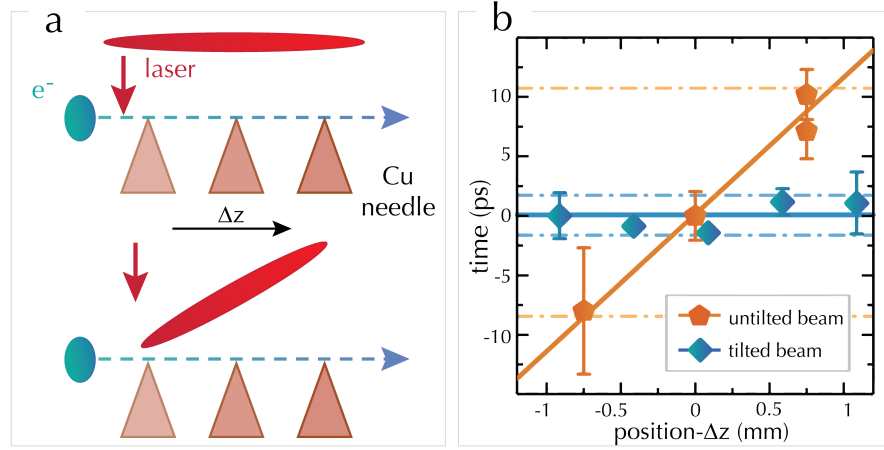
Figure 3.10: (a) Schematics of the *plasma lensing effect* experiment as also performed in [129]. A strong laser pulse is directed on a copper needle and thus generates a transient and localized plasma, which interacts with the propagating electron bunch inducing a sizeable distortion of its spatial profile. This lensing effect allows to define the time zero, t_0, for a given position of the needle, which is then moved along the electron propagation direction. The results of this experiment for the two cases of not tilted (orange) and tilted (blue) pump beam are shown in (b), where the position of t_0 is plotted as a function of the needle position.

To evaluate the insurgence of the studied phenomenon, we fitted with a gaussian function the intensity dip provoked in the image by the *plasma lensing effect* at three different fluences: 7, 28 and 56 mJ/cm^2 (see Fig. 3.9b). We identify the lowest fluence as slightly above the photoemission threshold: lower fluences have shown no effect on the cross-correlation analysis. The difference in fluence does not influence the time-scale of the insurgence of the phenomenon, consistently with the nature of multiphoton ionization. Conversely, the fluence affects the amount of photoemitted electrons and thus the entity of the observed effect.

The relative change in each image with respect to a reference image taken before the excitation allows the determination of time-zero, t_0, with a precision of ~ 1 ps [129, 137, 139]. During the experiment, the position of the needle is varied along the propagation direction of the electron beam, and the value of t_0 is measured for each spatial coordinate. We performed the experiment with both the tilted pump pulse and with an untilted reference pulse. As schematically shown in Fig. 3.10a (above) and derived from the experimental data in Fig. 3.10b (orange pentagons), when using the untilted pump the electron pulse overlaps at different times for different positions of the needle, showing an expected dispersion of 10 ps/mm. Instead, when using the tilted beam configuration, the t_0 position remains constant for any position of the needle in the measured range of ~ 2 mm (see schematics in Fig. 3.10a (below) and blue diamonds in Fig. 3.10b).
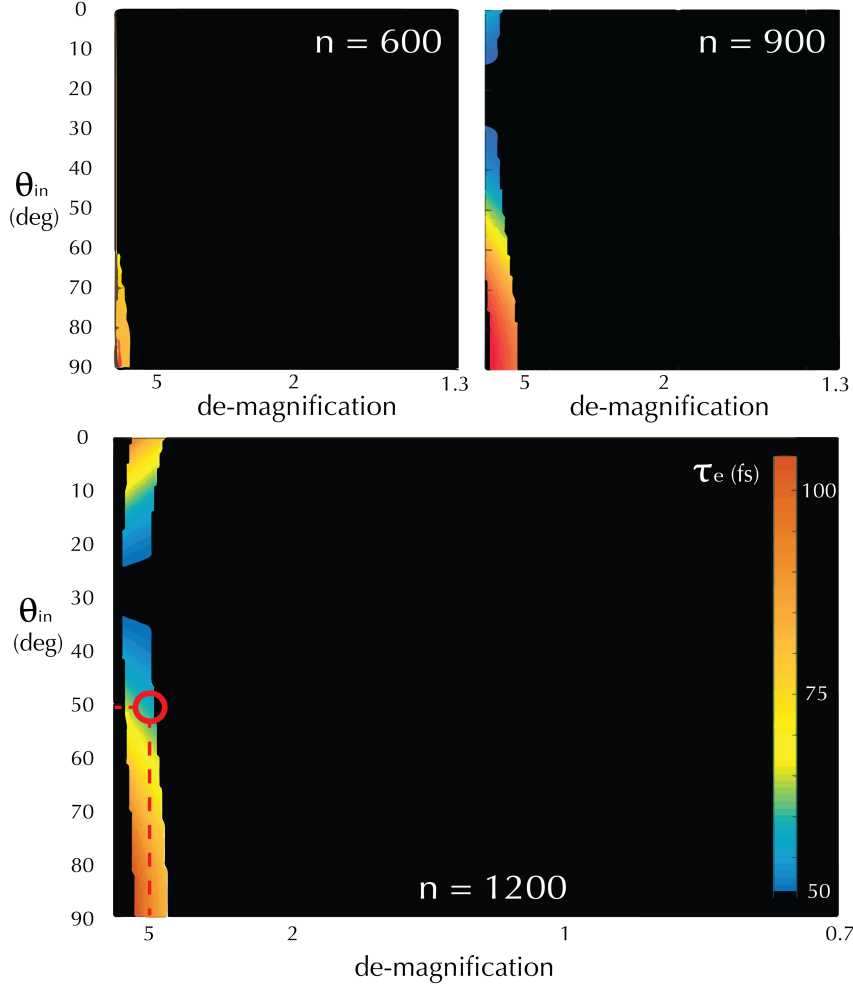
Figure 3.11: Simulation of the temporal expansion of the tilted beam at ~ 1.25 mm from its centre as a function of the entrance angle θ_{in} and the de-magnification factor M of the imaging object, for gratings with $n = 600$, 900 and 1200 grooves per millimetre. The black areas defines the sets of parameters that do not provide a tilting angle $\alpha = 71.4° \pm 2°$ and a beam dimension fitting to the geometrical constraints of the experimental chamber. Only the grating with $n = 1200$ shows a suitable configuration (highlighted by the red circle) but only at the expense of a high demagnification factor.

3.4 TILTING DESIGN AND IMPLEMENTATION FOR $\lambda = 400$ NM

In order to extend the potential of the URHEED setup and to introduce a flexibility in the pump energy, which would allow us to excite materials on different absorption features, we design and implement in our beam-line a tilting scheme for the second harmonic of the fundamental $\lambda_0 = 800$ nm, $\lambda_0 = 400$ nm.

We adopted the very same iterative approach reported in section 3.2.1 for $\lambda_0 = 800$ nm, to evaluate the best compromise amongst the different sensitive parameters and constraints involved. Three gratings with different spacing parameters ($n = 600$, 900 and 1200 grooves/mm) were considered. As visible from figure 3.11, the gratings with $n = 600$ and 900 grooves/mm are not suitable due to

the configuration required. Conversely, the grating with n = 1200 grooves/mm gives the possibility to realize a proper pulse front tilt also for $\lambda_0 = 400$ nm, even if at the expense of a high demagnification factor.

The final parameters for the tilting scheme are an off-Littrow configuration with θ_{in} = 50° and θ_{out} = 17°, a grating-to-lens distance p = 120 cm, a lens-to-sample distance i = 24 cm and thus a demagnification factor M = 5 (this configuration is highlighted by the red circle in Fig. 3.11 and rendered in Fig. 3.12a). The evaluated pulse front tilt for this parameters configuration is $\alpha = 69.9°$.

Similarly to what done in the case $\lambda_0 = 800$ nm, we try to perform both an all-optical and a crossed light-electron *in situ* characterisation. The optical characterisation can be done *via* Sum Frequency Generation (SFG), where the tilted 400 nm pulse cross-correlated with an untilted reference 800 nm pulse. The frequency sum at 266 nm would be monitored as a function of the reciprocal delay between the pulses and the spatio-temporal information concerning the 400 nm pulse retrieved.

On the example of the previous case, we tried to perform an optical characterisation through Third Harmonic Generation (THG) and an *in situ* photoemission experiment. However, due to the low fluence achievable with the 400-nm configuration, neither one or the other of the procedures was suitable to fully characterise our tilted beam. The implementation of the tilting system in our beamilne is visible in figure 3.12b).

3.5 CONCLUSIONS AND FURTHER THINKING

In conclusion, by means of an iterative calculation approach, we have been able to identify and develop an optimal optical tilting scheme for ultrafast electron diffraction working in reflection geometry with 30 keV electrons, both for pump pulse at $\lambda_0 = 800$ nm and $\lambda_0 = 400$ nm. The multiple experimental characterizations reported in this chapter for the $\lambda_0 = 800$ nm case demonstrated the validity of our method, which allowed us to achieve an overall temporal resolution in the sub-500 fs regime while using $10^4 - 10^5$ electrons per pulse in a URHEED scheme. However, this is only valid for the $\lambda_0 = 800$ nm case. The scarce fluence achievable for the $\lambda_0 = 400$ nm pump did not allow to perform the same characterizations performed for the 800-nm pump. Nevertheless, we count on the solidity of the iterative design approach demonstrated for the 800 nm pump to consider this second tilting design reliable at a first approximation. The observation of sub-500 fs dynamics initiated by a 400 nm pump pulse will be the confirmation of the proper tilting configuration also for this pump wavelength. The successful implementation of these pulse front tilt for URHEED pumping, which exhibits surface sensitivity with atomic-scale space and sub-picosecond time resolution, opens the path to
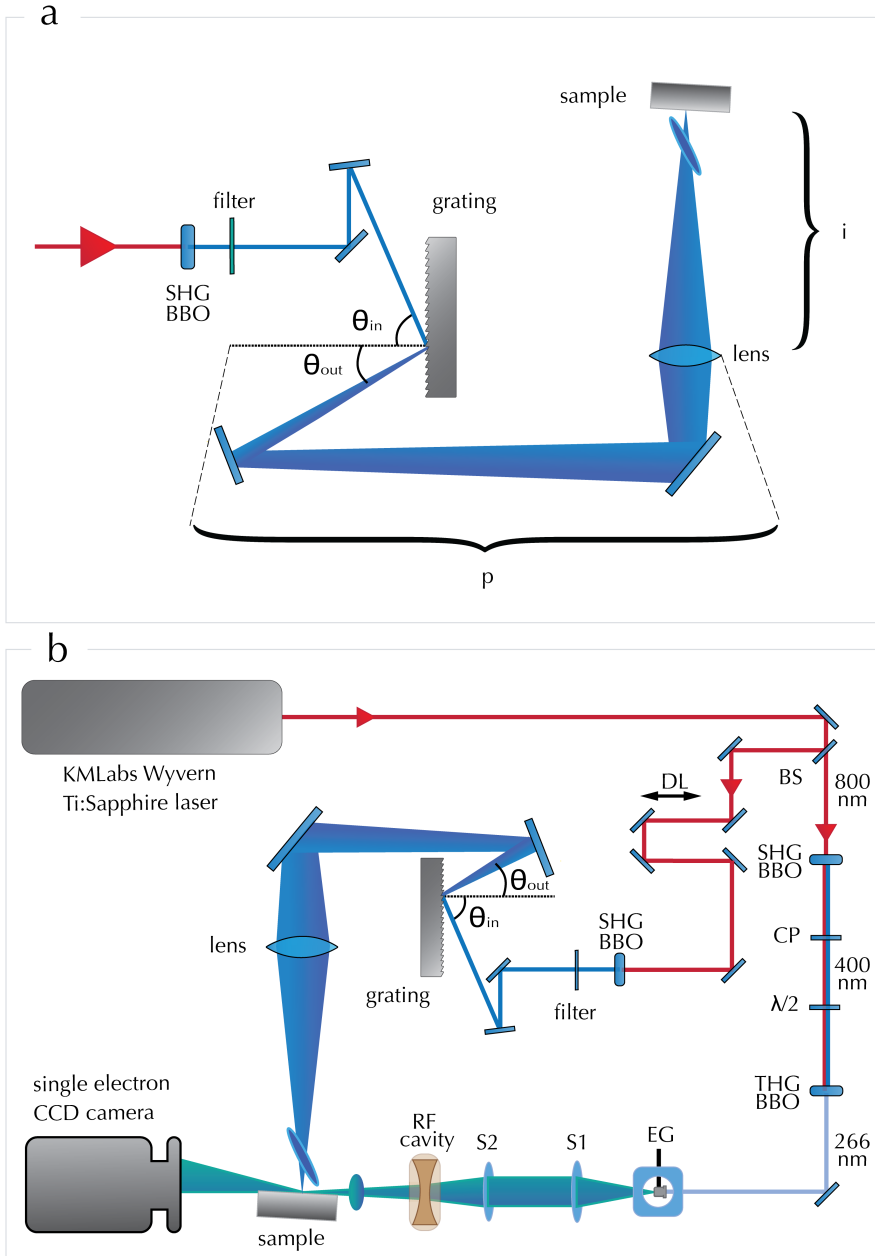
Figure 3.12: Final tilting scheme for $\lambda_0 = 400$ nm (a) and implementation in the UED beamline (b). The optical parameters are $\theta_{in} = 50°$ and $\theta_{out} = 17°$, a grating-to-lens distance $p = 120$ cm, a lens-to-sample distance $i = 24$ cm. BS represents a 90:10 beam splitter, DL the delay stage, CL a cylindrical lens, SHG and THG BBO the nonlinear crystals responsible for second and third harmonic generation, CP the group delay compensation plate, $\lambda/2$ the dual wave-plate, EG the electron gun, S1 and S2 a collimating and a focusing electronic lens, RF cavity our radio-frequency cavity operating in TM_{010} mode.

the sub-500 fs direct observation of the structural dynamics in solids, surfaces and low-dimensional nanoscale systems with this technique. Experimental proofs of what aforementioned will be presented in the next chapters.

However, it is worth noting that the main limitations of the tilting design process are the mechanical constraints involved in his development. As a general consideration, the whole design should be done in parallel with the development of the experimental chamber, in order to take into account the tilting requirements. As a matter of facts, further simulations shows how the absence of the experimental constraints would have allowed more freedom into the tilting scheme development. Moreover, a better trade-off between the sensitive parameters (*i.e.* α, η and $\tau(\Delta z)$) could have been reached. In figure 3.13, we compare the simulations for λ = 800 nm with an imaging object with f = 200 mm combined with gratings with n = 1200 and 1800 grooves/mm with and without the experimental constraints. The grating with n = 2000 grooves/mm is no more considered since it does not allow a sub-ps temporal chirp of the pulse. It is worth noting that, while the simulation is almost unmodified for the grating with n = 1800 grooves/mm, the scenario for the grating with n = 1200 grooves/mm is completely different and would offer a much shorter temporal expansion $\tau(\Delta z)$.

In figure 3.14 we also report simulations for λ = 800 nm for the following cases: a grating with 1200 grooves/mm combined with an imaging object with focal length f = 100 and 300 mm and a grating with 1800 grooves/mm combined with a lens with focal length f = 100 mm. As before, the case of n = 2000 is not reported since it does not present any sub-ps temporal chirp $\tau(\Delta z)$ of the pulse. Again, the riddance of the constraints due to the experimental chamber would allow a more suitable choice of the involved variables in order to obtain the best compromise amongst the sensitive parameters. In particular, the elimination of the lens-to-sample constraint $i \geq 22.5$ cm allows the use of imaging optics with f = 100 mm, whose consequential temporal spread is much shorter than the one obtained with the f = 200 mm lens - as visible in figure 3.14 - and thus more suitable for the desired application.
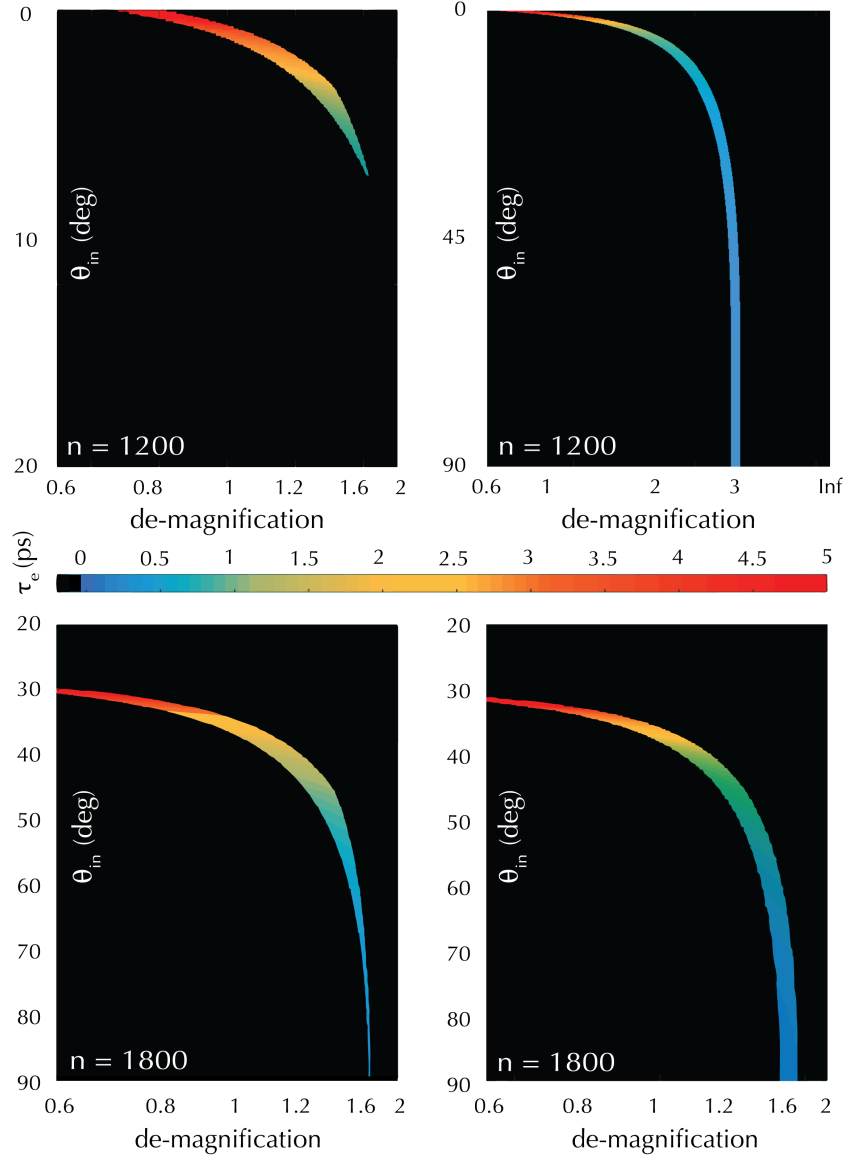
Figure 3.13: Comparison of the simulations of the temporal expansion of the tilted beam at $\sim$ 1.25 mm from its centre as a function of the entrance angle θ_{in} and the de-magnification factor M of the imaging object, for gratings with $n = 1200$ and 1800 grooves per millimetre. The black areas defines the sets of parameters that do not provide a tilting angle $\alpha = 71.4° \pm 1°$ and a beam dimension fitting to the geometrical constraints of the experimental chamber. On the figures on the right-hand side, only the tilting angle is kept as a constraints.

Figure 3.14: Ideal simulations (*i.e.* without geometrical constraints) of the temporal expansion of the tilted beam at $\sim$ 1.25 mm from its centre as a function of the entrance angle θ_{in} and the de-magnification factor M of the imaging object, for the following grating and imaging focal length parameter: $n = 1200$ grooves/mm and $f = 100$ mm (above), $n = 1800$ grooves/mm and $f = 100$ mm (middle) and $n = 1200$ grooves/mm and $f = 300$ mm (below). The black areas defines the sets of parameters that do not provide a tilting angle $\alpha = 71.4° \pm 1°$.

4
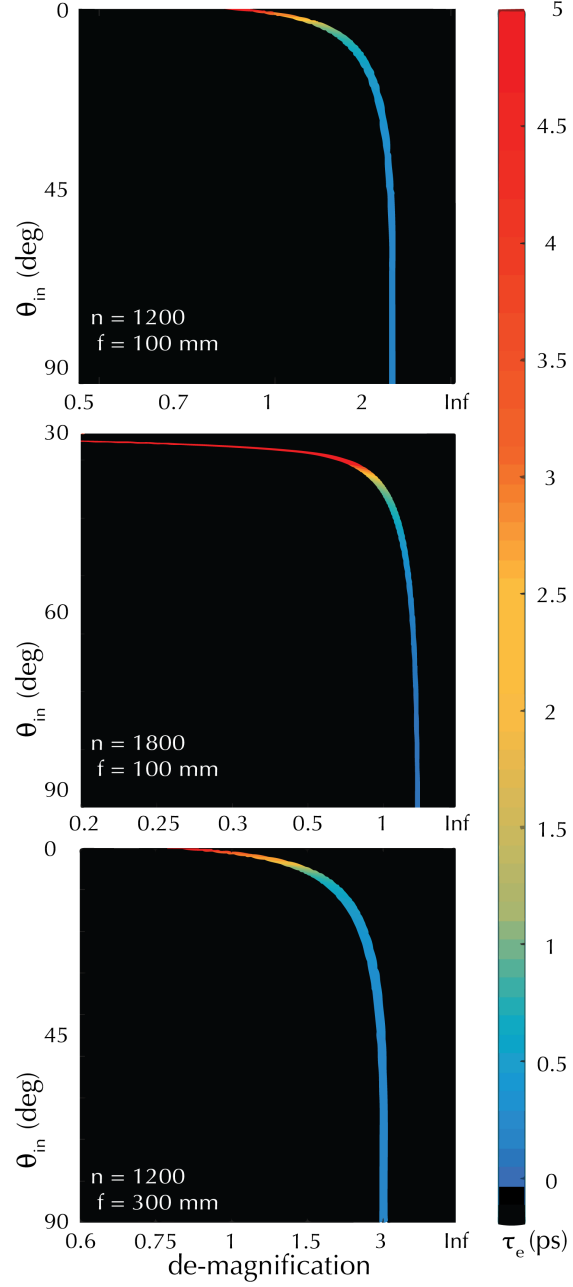
ELECTRON-PHONON COUPLING IN GRAPHITE

This chapter is based on the article by F. Pennacchio *et al.*, *Design and implementation of an optimal laser pulse front tilting scheme for ultrafast electron diffraction in reflection geometry with high temporal resolution.* [113]. An extended introduction is added and more data are presented and discussed.

4.1 GRAPHITE: AN INTRODUCTION

Carbon is the 6th element in the periodic table and also the sixth estimated element in the universe, after hydrogen, helium, oxygen, neon and nitrogen. On planet Earth, despite it is only a minor component in the crust, it can be found in many different forms and compounds, ranging from minerals (magnesium and calcium carbonates, dolomites, marble etc.), biogenetic materials (corals, invertebrates exoskeleton and shells), to organic compounds in fossil fuels and natural gases. Moreover, via the so-called carbon cycle - a sequence of biochemical mechanisms ranging from photosynthetic fixation of molecular carbon into carbohydrates and their successive in vivo oxidation during metabolism - carbon consitutes the main building block of bio-molecules in living organisms [140].

Elemental inorganic carbon is polymorphic. Its natural allotropes are: amorphous carbon, diamond, graphite and fullerenes. Amorphous - or glassy - carbon does not present a long range crystalline order, while fullerenes consist in a family of carbon-based self-folding macromolecules [141], as for example the renowned C_{60} buckyball or carbon nanotubes. Thus, only graphite and diamond are the crystalline allotropic forms of carbon. Macroscopically, they present divergent physical properties: graphite is one of the softest materials (degree 1.5 in the Mohs classification), is a good electrical conductor, a weak thermal conductor and it's opaque as respect to light. Conversely, diamond is the hardest natural material (degree 10 in the Mohs classification), is an electrical insulator, a good thermal conductor and in its pure form is transparent to light.

Such opposite properties are directly connected to the atomic structure of the two allotropes. In diamond, the carbon bonding involves sp^3 (tetrahedral) hybridisation of the orbitals resulting in a covalent three-dimensional crystal structure with cubic symmetry (Fm̄3m space group). Graphite, instead, is characterised by sp^2 (trigonal) hybridisation of the carbon orbitals forming 2D interconnected carbon hexagons. As a result, its structure consists in carbon layers stacked in an AB

(a) *Graphite crystal in a marble quarry, Kolchholz, Mostviertel, Austria .*

(b) *Hexagonal black crystals on graphite. From Merelani Hills, Manyara Region, Tanzania.*
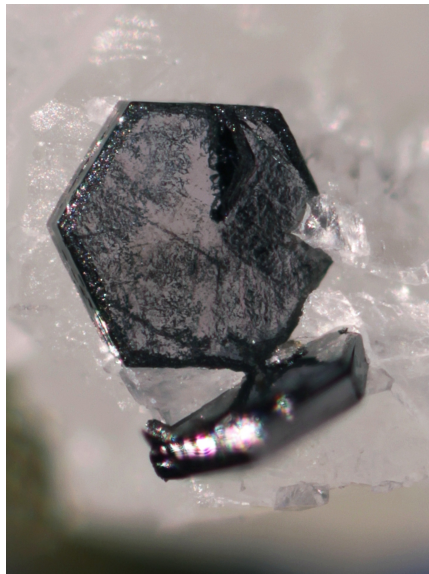
(c) *1-mm graphite crystal. The crystal has well formed hexagonal prism faces, minor pyramidal faces and a small growth twin on the basal plane. From Crestmore, California, USA.*

(d) *Bright dark grey metallic graphite flattened crystal flakes distributed rendomly in quartz. From Lead Hill Mines, Ticonderoga, New York, USA.*

Figure 4.1: Graphite natural crystals. Image courtesy of © Harald Schillhammer (a), © Olaf Dziallas (b), © John A. Jaszczach (c) and © Jean-François Carpentier (d) [142].
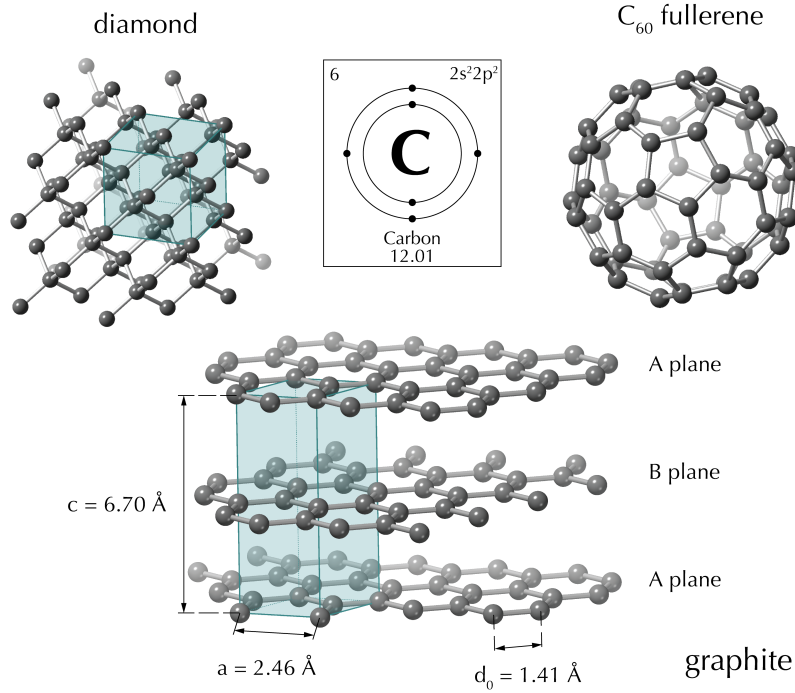
Figure 4.2: Allotropic forms of carbon: diamond, C_{60} fullerene and graphite. In diamond and graphite, the crystallographic unit cell is shown. For graphite, the AB stacking of layer and the unit cell parameters are reported.

sequence characterised by strong cooperative covalent and metallic bonding inside each layer and weak Van der Waals interactions derived by delocalised π orbitals in the out of plane direction [143]. It belongs to the hexagonal $P6_3/mmc$ space group and its cell parameters are a = b = 2.47 Å and c = 6.70 Å, while $\alpha = \beta = 90°$ and $\gamma = 120°$ [144, 145]. In figure 4.1 some examples of natural graphite ores are reported, while figure 4.2 illustrates the atomic structure of carbon allotropes: diamond, fullerenes and graphite.

Due to its structure, graphite is an anisotropic material, thus having strongly different properties in the in-plane or out-of-plane direction. As a result of this anisotropy in the structure, carbon layers can easily reciprocally glide. This makes graphite a good lubricant and pencil material - probably its original application, from which its name (from ancient greek $\gamma\rho\acute{\alpha}\varphi\epsilon\iota\nu$ - to write).

4.2 STRONGLY COUPLED OPTICAL PHONONS

In graphite, Near IR light is known to excite a subset of phonon modes often referred to as Strongly Coupled Optical Phonons (SCOPs) [24]. These modes are primarily high-energy optical phonons [146, 147] which later decay via anharmonic couplings into all other lattice vibrations. The mechanism for their population was first inferred via ultrafast terahertz spectroscopy [148], optical transmission [149] and photoemission [150], clocking their characteristic thermalisation time

within 500 fs. The subsequent anharmonic decay was measured to occur within 6-7 ps. The initial electron-SCOPs coupling in graphite is among the fastest global structural reactions ever measured in a solid, similar to the initial dynamics of VO_2 [17, 151]. However, observation of SCOPs excitation times so far always came from indirect methods that were probing the electronic structure alone. A hint of ultrafast structural rearrangement was obtained in [25] by monitoring the temporal evolution of the Debye-Waller effect of a single crystal of graphite at different fluences. A weak kink in the decay of a certain Bragg peak intensity was observed, but precise interpretation was obstructed by the too low time resolution of that experiment ($\sim$ 700 fs). More recently, UED in transmission geometry have been successfully used to probe the electron-SCOPs coupling temporal evolution in graphite [24]. The observation of the dynamics of the 110 Bragg peak allowed the clear resolution of the aforementioned dynamics. However, the experiment was performed probing the orthogonal direction to the c axis of graphite in a less-than-50 nm thick nanocrystal.

In what follows, we show that our improved pulse-front tilting scheme in combination with the radiofrequency pulses compression technology in our reflection UED set-up allows for the direct structural observation of the characteristic time-scale of 500 fs associated with the population of the SCOPs on the surface of a 3D bulky sample, in excellent agreement with the previously published results.

4.3   MATERIALS AND METHODS

The studied sample is a bulk $10 \times 10 \times 2$ mm^3 AGraphZ Highly Oriented Pyrolytic Graphite (HOPG) sample from Optigraph GmbH [152]. HOPG is a form of synthetic graphite obtained through a pyrolytic process combined with a tensile stress applied to the sample the basal plane direction. The result is a high purity sample where the crystallites of graphites present an high degree of alignment [153]. The identifying parameter in HOPG sample is the mosaic spread, expressed in degree and evaluating the global alignment of crystallites in the sample, lower values meaning a better degree of alignment. The studied sample presented a mosaic spread of $0.4° \pm 0.1°$, which is the highest degree of alignment available in commercial samples. The graphite sample expose the (001) surface. In the following experiments we investigate the (006) Bragg reflection.

The diffraction experiments have been conducted using ultrafast electron diffraction setup at Laboratory for Ultrafast Microscopy and Electron Scattering (LUMES) laboratory at EPFL working in reflection geometry. Ultrashort electron pulses with energy per particle of 30 keV and 300 fs pulse duration are generated in a photoelectron gun after back-illumination of a photocathode with ultrashort UltraViolet (UV) laser pulses (λ = 266 nm). The electron beam has a transverse spot size of $\sim$ 100 µm and is focused on the sample in a grazing

incidence geometry (0.5-2.5°). The sample is mounted on a 5-axis goniometer, allowing for simultaneous adjustment of the incidence (θ) and the azimuthal (ϕ) angles. The electron beam diffracted from the surface is recorded on a phosphorus-screen/Micro Channel Plate (MCP)/CCD assembly. The dynamics is initiated by 45-fs laser pulses at 800 nm (repetition rate of 20 kHz) focused in normal incidence on the sample surface. The velocity mismatch and the non-coaxial geometry between electrons and photons are generally responsible for a broadening of the temporal resolution. This effect is compensated for by tilting the wavefront of the optical pulse with respect to its propagation direction as explained in chapter 3 [113]. Experiments heve been performed with a pump spot dimension of 3.5 × 0.4 mm and a pumping fluence of 6.5 mJ/cm^2. The chosen low excitation fluence is meant to prevent any surface charge dynamics to influence our results [25, 154–156].

The diffracted electrons are then recorded in stroboscopic mode at different delay times between the excitation laser and the electron pulse up to 50 ps after the excitation (tilted beam experiment) and 450 ps (untilted reference experiment). For every time point, we averaged 30 acquisition of 10^5 shots, containing 10^5 electrons each. To enhance the sensitivity of the experiment, a finger beam block is implemented to stop the direct beam electrons reflected by the sample surface.

4.4 RESULTS AND DISCUSSION

The static diffraction pattern of HOPG obtained in RHEED geometry is shown in figure 4.3, where the Bragg peaks corresponding to the (006) and (008) plane families are distinctly identified. The obtained lattice parameter c = 6.71 Å is in agreement with previous crystallographic characterisation of graphite [143, 144].

In the time-resolved experiments, a non-magnetic stainless-steel shield with a central hole, free to move on the plane orthogonal to the electron direction, positioned in front of the CCD. This prevents the pump beam scattered light from reaching the detector, thus reducing the background noise level. However, the only drawback of this implemented noise reduction technique is that the peripheral areas of the diffracted electrons is also screened and thus only a portion of the diffraction pattern can be imaged on the CCD. The experiments were performed by centring the visible diffraction pattern around the target diffraction peak - the (006). In figure 4.3, we show the selected diffraction peak as obtained before t_0 in the time-resolved experiment. The peak profile obtained as the average of the pixels intensity value along the drawn direction (green dashed line) is also shown in Fig. 4.3.

After optimising the spatial overlap of the electron beam and laser spot at the sample surface, we monitored the intensity variation of
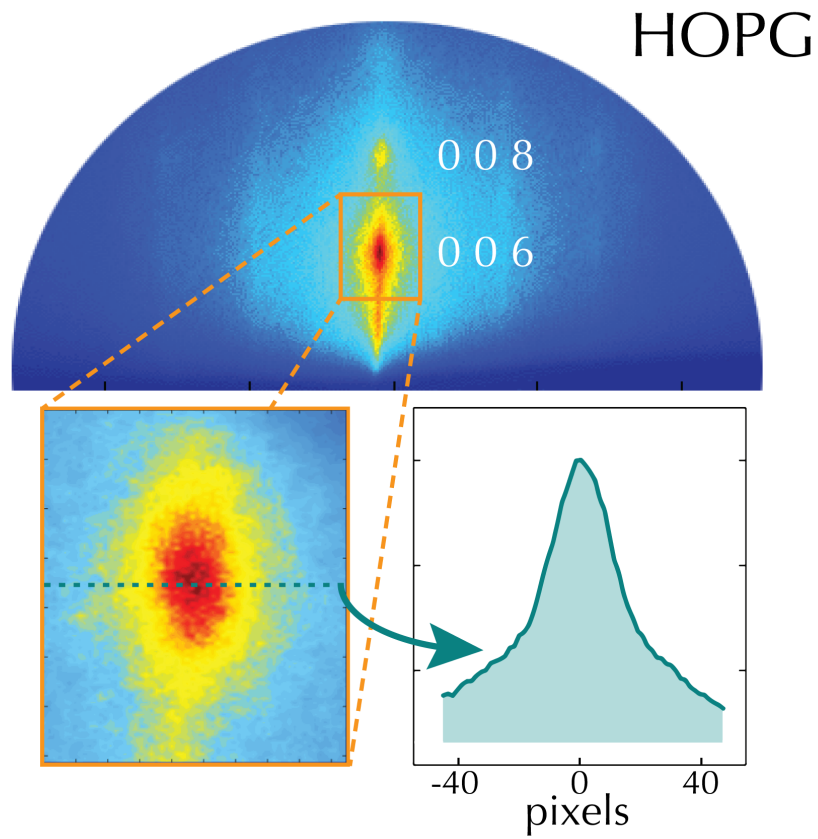
Figure 4.3: Diffraction pattern of the HOPG obtained in static conditions. The 006 and 008 peaks are identified. During time-resolved measurements, only a portion of the diffraction pattern centred on the 006 peak is recorded. The analysed peak is highlighted in the orange frame. The intensity of the peak is obtained as the average of the pixel intensity values along the drawn direction (green dashed line).
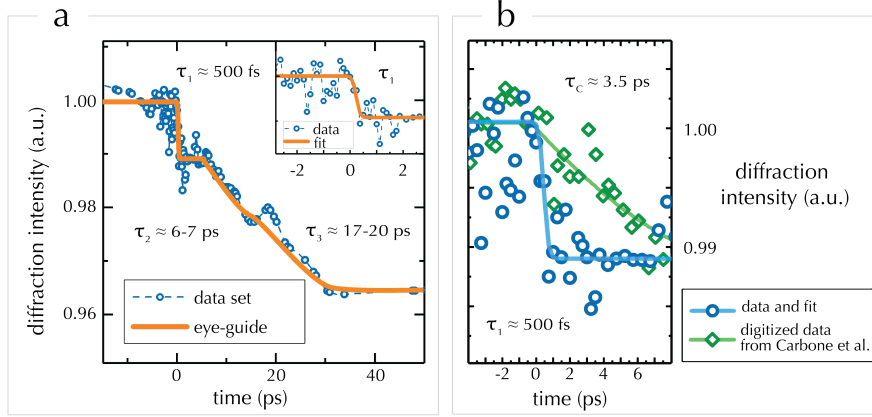
Figure 4.4: Intensity decay of the 006 Bragg peak. (a) Temporal evolution of the peak decay in the range -15 to 50 ps as respect to photoexcitation. Data are reported as empty circles, while in orange we report an eye-guide. The data evidence a composite decay, which can not be directly fitted with a multi-exponential curve. However, we estimated three different timescales involved in the process. In top-right inset, only the early decay is reported, and an error function decay is implemented to fit the data. The associated timescale corresponds to the $\tau_1 \sim 500$ fs reported also in the main graph. (b) Comparison of the measured fast decay with time constant τ_1 with the already published data by Carbone *et al.* [25]. The enhancement of the time resolution and a step-like behaviour during the intensity quench of the 006 peak are visible.

the (006) Bragg peak as a function of the delay time between pump and probe at the sample. The results are plotted in Fig. 4.4a. In the main figure, we report the data (blue dots and dashed lines) while in orange an eye-guide is superimposed. A composite intensity behaviour is observed: a first decay with $\tau_1 \approx 500$ fs succeeded by a ~ 5 ps long plateau, which then continues its quench on a ~ 20 ps timescale. In the figure, we indicate also the time constants $\tau_2 \approx 5$-7 ps and $\tau_3 \approx 17$-20 ps despite the impossibility to properly fit the curve with a multiexponential fit.

Conversely, the fist time constant $\tau_1 \approx 500$ fs is obtained by the fit of the data through an error function. The top-righ inset in Fig. 4.4a contains the detail of the fast decay with the fast time constant, where the orange line corresponds to the fit. In figure 4.4b, we compare our data (blue) with the data presented in [25], where a hint of the fast dynamics and the succeeding plateau was observed, but its complete resolution was hinder by the lower time resolution of the experimental setup, ~ 700 ps.

To enhance the signal to noise ratio and to better resolve the initial decay, a second investigation confined in the interval [-2 to 5 ps] and with higher statistics was performed. The results are reported in figure 4.5 as blue open circles, while the orange solid line corresponds to the best least-square error function fit of the data. The observed intensity decay evolves with the expected time constant $\tau_1 \approx 500$ fs, and the presence of a stem in the overall intensity decay is well evidenced.

The observed dynamics can be assigned to multiple phenomena occurring in the sample after photoexcitation. The most agreed model is
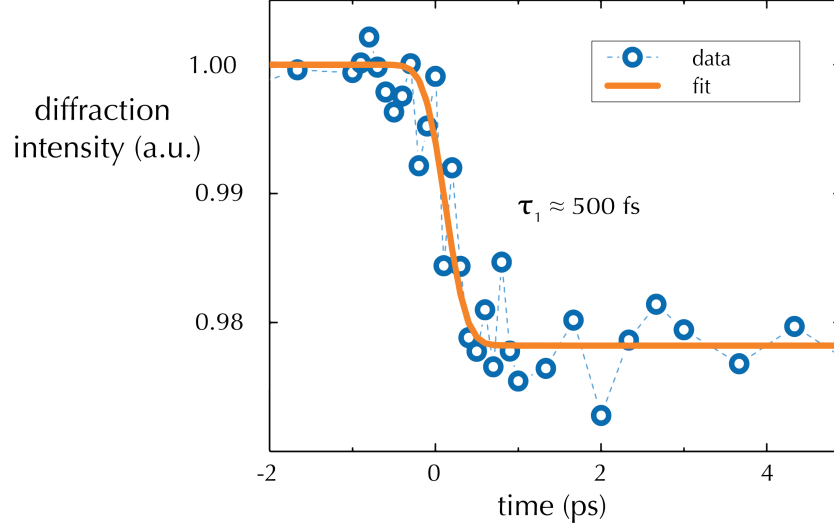
Figure 4.5: Fast component in the intensity decay of the 006 Bragg peak, data (blue open circles) and fit (orange line). The observed dynamics corresponds to energy transfer from excited electrons to strongly coupled-optical-phonons with a time constant $\tau_1 \approx 500$ fs.

that incoming photons excite anisotropically the electronic bands, as explained in [146, 150]. Subsequently, energy dissipation happens in first place by electron-phonon coupling with the mentioned SCOPs, whose excitation occurs within the observed time scale of 500 fs. Despite the directionality of SCOPs phonon modes is perpendicular to the c axis in graphite, their temporal evolution can be revealed by the observation of the (006) Bragg reflection because the impulsive population of SCOPs is known to trigger strong c-axis dynamics [25, 110, 157–161]. Afterwards, the system relaxes by progressive multiphonon scattering in a ~5-7 ps time window. We attribute the longer time-scale to the dynamics of the photoexcited surface of the sample and to the heat dissipation to the bulk by acoustic waves. This latter dynamics of graphite, often observed also by probes of the electronic structure, during the strongly anisotropic out-of-equilibrium heat diffusion has been a subject of intense debate [149, 157–160, 162]. Our current results provide a further indication of its structural origin.

4.5 CONCLUSIONS

In conclusion, it is worth noting that although the light-induced population of SCOPs in graphite has already been observed in transmission geometry [24], we point out that this study provides the first direct measurement of the short time constant τ_1 with U-RHEED on a mm^2-size 3D sample surface, which is not nanostructured and therefore more ideally represents crystalline graphite than ultrathin flakes. The overall ultrafast structural dynamics, the ps response and longer time thermalization in graphite have already been investigated in de-

tail in the literature [24, 25, 110, 146, 148–151, 158–165] and thus was not the main aim of our experiments.

Moreover, the obtained direct observation of the short time constant associated to the population of the SCOPs gives a direct *in situ* validation of the optimal tilting scheme developed for our beamline and presented in chapter 3.

LIGHT-INDUCED CONTROL OF THE VERWEY TRANSITION IN MAGNETITE

This chapter is based on the article by F. Pennacchio *et al.*, *Light-induced control of the Verwey transition in magnetite*, in preparation. An extended introduction and data are added.

The author acknowledge Dr. Giovanni Maria Vanacore, Dr. Vittorio Sala and Andrea Muni for their precious help and contribution during the experimental sessions which allowed the data collection.

5.1 MAGNETITE - A STATE OF THE ART

5.1.1 *Historical introduction*

Magnetite (Fe_3O_4) is a mineral belonging to the family of the iron oxides. It is the earliest discovered magnetic material: both the Chinese and the Greeks in ancient times were aware of the attractive properties of lodestone, natural magnetite ores. The first observations of natural magnetism can be attributed to the Greek philosopher and mathematician Thales of Miletus and date the sixth century B.C., while Chinese literature between the third century B.C. and the sixth century contains many references to the attractive peculiarity of magnets. In the first decades of the first century A.D., we can find the description of the properties of lodestone in the literary work *Moralia - On Isis and Osiris* by the Greek essayist and biographer Plutarch [166]. Almost contemporarely, the Roman author and naturalist Pliny the Elder reports about magnetic effects in his *Naturalis Historiae*, dated 77-79 A.D., as follows:

> There are two mountains near the river Indus; the nature of one is to attract iron, of the other to repel it: hence, if there be nails in the shoes, the feet cannot be drawn off the one, or set down on the other [167].

Magnetite nomenclature comes from the ancient greek world, too, despite a contentious concerning its proper etymology: some assert it comes from the name of the city Magnesia ad Sipylum, situated in the ancient region of Lydia, which nowadays is called Manisa and it is located in the Aegean region of Turkey [168]. Conversely, others state that the origin of magnetite name come from the mount Magnetos, a greek mountain particularly rich in this mineral [169]. On top of this, legend has it that it have been named after an ancient Greek

(a) *Octahedral crystals. Laach lake volcanic complex, Eifel, Rhine-Pfalz, Germany.*

(b) *Octahedral crystal, whose faces are repeated in a pyramidal structure. From Capranica, Vico Lake, Latium, Italy.*

(c) *Cubic crystals, showing regions of octahedral and rhombic-dodecahedral habitus, amid green lizardite. From Rio Varbore, Parma, Italy.*

(d) *Poli-habitus crystal, showing partially the dodecahedral faces, amid tabular brown crystals of phlogopite. From San Vito, Somma-Vesuvius Complex, Italy..*

Figure 5.1: Magnetite natural crystals, which can be structured in different habitus. Image courtesy of © Stephen Wolfsried (*a*) and © Gianfranco Ciccolini (*b - d*). [142]

shepherd called Magnes. He is told to first observe the magnetic properties of the mineral after the nails of his shoe and the iron ferrule of his staff clung to the lodestone [170]. Despite the controversy, it is worth noting than both the reliable etymologies concern geographical toponyms related to the presence of magnetite deposit, and even more interesting, is the term *magnetism* which has been named after the mineral, and not vice versa, as already confirmed by the Roman author Lucretius in his *De Rerum Natura* [171, 172].

We have to wait about a millenary for the first reported treatise dedicated to magnetism and magnets, *De Magnete*, written by the French scholar Pierre Pelerin de Maricourt in 1269 [173]. In the treatise he analyses the properties of freely pivoting compass needles, which found their application in medieval navigation shortly afterwards. Another milestone concerning the understanding of magnetism was set by William Gilbert in 1601 with his oeuvre *De magnete*, in which he first proposed geomagnetism and observed the loss of magnetic properties in heated lodestones [174].

However, despite the early observation and macroscopical understanding of magnetic phenomena, only the advent of quantum mechanics in the 20th century and modern scientific techniques allowed the probe and control of magnetic phenomena and the understanding of their interplay with structural and electronic degrees of freedom. Magnetite, probably the mostly studied magnetic material, played and still plays a fundamental role in this pathway along the understanding of magnetism.

5.1.2 *Mineralogy & biological presence*

Magnetite (Fe_3O_4) belongs to the family of iron oxides and is the natural ore with the highest iron content (72.3% in weight). It occurs in various geological environments ranging from metamorphic to igneous to sedimentary rocks. Magnetite crystals can be find in nature more commonly in the octahedral habitus exposing the {111} planes, less frequently they can assume the dodecahedral or rhombic-dodecahedral habitus. More exceptionally, they can present in the cubic shape [142, 175] (see Fig. 5.1).

Magnetite plays also a big role in biological systems. Biogenic magnetite nanocrystals have been found in many different species of living systems ranging from magnetotactic bacteria [176, 177] and protists [178], honeybees [179], fishes [180, 181], migratory birds [182] and cetaceous [183]. In these organisms, magnetite plays an essential role in the biophysical mechanism of magnetoreception (*i.e.* magnetic field detection) [184], which enhances orientation and navigation capabilities of the involved species [185]. In addition, many human tissues contains traces of magnetite nanocrystals with different concentration, with the highest gradient in the cranial area and in brain tissue [186]. Hypothesis of their function range from intracellu-

lar functional biomechanisms [187] to their possible role as biological memory molecules [188, 189].

5.1.3 *A material of actual interest*

Together with its early discovery, it came as well the first application of magnetite. The invention of the compass by the Chinese is an event of immense impact in ancient navigation. The earliest use of magnetite for navigation purposes is reported by at least the first century A.D., probably a couple of centuries before [190]. First compasses were made by a lodestone spoon on a flat bronze plate. As soon as the plate was moved, the spoon spun around to align with the Earth magnetic field and stopped with the handle pointing to the south. Friction drag resulting to the contact between the board and the spoon was later removed by the development of the floating compass. This compass format was introduced in Europe during the twelfth century A.D., probably brought by the sea by the arabs [191], and was improved along the centuries to grant high precision in navigation technologies.

In addition to its millenary history in navigation technology, nowadays magnetite applications range many more different fields. Maybe the broader diffusion of magnetite concerns data storage applications [192–195], where the induction of magnetization patterns in a magnetizable support allows to store data as non-volatile memory. A read/write head can access the stored information.

The technological breakthrough delivered by nanotechnology opened new fascinating possibilities also for magnetite in fields ranging from medicine to mechanical engineering, electronics and bio-imaging. Magnetite nanoparticles have been successfully tested as tumor-specific contrast agent in Magnetic Resonance Imaging (MRI) and Magnetic Resonance Tomography (MRT) [196–202] and they are promising candidates for successful cancer detection [203] and treatment by means of tissue targeting and magnetic hyperthermal therapies [199, 201, 204–206]. Due to its biocompatibiliy and the possibility of external magnetic driving, magnetite nanoparticles have been applied to drug delivery techniques [202, 207] and transdermal drug diffusion via magnetophoresis [208]. Additional uses in medicine involve magnetocitolysis and Alzheimer disease treatment [209].

In environmental engineering magnetite have been proved effective in the treatment of aqueous wastes [210, 211], contaminated soil analysis [212] and microorganisms and cells separation [213].

Furthermore, magnetite nanoparticles, in presence of a surfactant to prevent their aggregation and suspended in a carrier fluid, form the so-called ferrofluid colloidal solution. Due to its high magnetizability, when a magnetic field is applied ferrofluids tend to modify its shape to align with the magnetic field lines and move accordingly.

(a) *A lodestone spoon, the first exemplar of compass. A magnetite crystal was carved into a spoon and placed on a bronze plate. As the plate was moved, the spoon spun around to align with the Earth magnetic field and stopped with the handle pointing to the south.*

(b) *A magnetic hard disk. Magnetic data storage involves the induction of different magnetization patterns in a magnetizable material to store data as a nonvolatile memory. Information is later accessible using a read/write head.*
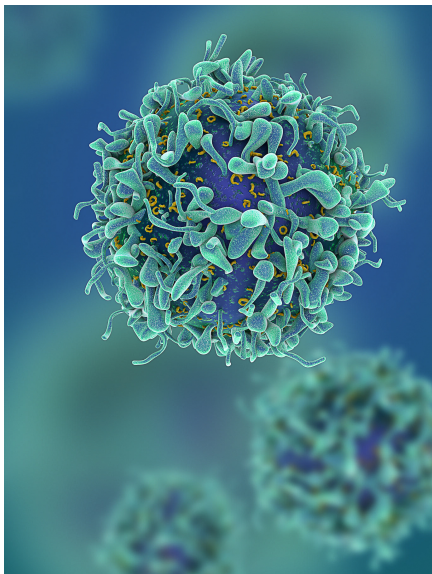
(c) *Qualitative rendering of a drug delivery system. A core nanoparticle is functionalized with different kind of ligands, which are responsible of both the targeting of the involved tissue and the subsequential drug release.*
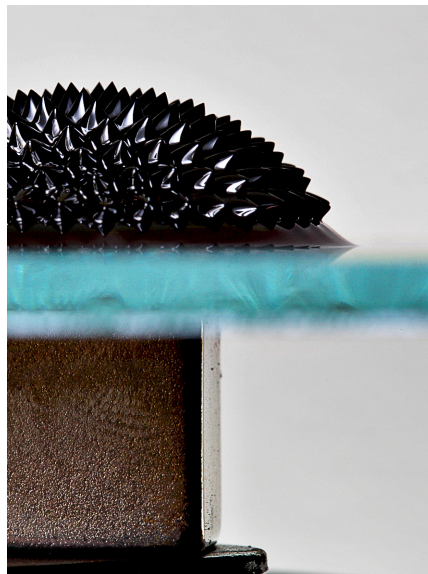
(d) *Magnetite nanoparticles in the presence of a surfactant suspended in a carrier fluid form a ferrofluid colloidal solution. In presence of a magnetic field, the magnetite nanoparticles aligns with the magnetic field lines.*

Figure 5.2: Ancient and modern applications of magnetite. Image courtesy of © Hong Kong Space Museum (a), © Wladimir Bulgar (b), © Nano Magazine (c) and © Gregory F. Maxwell (d).

This peculiar behaviour have been applied to design heat dissipators in loudspeakers or hard disks [214] or sealing agents for vacuum technology [214, 215].

A more exhaustive review of magnetite applications can be found in [216], while a deeper focus about ferrofluids and their application is contained in [217, 218].

5.2   STRUCTURAL INFORMATION

Magnetite (Fe_3O_4) is formally the combination of ferrous oxide (FeO) with ferric oxide (Fe_2O_3), ad it can be better described with the general formula ($Fe^{II}Fe_2^{III}O_4$). By early x-rays diffraction studies [219, 220] at room temperature and atmospheric pressure, magnetite is known to show the crystal structure of a cubic inverse spinel (Fd3̄m space group) where Fe cations are embedded in a face-centered cubic lattice of O^{2-} anions and they are either tetrahedrally (Fe_A) or octahedrally (Fe_B) coordinated. Fe atoms in Fe_A sites are always trivalent, showing an electronic configuration $3d^5$ with spin $S = 5/2$, while Fe_B sites host equally Fe^{II} ($3d^6$, $S = 2$) and Fe^{III} ($3d^5$, $S = 5/2$) atoms. The presence of different valence cations in equivalent crystalline sites results in mixed charge states for the Fe_B, which are characterised by an average effective charge of 2.5+. This electronic delocalisation is responsible for the high observed conductivity as respect to other spinels like Mn_3O_4 and Co_3O_4 [221]. The conventional unit cell is composed by eight formula units and its lattice parameter is **a** = 8.3941 Å [222] (see Fig. 5.3).

The magnetic structure of magnetite was first proposed by Louis M Néel [223] in 1948 and later confirmed by neutron diffraction [224]. Antiferromagnetically-coupling magnetic moments - orientated along the [111] direction - chatacterize the tetrahedral (Fe_A) and octahedral (Fe_B) iron cations. This can be rationalised in terms of superexchange [225] between A-O-B sites, and due to the different number of A and B sites, it result in a ferrimagnetic global behaviour.

5.3   THE VERWEY TRANSITION - A REVIEW

5.3.1   *First observations and the Verwey model*

Two temperature-dependent phase transition can be observed in magnetite: a ferrimagnetic-to-paramagnetic transition at the Curie temperature $T_C = 848$ K and a simultaneous structural, magnetic and electronic first-order transition at $T_V \simeq 125$ K (the so-called Verwey transition [226, 227]). The aforementioned transition temperature refers to high purity magnetite crystals, while observed deviations of T_V from
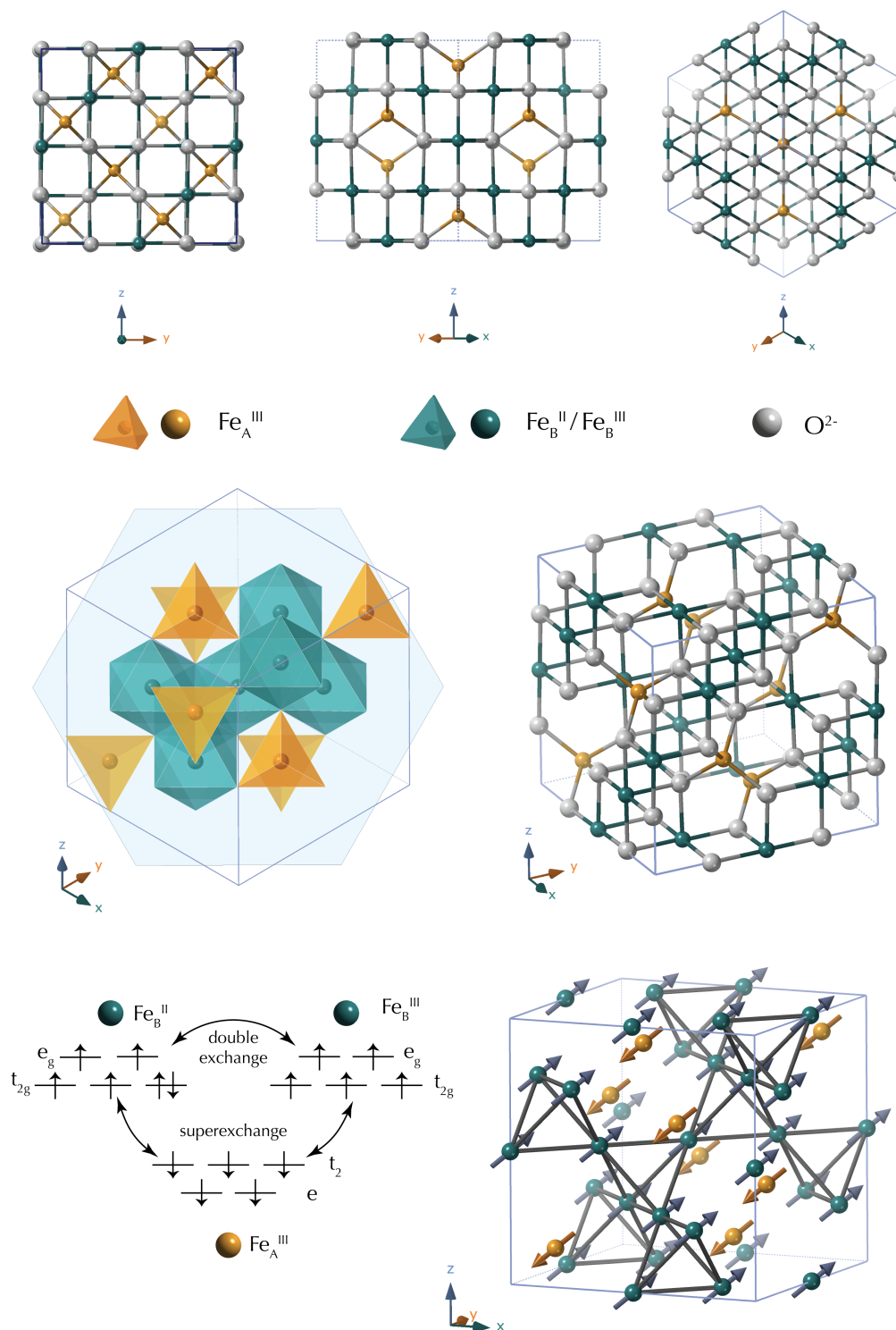
Figure 5.3: Magnetite atomic structure. Top: crystalline unit cell projected along the [100], [110] and [111] directions. Middle, left-hand side: polyhedral visualisation of the unit cell to highlight the different coordination sites typical of the spinel. In orange, tetrahedrally coordinate A-sites, while in green octahedrally coordinated B-sites are shown. The light blue hexagon represents the plane [$\bar{1}1\bar{1}$] as a landmark for observation. Middle, right-hand side: balls and stick model of the unit cell. The oxygen ionic radii are reduced for clarity reasons. Bottom: ferrimagnetic order in magnetite. Left, electronic exchange phenomena involved; right: render of the magnetic arrangement in the unit cell, superimposed to the pyrochlore lattice composed by the Fe$_B$ atoms.
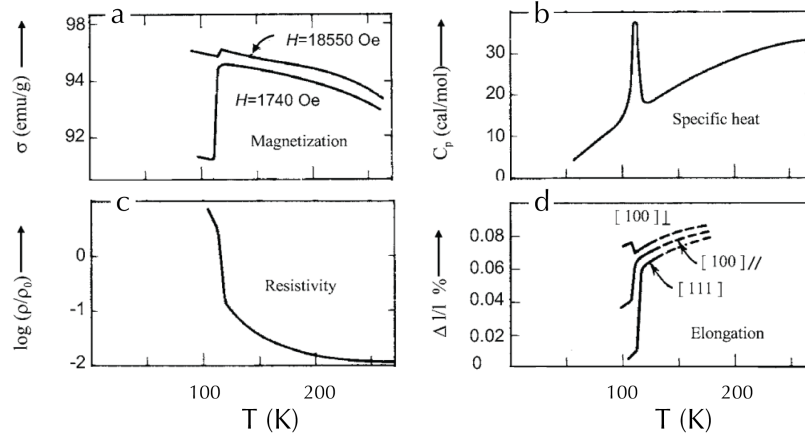
Figure 5.4: Basic manifestations of the Vervey transition in Fe_3O_4 near T_V, arranged in the historical order of their detection: (a) spontaneous jump of the magnetization [229], (b) specific heat anomaly [230], (c) spontaneous drop of the specific resistivity [231], (d) thermal expansion along selected directions [232]. Image and caption readapted from [228].

that value in most of the real crystals are related to a lower degree of purity [228].

The first evidence of this latter phase transition was reported in 1913 by Renger [233] during his PhD studies. In his thesis, he reported a discontinuity in the magnetic susceptibility in Fe_3O_4 as a function of the temperature. A dozen year later, Parks and Kelley documented a discontinuity in the sample heat capacity around 120 K [234]. Further observation of a phase transition fingerprint have been a spontaneous jump of the magnetization [229], specific heat anomaly [230], drop of the specific resistivity [226, 231] and thermal expansion along selected directions [232] (see Fig. 5.4).

Following his observations of the change in resistivity in magnetite [226], Evert Johannes Willem Verwey proposed a phase transition model driven by the charge ordering of the system in the Low Temperature (LT) phase [227]. According to his prediction, the average virtual state of $Fe_B^{2.5+}$ would disproportionate in distinct Fe_B^{II} and Fe_B^{III} in an orthorhombic unit cell.

5.3.2 *The low temperature unit cell*

In the seventy years that followed, both the charge ordering nature of the structural transition and the LT crystalline structure have been the ground of a profuse scientific debate [235–241]. Despite the controversies, in the last twenty years the scientific community seems to converge toward a LT crystalline phase belonging to the monoclinic Cc space group. The experimental milestones that concurred to this detemination are the neutron diffraction study performed by Iizumi *et al.* in 1982 [242], the combined X-ray and neutron powder diffrac-

tion study carried out by Wright *et al.* [243, 244], and the recent X-ray experiment performed by Senn *et al.* [245].

Accordingly, the Verwey structural transition consists in a reversible crystallographic distortion with symmetry lowering from the cubic $F\bar{d}3m$ to the monoclinic Cc space group. During the transition, the top and bottom faces of the cube mutually glides along the $[110]_c$ direction, resulting in a deviation of the $\mathbf{c}_m$-axis from $[001]_c$ axis by an angle of $\sim 0.2°$ (*c* and *m* subscripts designate the cubic and monoclinic phases, respectively). Also the $\mathbf{a}_m$- and $\mathbf{b}_m$-axes lie along the $[110]_c$ and $[1\bar{1}0]_c$ axes respectively. If we neglect the tilting of the vertical axis, the global transformation between the primitive vectors consist in the length doubling in the out-of-plane direction and in an increase by a factor $\sqrt{2}$ and a rotation by $-\pi/4$ in the plane directions, which can be described as follows:

$$(\mathbf{a}_m, \mathbf{b}_m, \mathbf{c}_m) = (\mathbf{a}_c, \mathbf{b}_c, \mathbf{c}_c) \times \left[\sqrt{2} \begin{pmatrix} 1/\sqrt{2} & 1/\sqrt{2} & 0 \\ -1/\sqrt{2} & 1/\sqrt{2} & 0 \\ 0 & 0 & 0 \end{pmatrix} + \begin{pmatrix} 0 & 0 & 0 \\ 0 & 0 & 0 \\ 0 & 0 & 2 \end{pmatrix} \right]$$

and summarised by the formation of a $\sqrt{2}a \times \sqrt{2}a \times 2a$ supracell. As a result, the low-temperature unit cell volume is four times the one of its high-temperature parent cell.

Nevertheless, while the controversy upon the LT phase space group seems to be solved, the nature of the structural transition is still questioned and brought to the formulation of various and contradictory models involving charge-ordered, orbital-ordered and bond-dimerised ground-states [246–248].

However, recent studies by Senn *et al.* argue that all the structural distortion characterising the LT phase cannot be described by the condensation of a single subset of phonon modes, since a more cooperative contribution of the 168 frozen modes, in particular with Δ_5, X_1, X_4, and W_1 symmetries - is required [245, 250]. As a consequence, the phase transition would be rather driven by local distortion induced by orbital ordering. Accordingly, they identify linear three-Fe-sites quasiparticles - mostly composed by two outer Fe^{III} and a central Fe^{II} on B sites - characterised by the delocalisation of the Fe_B^{II} electron over the neighbouring Fe_B^{III} and by a subsequent dislocation of the two terminal Fe^{III} atoms toward the central Fe^{II} one. These three-Fe quasi-particles have been named *trimerons* and organise in a long-range network defined by 60° or 120° connections. The intersections of the trimerons happen in most cases on the terminal Fe_B^{III} sites (see Fig. 5.5d).

In accordance with this model, they identify these distortions as the primary building blocks of the LT phase and the Verwey transition would mark the conversion of the frozen network of trimerons
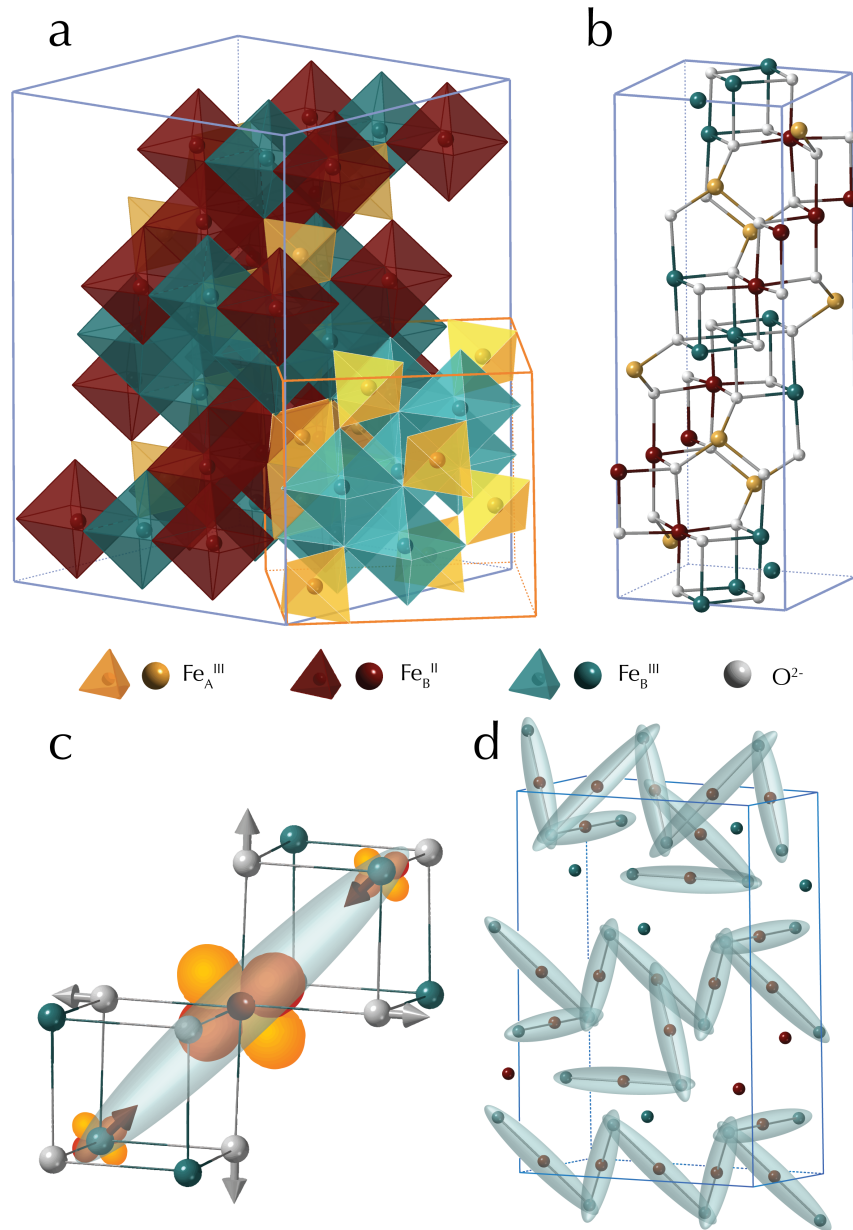
Figure 5.5: Monoclinic structure of magnetite. (a) Direct comparison of the cubic (orange edges) and monoclinic (indigo edges) unit cell in magnetite, obtained via Crystalmaker [249]. The polyhedral visualisation model is reported, where each Fe atom is at the centre of the polyhedra and O atoms are situated at their vertices. (b) Representation of the P2/c unit cell used by Iizumi [242] and Wright [243] for the monoclinic phase structural refinement. It corresponds to a $a_m/2 \times b_m/2 \times c_m$ subcell of the Cc unit cell. (c) Qualitative visualisation of a trimeron. The charge delocalisation amongst the central Fe_B^{II} and the terminal Fe_B^{III} is correlated to a local lattice distortion. (d) Visualisation of the trimeron network in the unitary cell of monoclinic magnetite. Most of the trimeron-trimeron connections in the network happens at the terminal Fe_B^{III}, with only two exceptions, where the connection is located at the Fe_B^{II} position.
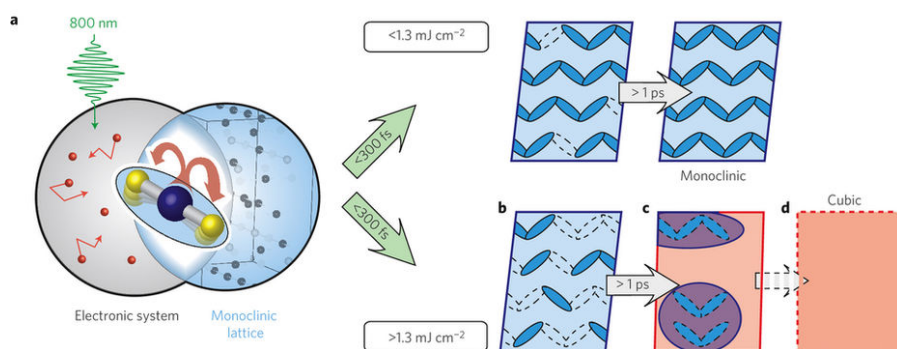
Figure 5.6: Summary of the photoinduced Verwey transition mechanisms. (a) Ultrafast trimeron annihilation due to laser excited $Fe^{II}-Fe^{III}$ charge transfer launches strongly coupled electronic and lattice dynamics. (b,c) For a pump fluence above a fluence threshold trimeron holes (b) transform with a time constant of 1.5 ± 0.2? ps to a state with shrinking patches of remnant phase-scrambled electronic order (c). Its structure is approaching that of the cubic case (d) embedded in a network supporting mobile charge fluctuations (red) derived from the aggregation of the trimeron vacancies in (b). (d) The end of the line would be the fully metallic, cubic phase. Image and caption from [251].

observable in the insulating state to a fluctuating structure of these quasi-particles.

5.3.3 *Time-resolved evidences*

In the wake of the recent structural refinement of the Cc monoclinic cell and of the proposition of the trimerons lattice, de Jong *et al.* [251] in a recent pump-probe x-ray experiment demonstrated that nonequilibrium transient metallic state can be triggered in LT magnetite *via* photoexcitation. A two-steps fluence-dependent mechanism was observed, composed by an initial trimeron annihilation followed either by a reconstruction of the trimerons network or by a lattice reorganization toward the conductive phase. Time-resolved optical reflectivity measurement unveiled an intermediate state of phase segregation of insulating domains in a percolative network of conducting phase as the main reason to the observed mechanism. A graphical summary can be found in figure 5.6.

This scenario have been confirmed by a further study [252], where the optical reflectivity of magnetite and the variation of the spectral weight of the features related to the Fe_B^{II} $t_{2g} \longrightarrow Fe_B^{III}$ t_{2g} and the Fe_B^{II} $t_{2g} \longrightarrow Fe_B^{III}$ e_g electron transitions have been investigated at the photoinduced Verwey transition limit. Also in this case, a fluence interval characterized by the cohexistence of insulating and metallic domains have been identified.

Recent optical results by Borroni *et al.* have revealed that fs bluelight pulses (3.1 eV) can transiently bring the conduction band carriers of magnetite in their low-temperature ordered state, while the crystal is above the critical temperature of the phase transition [253]. In this scenario, the ability to switch the transport properties by adopt-

ing a tunable external optical stimulus opens new possibilities for optoelectronic devices. In order to fully exploit this potential, it is therefore necessary to understand the interplay between the atomic motions and the electronic structure changes responsible for the phase transition. In this investigation frame we include the UED experiments that we present in the following sections.

Further details concerning the atomic-scale mechanisms subdued to the Verwey transition and the state of the art of its investigation can be found in [228] and in the solid PhD thesis of Mark S Senn [254] and Simone Borroni [255, 256].

5.3.4 *About micro-twinning*

As common in phase transformations involving a lowering in symmetry, magnetite Verwey transition results in the formation of micrometer-sized structural domains called twins, where each twin corresponds to a different orientational variant of the monoclinic phase with respect to the parent cubic lattice. This phenomenon is due to the equivalence of the main crystallographic direction in the parent unit cell, as the $\mathbf{c}_m$ axis can be established with equal probability along the $\langle 100 \rangle_c$, the $\langle 010 \rangle_c$ or the $\langle 001 \rangle_c$ directions during the phase transition. Additionally, due to the equivalence of the $\langle 110 \rangle_c$ directions, the top and bottom faces of the cubic cell can glide with equal probability along the four directions. Thus, considering also inversion, the presence of $3 \times 4 \times 2 = 24$ possible orientations can be observed in the crystal [257]. For clarity reasons, we report the main three possible twins orientation in figure 5.7.

Micro-twinning has longly affected the structural investigation of magnetite monoclinic phase, and the development of detwinning methods has been the key to address the structural characterisation of the LT phase [242]. To preserve a unique structural domain when crossing the Verwey transition from above, a specific twin must be favoured in energy. Field-cooling, *i.e.* the application of a magnetic field while crossing the Verwey temperature, have been demonstrated effective in the univocal selection of the $\mathbf{c}_m$ axis all along the crystal due to the coincidence of the $\mathbf{c}_m$ axis with the easy magnetisation axis in the LT phase. Furthermore, the application of uniaxial tension along a specific $[111]_c$ axis - or a cylindrical compression on a plane perpendicular to the same axis - favours the twin whose elongation is oriented on the same direction. To successfully apply the detwinning procedure, a single crystal with cylindrical shape and axis parallel to the $[111]_c$ direction surrounded by aluminum rings was designed. While field cooling across the Verwey transition, the thermal contraction mismatch between aluminum and magnetite results into the application of a cylindrical contact pressure along the desired axis.

A theoretical addressing of the aforementioned procedure can be found [258]. The detwinning process have been implemented in the
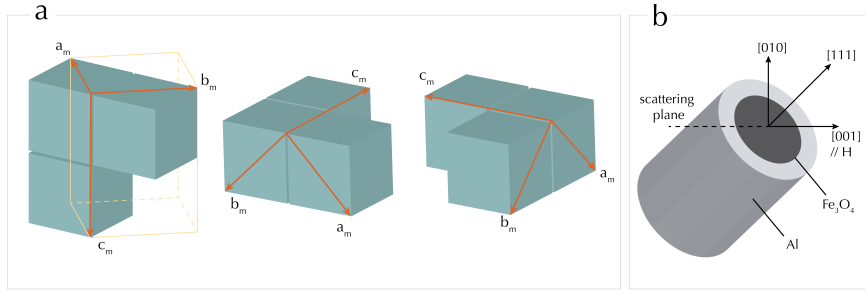
Figure 5.7: Twinning and detwinning in magnetite. (a) Crystallographic relationships between cubic and monoclinic phases in magnetite during the twinning process. The cubic unit cell is shown as a shaded green box, while the orange axes show the possible orientation of the c_m axis after the phase transition. Only 3 of the 24 possible orientations are shown. The other orientations can be obtained by progressive 90° rotations around the c_m axis (4 twins for each c_m direction) and by the inversion operation applied to every twin, that makes $3 \times 4 \times 2 = 24$ twins. (b) Schematic representation of the experimental geometry for detwinning magnetite samples through cylindrical compression and field cooling. Readapted from [255, 257].

neutron scattering experiments reported in [256]. However, it has not been possible to address it during Ultrafast Reflection High-Energy Electron Diffraction (URHEED) experiments due to the incompatibility of the procedure with our experimental setup.

5.4 UED EXPERIMENTS ON MAGNETITE

5.4.1 *Materials & Methods*

The URHEED experiments were performed on a bulk $5 \times 5 \times 2$ mm^3 natural magnetite single crystal (99.99% pure), purchased from Surface Preparation Laboratory [259]. Resistivity measurement proved the Verwey transition to happen at $\sim$ 117.5 K. The sample was cut to expose the (1$\bar{1}$0) surface. In the following experiments we started our investigation from the (4$\bar{4}$0) Bragg reflection in the cubic phase of magnetite.

The diffraction experiments have been conducted using the ultrafast electron diffraction setup at LUMES at EPFL working in reflection geometry. Ultrashort electron pulses with energy per particle of 30 keV and 300 fs pulse duration are generated in a photoelectron gun after back-illumination of a photocathode with ultrashort UV laser pulses (λ = 266 nm). The electron beam has a transverse spot size of $\sim$ 100 µm and is focused on the sample in a grazing incidence geometry (0.5-2.5°). The sample is mounted on a 5-axes goniometer, allowing for the simultaneous adjustment of the incidence (θ) and the azimuthal (ϕ) angles. The temperature of the sample can be varied in the range 1.8 K to 300 K employing a liquid helium flow cryostat. The electron beam diffracted from the surface is recorded on a phosphorus-screen/MCP/CCD assembly. The dynamics is initiated by

45-fs laser pulses at 800 nm (repetition rate of 20 kHz) with fluences ranging from 0.2 to 4.5 mJ/cm^2 focused in normal incidence on the sample surface. The velocity mismatch and the non-coaxial geometry between electrons and photons are generally responsible for a broadening of the temporal resolution. This effect is compensated for by tilting the wavefront of the optical pulse with respect to its propagation direction as explained in chapter 3 [113]. Therefore, the time resolution of the experiments is < 500 fs. The diffracted electrons are then recorded in stroboscopic mode at different delay times between the excitation laser and the electron pulses up to 250 ps after the excitation.

Here, we have explored the lattice dynamics of the magnetite crystal for a laser excitation of 800 nm at two different initial temperatures, 40 K and 300 K, the first below and second above the Vervey transition temperature, $T_V \sim 117.5$ K in our sample.

5.5   RESULTS

In kinematical diffraction theory the diffraction intensity I and the scattering vector s depend on the modulus and on the phase, respectively, of the structure factor F. Because F is strongly dependent on the atomic displacement, u, the temporal behaviour of the observed diffraction pattern is able to mirror the evolution of the lattice dynamics within the magnetite crystal during thermal expansion phenomena or across the Verwey transition. In Bragg scattering the incoming electron wave is directly coupled to an outgoing wave and, for a weak inner potential, the scattering condition is given by:

$$2d^{[hkl]} \sin \theta = n\lambda_e \tag{5.1}$$

where $\lambda_e = 6.98 \times 10^{-12}$ m is the de Broglie wavelength associated to 30 keV electrons and $d^{[hkl]}$ is the interplane separation along the $[hkl]$ direction. A homogeneous deformation (expansion/contraction) of the lattice will thus modify the scattering vector s of the Bragg peak according to the relation:

$$\frac{s(t) - s_0}{s_0} \approx \frac{d^{[hkl]}(t) - d_0^{[hkl]}}{d_0^{[hkl]}} = \epsilon^{[hkl]} \tag{5.2}$$

where the subscript o indicates the corresponding quantities before laser excitation, and $\epsilon^{[hkl]}$ denotes the lattice strain along the $[hkl]$ direction.
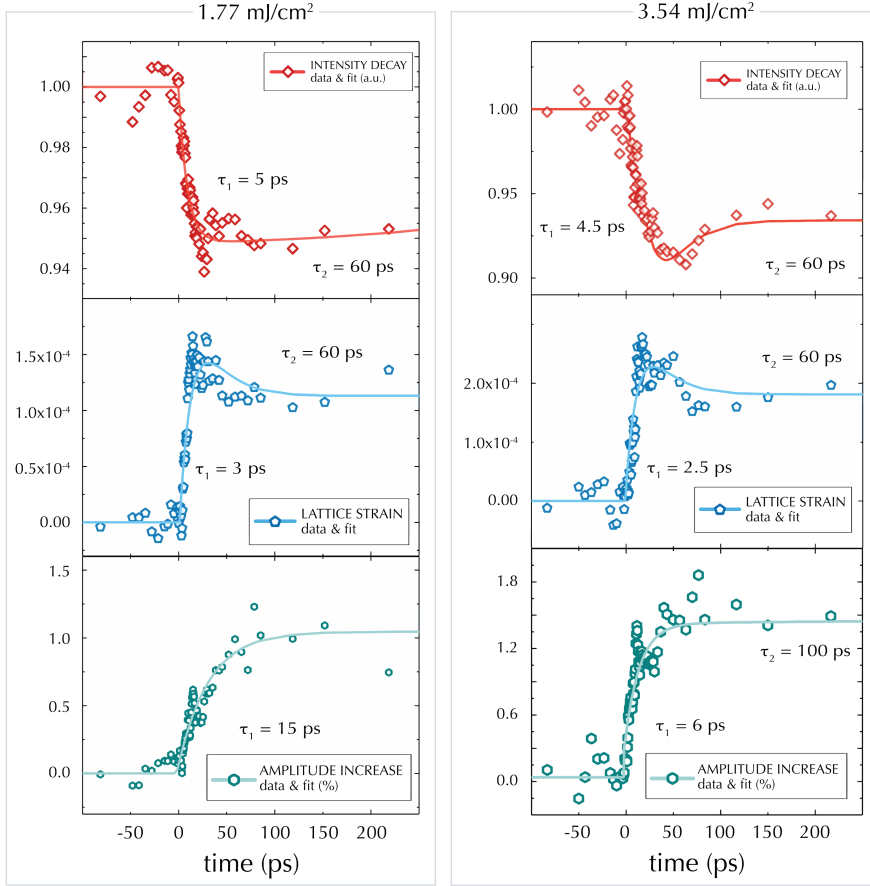
Figure 5.8: Time-dependent evolution of the intensity (red diamonds), strain (blue pentagons) and width (green hexagons) of the [4$\bar{4}$0] diffraction peak at T = 300 K and with a pump fluence of 1.77 and 3.54 mJ/cm^2. In both cases, we can observe a fast quench in the intensity, due to an expansion of the lattice spacing on the observed reflection and to a broadening of the peak. A sketch with the definition of intensity, strain and amplitude of the peak can be found in figure 5.11. The acquired data were fitted by means of mono- or biexponential curves.

5.5.1 *Photoinduced thermal expansion*

Our first investigation of the dynamics in magnetite was performed at a temperature of $\sim$ 300 K and with a pump wavelength λ = 800 nm. In figure 5.8 we report the observed time-dependent evolution of the features of the [4$\bar{4}$0] diffraction peak - intensity, strain of the related family of planes and amplitude - upon photoexcitation, with pump fluences of 1.8 mJ/cm^2 (a) and 3.5 mJ/cm^2 (b). At the fluence value of 1.8 mJ/cm^2, we observe a $\sim$ 5% quench in the peak intensity, together with an observed expansion of $\sim 1.25 \times 10^{-4}$ and with an increase of the peak amplitude of $\sim$ 1%. At the fluence value of 3.5 mJ/cm^2, a $\sim$ 8-10% quench in the peak intensity, together with an observed strain of $\sim 2.00 \times 10^{-4}$ and with an increase of the peak amplitude of $\sim$ 1.5% is registered.

The same parameters have been investigated as a function of the pump fluence (see Fig. 5.9). A linear dependence of the peak intensity - red - and of the lattice strain $\epsilon^{4\bar{4}0}$ - blue - as respect to the
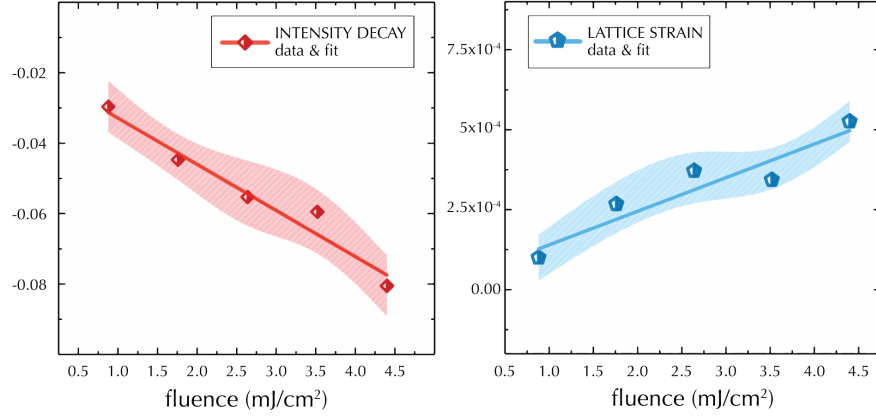
Figure 5.9: [4$\bar{4}$0] diffraction peak intensity decay (red) and lattice strain along the [1$\bar{1}$0] directon (blue) plotted as a function of the pump fluence. We observe a linear dependence between the intensity decrease and the crystal expansion as a function of the fluence. These observations agree with the photoinduced thermal expansion of the crystal. The coloured areas represent a b-spline of the calculated error interval.

pump fluence is retrieved. The aforementioned observations are in good agreement with the thermal expansion of the crystal cell, as discussed in section 5.6.1.

5.5.2 *Peaks attribution in the monocline phase*

We slowly cooled the sample with liquid helium to the LT phase, while monitoring the diffraction pattern. When the sample crosses the Verwey temperature, we observe a wide broadening and a position variation of the [4$\bar{4}$0] peak in the direction perpendicular to the sample surface.

Microscopically, during the phase transition two main structural processes occur: the rotation of -π/4 of the monoclinic cell as respect to the parent cell and the formation of microtwins domains. The effect of the rotation alone, in presence of an effective detwinning protocol, would still cause a change of the observed diffraction feature, due to the new orientation of the unitary cell as respect to the incoming radiation. The combined effects result in the superposition of various diffraction features of the LT phase with different spacing parameters d, thus explaining the broadening of the peak.

To assign the diffraction features appearing in the monocline cell, we reconstructed on CrystalMaker [249] both the crystalline phase of cubic and monoclinic magnetite. The cubic magnetite structure was obtained from Fleet [222], while the monoclinic unit cell was built as the $2a \times 2b \times c$ supracell of the P2/c unitary cell defined by Wright et al. [244] and used for the structural refinement of the Cc monoclinic unit cell. The P2/c cell is related to the parent cubic cell by the relation $a_c/\sqrt{2} \times a_c/\sqrt{2} \times 2a_c$. The monoclinic cell size, thus, corresponds to
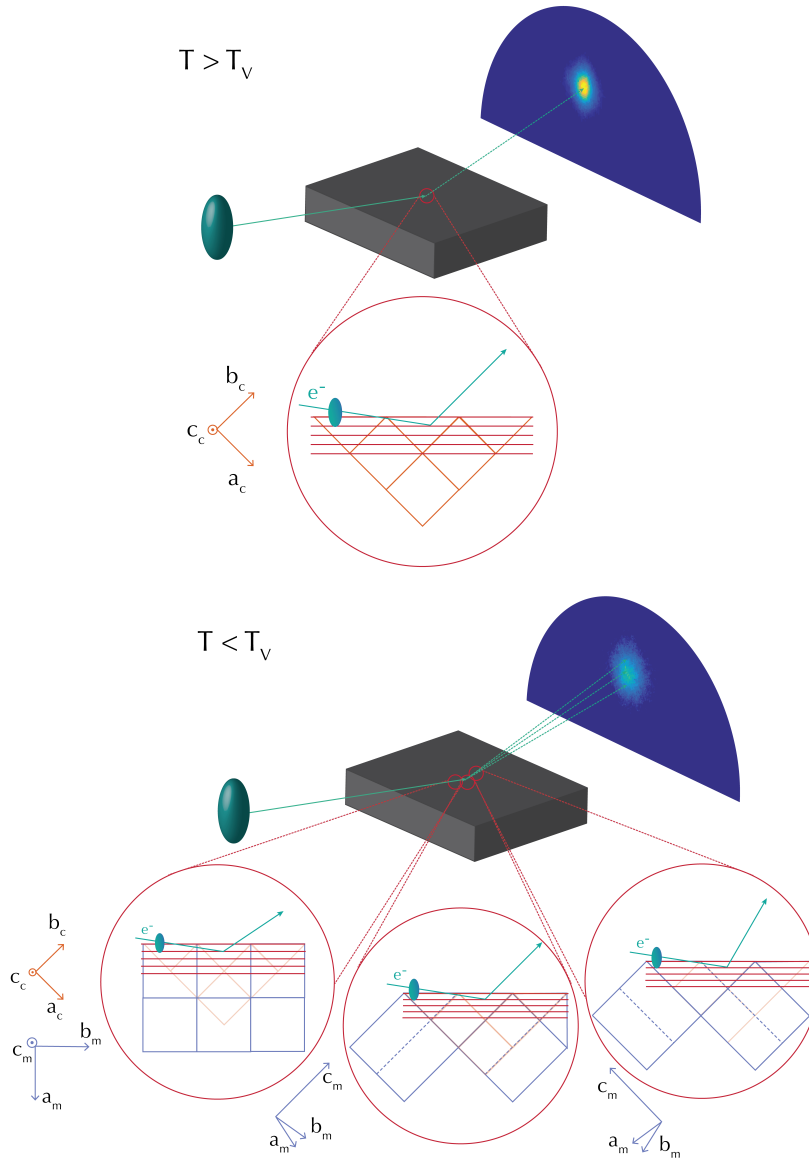
Figure 5.10: Change of the observed diffraction pattern across the Verwey transition. Top: sketch of the diffraction patter at $T > T_V$, with the definition of the cubic unit cell. The defined diffraction peak reflects the long range order in the crystal. Bottom: effects of the twinning over the diffraction pattern. The three main twins orientation are shown, with the $\mathbf{c}_m$ establishing over $\mathbf{c}_c$, $\mathbf{b}_c$ and $\mathbf{a}_c$, respectively. According to the variation of the spacing of the monoclinic families of planes correspondent to the $[4\bar{4}0]_c$, we assist to a distribution of the scattering angles. The direct consequence is a broadening of the diffraction feature in the low temperature phase. The presented sketch shows a simplified version of the problem, with a graphical approximation of the Cc monoclinic cell to an orthorhombic unit cell (the angle β is here neglected). Also, for clarity reasons, the diffraction peaks are magnified as respect as their dimension on the collected diffraction pattern.

the $\sqrt{2}a_c \times \sqrt{2}a_c \times 2a_c$ supracell of the parent cubic cell, as reported in section 5.3.

The two cells have been superimposed to reconstruct the variation of the observed reflection for the different possible twins. When the $\mathbf{c}_m$ axis establishes along the $\mathbf{c}_c$ axis, the previous $[4\bar{4}0]_c$ reflection corresponds to the $[800]_m$ and to the $[080]_m$. Among the 24 possible twins, in case of equiprobability in their orientation, 1/6 of the twins population exposes the $[800]_m$ and another 1/6 exposes the $[080]_m$ direction. Instead, if the $\mathbf{c}_m$ axis establishes along the $\mathbf{a}_c$ axis, the previous $[4\bar{4}0]_c$ reflection corresponds to the $[448]_m$ and to the three equivalents for successive rotations of $\pi/2$, the $[4\bar{4}8]_m$, $[\bar{4}48]_m$ and $[\bar{4}\bar{4}8]_m$. It is worth noting that single twins will show only one reflection, and that this superposition is caused by the possible orientations of the LT cell. Due to the equivalent spacing of these reflections, we will refer more in general to the $\{448\}_m$ family. Among the 24 possible twins, in case of equiprobability in their orientation, 1/3 of the twins population exposes the $\{448\}_m$ direction. Last, if the $\mathbf{c}_m$ axis establishes along the $\mathbf{b}_c$ axis, the previous $[4\bar{4}0]_c$ reflection also corresponds to the $\{448\}_m$ family. Thus, among the 24 possible twins, 2/3 of their population exposes the $\{448\}_m$ direction. A qualitative sketch, not taking into account the variation of the angle β is represented in figure 5.10.

Once identified the composite diffraction structure of our sample, the corresponding spacing d has been computed for the different reflections. The results are summarised as follows:

cubic	d [Å]	monoclinic	d [Å]	strain ϵ
		800_m	1.4861	-1.5 $\times 10^{-3}$
$4\bar{4}0_c$	1.4839	080_m	1.4812	1.8 $\times 10^{-3}$
		448_m	1.4810	2 $\times 10^{-3}$

The direction of the strain in the table (positive = expansion, negative = contraction) are related to the transition from the LT monocline phase to the cubic phase. The computation of the position in our CCD of the identified diffraction features confirms the broadening of the observed peak.

In what follows, the word *strain* is used also to indicate the variation of the spacing of different families of planes due to the rotation of the unit cell and to the microtwinning during the phase transition. Also, we will refer to the superposition of the $\{448\}_m$, $\{800\}_m$ and $\{080\}_m$ in the monoclinic phase as the *composite peak*.
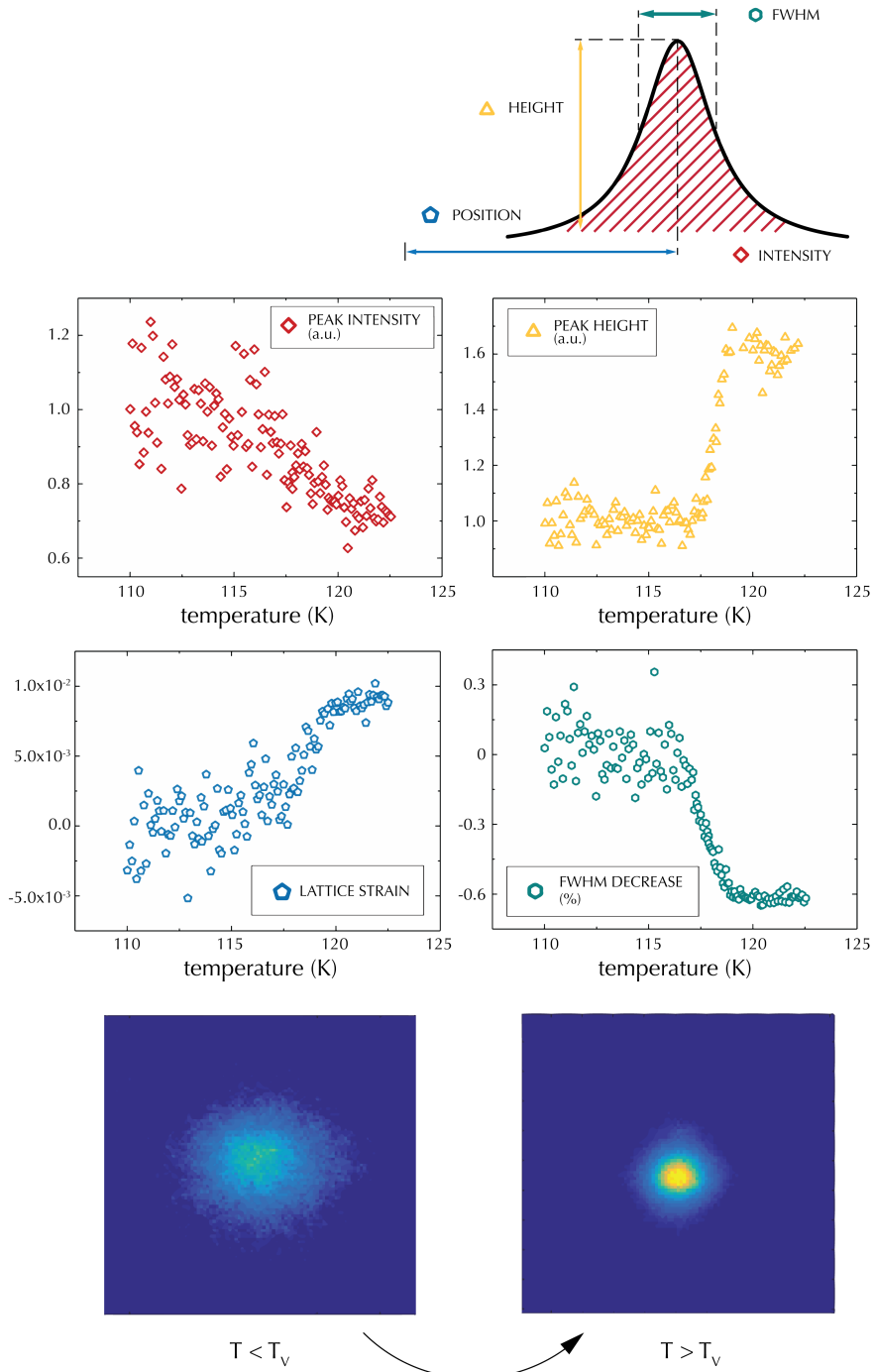
Figure 5.11: Variation of the observed diffraction features as a function of the temperature across the Verwey transition. Top: sketch of the diffraction peak with the definition of the analysed parameters: intensity (red diamonds), height (yellow triangles), position (blue pentagons) and amplitude (green hexagons) evaluated as FWHM. All the parameters are normalised as respect to the initial monoclinic phase. The lattice strain value is related to the peak position as expressed in equation 5.2. Bottom: signature of the thermal Verwey transition in the shape of the observed diffraction spot, before and after the Verwey temperature T_V. The two images are integrated the same amount of time.

5.5.3 *Thermal phase transition*

To reference the monocline-to-cubic phase transition in magnetite, we registered a sequence of diffraction pattern while crossing thermally the Verwey Temperature T_V, situated at ~ 117.5 K in our sample. The experiment was performed as follows: after cooling the sample at a temperature of ~ 110 K we removed the liquid helium flow from our cryostat and we let the sample thermalise. As the temperature rose, a sequential acquisition of diffraction patterns was performed until the temperature reached a value of ~ 122.5 K. During the investigated temperature interval, the thermalisation rate was ~ 0.5 K/min.

The modification of the observed diffraction feature during the transition from the monoclinic to the cubic structure was analysed. Figure 5.11 reproduces the change in the diffraction features during the thermal phase transition. The intensity (red), the height (yellow), the position (blue) and the amplitude (FWHM - green) of the Bragg feature in our diffraction pattern are plotted as a function of the temperature. The increase in the peak height and the strong decrease in the peak amplitude are due to the convergence of the multiple diffraction features of the monocline phase to the unique $[4\bar{4}0]_c$ Bragg peak in the cubic phase. The observed expansion in the cell is also due to the average higher spacing of the $4\bar{4}0_c$ planes as respect to the monoclinic reflections, as summarised in the table above.

In order to understand the decrease in the overall peak intensity, the squared structure factor $|F_{hkl}|^2$ have been computed for the involved reflections and unit cells ($4\bar{4}0_c$, 448_m, 800_m and 080_m), where the unit cell structure factor, F_{hkl} is defined as

$$F_{hkl} = \sum_1^n f_n e^{2\pi i(hx+ky+lz)} \tag{5.3}$$

where n is the number of atoms in the unit cell, f_n is the atomic scattering factor, h, k and l are the indexes of the considered reflections and x, y and z are the fractional coordinates of each atom in the unit cell.

The atomic scattering factors for Fe^{II}, Fe^{III} and O^{2-} were obtained from the international tables of crystallography [260], for scattering of electrons at the value $sin(\theta)/\lambda = 0.3368\text{Å}^{-1}$. This latter was computed with the Bragg law considering the spacing d of the lattice families of planes of interest. The scattering factor considered were the following: $f_{Fe^{II}} = 2.1665$, $f_{Fe^{III}} = 2.1827$, $f_{O^{2-}} = 0.9259$. Due to the charge delocalisation in Fe_B sites in the cubic phase, an intermediate value of the scattering factor between Fe^{II} and Fe^{III} have been considered in B sites. The atomic coordinates in the considered cells were obtained from Fleet [222] for the cubic cell and from Wright et al. [244] for the monoclinic cell.
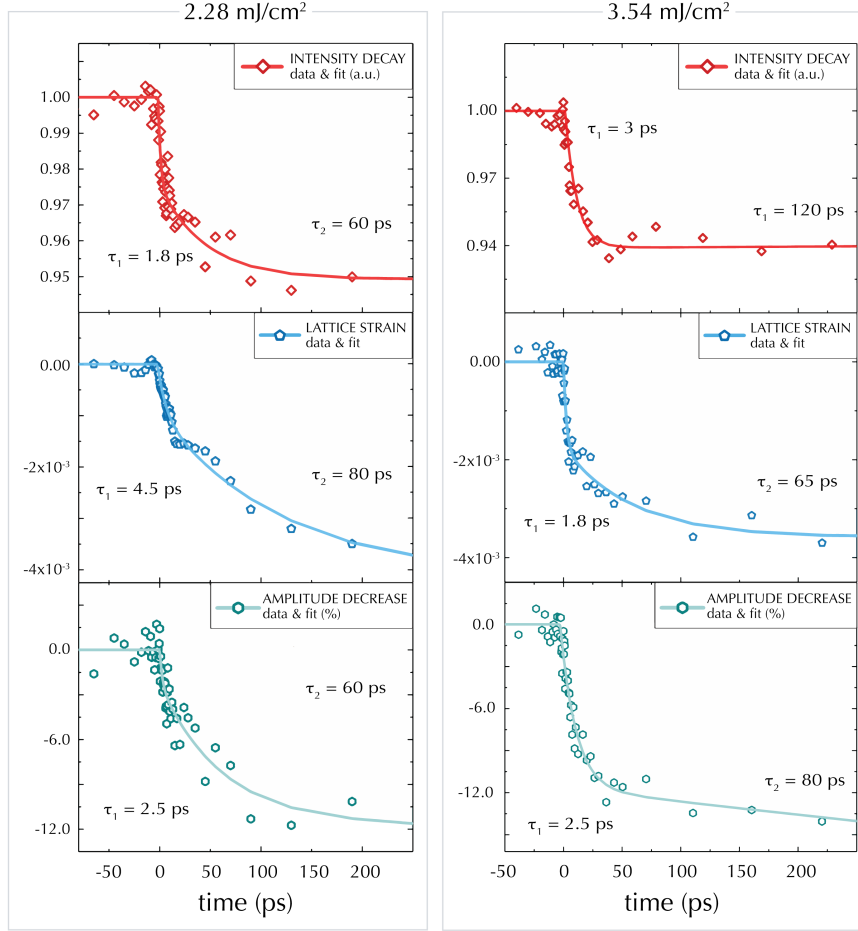
Figure 5.12: Time-dependent evolution of the intensity (red diamonds), strain (blue pentagons) and width (green hexagons) of the composite diffraction peak at the temperature T = 40 K and with a pump fluence of 2.28 and 3.5 mJ/cm². In both cases, we can observe a fast quench in the intensity, linked to a contraction of the lattice spacing of the observed reflection and to a narrowing of the peak. A sketch with the definition of intensity, strain and amplitude of the peak can be found in figure 5.11.

The obtained $|F_{hkl}|^2$ values for the three monoclinic reflections 448_m, 800_m and 080_m corresponds to $\sim 10^5$, with differences amongst the three in the 5% range. The value $|F_{hkl}|^2$ for the cubic $4\bar{4}0_c$ reflection, instead, is $\sim 7 \times 10^3$. After volume normalisation, $|F_{hkl}|^2$ for the cubic $4\bar{4}0_c$ corresponds to 1/4 of the monoclinic structure factors , in qualitative agreement with the observed decay in the peak intensity. The absence of a quantitative agreement in the intensity evolution is due multiple factors: the optimisation of the diffraction intensity in the high-temperature phase before cooling down, the structural change in the β angle in the monoclinic cell causing a deviation from the optimal diffraction conditions and the increased roughness of the probed surface after microtwinning.
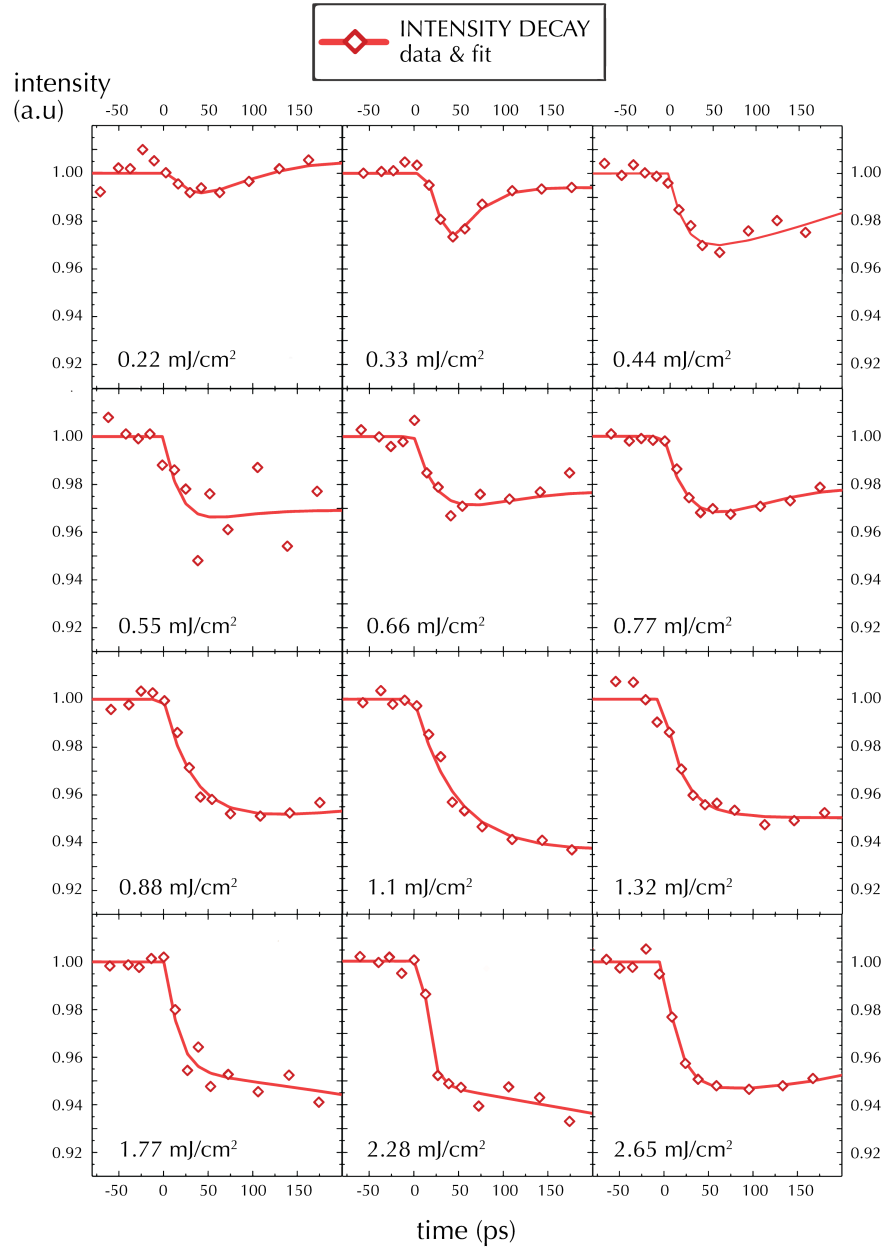
Figure 5.13: Intensity decay of the composite diffraction peak as a function of time for twelve investigated pump fluences ranging from 0.22 to 2.65 mJ/cm². Two different behaviours can be observed: at low fluences a recovery of the scattered intensity after the initial quench is observed, while at fluences higher than a threshold value of $\sim$ 0.9 - 1 mJ/cm² the intensity continues decaying at a lower rate.
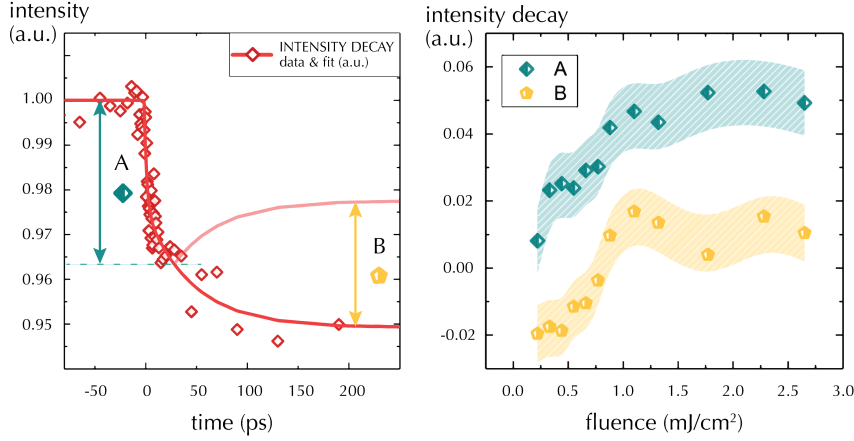
Figure 5.14: Pump fluence dependence of the initial drop in intensity - parameter A, green diamonds - and the slower intensity behaviour - parameter B (yellow pentagons). The two parameters behaves differently: the initial quench is present for all the investigated fluences, while the longer-time evolution of the intensity presents a threshold at a fluence value of ~ 1 mJ/cm^2. The coloured areas represent a b-spline of the calculated error interval.

5.5.4 *Photoinduced transient phase transition*

The second section of the experiments was performed at a temperature of ~ 40 K, with the aim to photoinduce the Verwey transition in the magnetite crystal and to study its mechanism. Detailed investigation was performed for fluence values of 2.28 and 3.4 mJ/cm^2.

In Fig. 5.12 we report the temporal evolution of the observed diffraction peak intensity (red diamonds), strain of the related family of planes (blue pentagons) and amplitude (green hexagons) - evaluated as FWHM - for the fluence values of 2.28 mJ/cm^2 and 3.54 mJ/cm^2. In the case of 2.28 mJ/cm^2, we observe a $\sim 5\%$ decay in the peak intensity, a strain of $\sim 3.5 \times 10^{-3}$ of the spacing and a narrowing of the composite peak amplitude of $\sim$ 10-11 %. With a pump fluence value of 3.54 mJ/cm^2, a $\sim 6\%$ decay in the peak intensity, a strain of $\sim 3.7 \times 10^{-3}$ of the spacing and a narrowing of the composite peak amplitude of $\sim$ 13.5 % are retrieved.

The observed dynamics can be fitted by biexponential decays with two time constants: a fast constant $\tau_1 \approx$ 2-2.5 ps and a slower constant $\tau_2 \approx 60 - 80$ ps. The intensity decay and the lattice contraction have been further investigated as a function of the pump fluence. In fig. 5.13 we report the intensity decay as a function of twelve different investigated fluences.

Two different behaviours can be observed. At fluences lower than a threshold value of ~ 1 mJ/cm^2, after an initial decrease in the order of 1.8-2.5 ps, we assist to a recovery of the scattering intensity. Complete recovery of the initial intensity is suspected happening only on a microseconds timescale, due to the low thermal conductivity of the system [261]. Conversely, at fluences higher than the threshold value,

a monotonic decrease of the peak intensity is observed after the initial quench with a longer time constant. Our observation are in good agreement with the results of the recent x-rays study from de Jong *et al.* [251]. Similarly to what done in that work, we plot two different features related to the intensity decay as a function of the fluence (see Fig. 5.14). The parameter A (green diamonds) evaluate the initial quench of the intensity. The parameter B (yellow pentagons) is related to the long-term behaviour of the intensity decay. In the B plot, the zero is associated to the intensity value at the end of the fast quench, thus negative values correspond to intensity recovery after the initial quench, while positive values define a persistence in the intensity decay.

Figure 5.15 contains plots of the reticular strain of the composite peak as a function of time for twelve values of fluence. A summary is reported in figure 5.16, where the average strain value after 150 ps is plotted as a function of the pump fluence. A fluence threshold at ~ 0.5 mJ/cm^2 is recognised, which can be ascribed to the effective observation of the Verwey transition. At lower values no strain in the lattice is observable, due to an insufficient energy transfer to trigger the phase transition.

In the fluence interval between 0.5 and 1.75 mJ/cm^2, the recorded compressive strain is proportional to the fluence increase. At fluences higher than 1.75 mJ/cm^2, the lattice strain reaches a saturation value of $\sim 3.5 - 4 \times 10^{-3}$ and the distortion does not show any further dependence on the pump fluence. As a note, the strain value at 3.54 mJ/cm^2, not corresponding to any time profile in figure 5.15, is related to the time decay shown in figure 5.12.

In the LT regime, we could not investigate any fluence higher than the reported value of 3.54 mJ/cm^2. Due to the low thermal conductivity of the monocline phase, higher fluences cause the thermalisation of the substrate and thus its thermal phase transition. The comparison of the peak features with pump fluences above this threshold value with the results shown in figure 5.11 confirms this scenario. Nevertheless, a time resolved experiment at 4.5 mJ/cm^2 have been performed to double check the obtained data to the ones collected at room temperature and contained in figure 5.8.

The evolution of the strain and the amplitude of the $[4\bar{4}0]_c$ Bragg peak are reported in figure 5.17. We can observe an initial behaviour (lattice expansion and peak amplitude broadening) similar to the RT measurement displayed in figure 5.8, thus confirming the happened thermal phase transition of the sample. However, in the 100-ps timescale, different behaviours can be observed, probably due to the sample thermal stress. Presumably for similar reason, no clear dynamics is retrieved in the peak intensity, that is thus omitted.
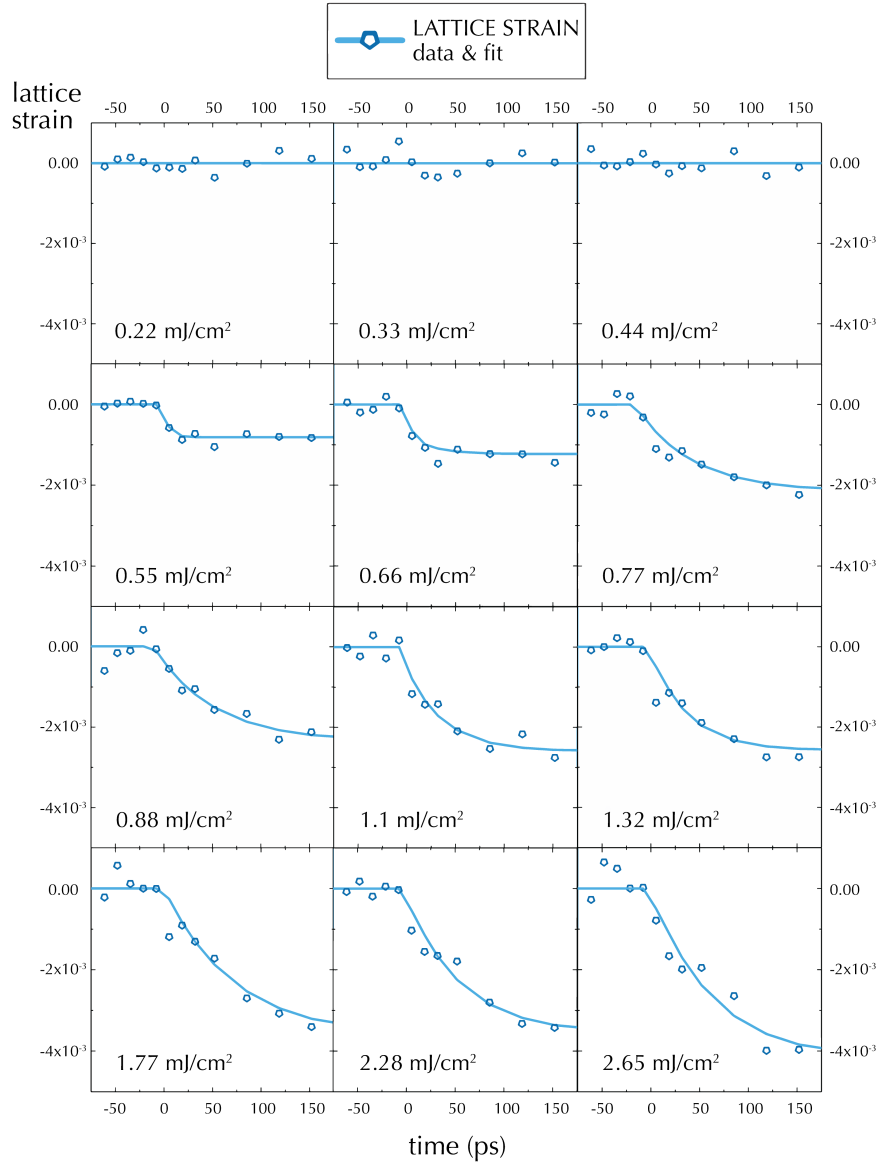
Figure 5.15: Lattice average strain as a function of time for twelve investigated pump fluences ranging from 0.22 to 2.65 mJ/cm². A threshold value of ~ 0.5 mJ/cm² can be observed: at lower fluences, no clear dynamics is visible, while at higher fluences a compressive strain is evidenced in the data.
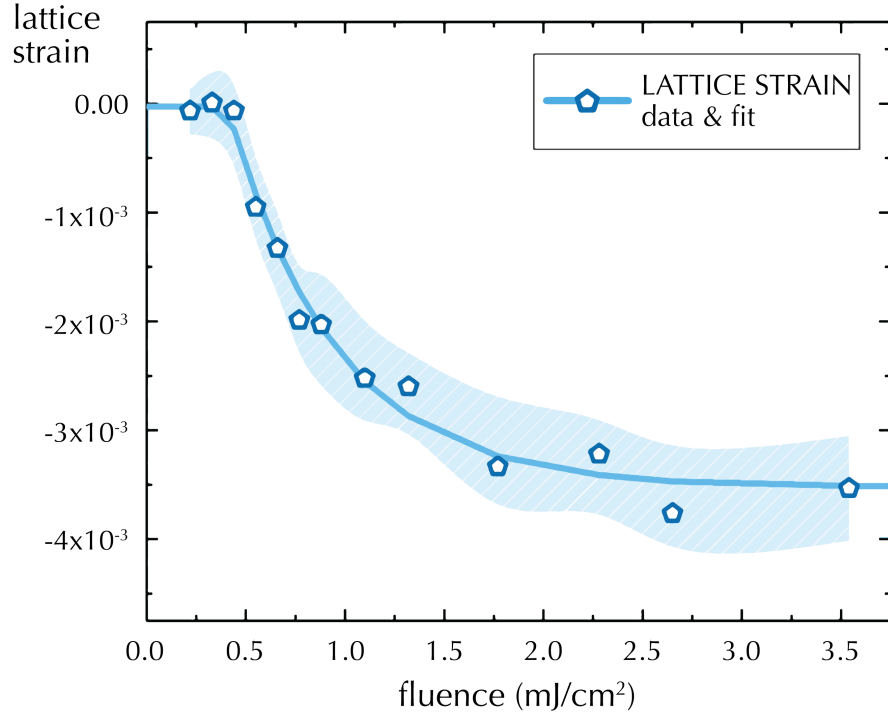
Figure 5.16: Fluence dependance of the observed strain relative at the composite diffraction peak during the phase transition. A fluence threshold at ~ 0.5 mJ/cm^2 is recognised, which can be ascribed to the effective observation of the Verwey transition. In the fluence interval between 0.5 and 1.75 mJ/cm^2, the recorded compressive strain is proportional to the fluence increase. At fluences higher than 1.75 mJ/cm^2, the lattice strain reaches a saturation value of $\sim 3.5 - 4 \times 10^{-3}$ and the distortion does not show any further dependence on the pump fluence. The coloured area represents the b-spline of the calculated error interval.
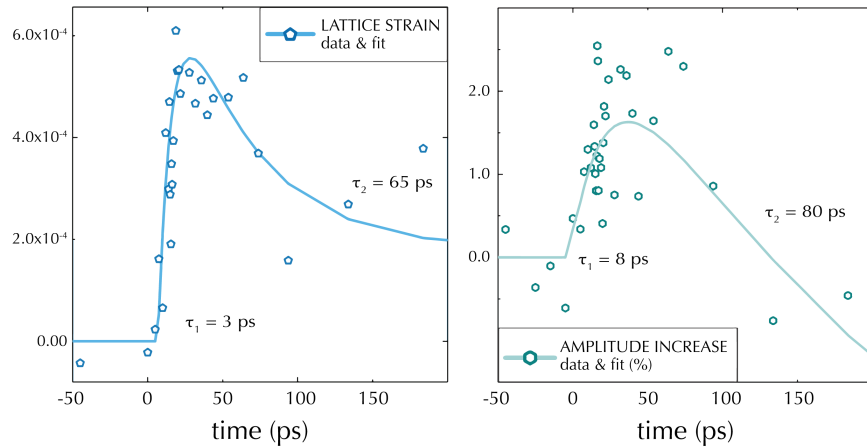
Figure 5.17: Laser-induced high temperature phase dynamics: lattice strain (blue pentagons) and amplitude variation (green exagons) of the $[4\bar{4}0]_c$ diffraction peak plotted as a function of the time. An initial behaviour similar to the RT measurement is observed in both the expansion of the crystal and the amplitude of the Bragg peak. At longer timescales, we observe a different trend in the data as respect to the RT experiments (see Fig. 5.8). Presumably, the thermal stress applied to the sample in this condition is responsible to the observed differences.

5.6 DISCUSSIONS

5.6.1 *Room temperature dynamics*

The room temperature dynamics can be understood as the out-of-equilibrium thermal expansion of the cubic lattice induced by laser heating. The observed dynamics of intensity, amplitude and lattice strain shown in figure 5.8 concur to the validation of this scenario. Moreover, the linear dependance of the intensity decay and the lattice strain as respect to the incoming fluence serves as a further confirmation of the lattice expansion in the crystal, and the retrieved strain values show good agreement with the literature [262].

5.6.2 *Thermal phase transition*

The observation related to the thermal phase transition are in good agreement with the theoretical previsions and calculation. Crossing the phase transition from below, the differently oriented twins of the monocline cell convolve to the long-range cubic arrangement of the crystal exposing the $1\bar{1}0$ family of planes. This is mirrored in the diffraction pattern with the strong increase in the peak height and the narrowing of its amplitude (see Fig. 5.11). The observed average expansion of the lattice planes is also in agreement with the computed spacing of the investigated planes in the monoclinic phase as respect to the $4\bar{4}0$. Also, the decrease of the intensity of the peak is in qualitative agreement with the calculation of the structure factor $|F_{hkl}|^2$ of the involved reflections. The deviation from the quantitative value of 4:1 (monoclinic:cubic) is probably due to the twinning phenomena, to the increased roughness of the sample in the monoclinic phase and from a mismatch from the optimal scattering condition of the monoclinic phase, as the optimisation of the diffraction pattern was performed for the high-temperature phase at the begining of the experiments.

5.6.3 *Photoinduced phase transition - intensity decay*

The observed composite intensity decay is in agreement with the observations reported in [251]. The initial fast decay corresponds to carrier excitation and subsequent annihilation of the long range network of frozen trimerons. The evolution of the system is strongly fluent-dependent. At low fluences, the trimerons network is reestablished after some tenth of picoseconds and the crystal maintains a monoclinic structure (recovery of the peak intensity). At fluences higher than a threshold value, the trimeron network is compromised and the system slowly evolves to the high temperature cubic phase (monotonic decay of the peak intensity). The threshold effect is clearly visible in

figure 5.14. The phase transition is accompanied by phenomena of phase segregation, where the presence of island of monoclinic phase in a percolate network of cubic phase is retrieved [251, 252].

5.6.4 *Photoinduced phase transition - lattice strain*

The observed strain in the phase transition presents a strong dependance from the pumping fluence. A threshold value of 0.5 mJ/cm^2 is identified. At lower values, the energy absorbed by the sample is not enough to induce the phase transition. At values of 1.8 mJ/cm^2 and higher, the observed compressive strain reaches a saturation value.

In the high statistic experiments, the presence of a standstill in the strain dynamics at a time of 10-40 ps is observed. A hint of the presence of this plateau is also visible in many of the low statistic dynamics shown in figure 5.15. However, due to the lack of time resolution, it is hard to identify any fluence dependent behaviour of this feature. A similar behaviour was observed by Hu [19] in diffraction from germanium telluride. A plateau in the scattering vector variation as a function of time have been explained as the result of two dynamics of different nature and with different timescales. In our case, a clear attribution of the involved dynamics have not been possible, due to the complexity of the involved phase transition. Further investigation would be required to better understand this feature.

5.6.5 *Comparison between thermal and photoinduced phase transition*

We compared the measured dynamics between the photoinduced and the thermal phase transition. As a first approximation, the photoinduced and thermal dynamics show similar trends.

However, a first discrepancy related to the different magnitude of the observed dynamics is detected. As visible in the decays in figure 5.11 and 5.12, during the photoinduced Verwey transition we do not assist to the complete recovery of the diffraction peak characteristic of the cubic phase. This observation suggests the coexistence of a superficial cubic phase with a monoclinic phase localised more in depth during the photoinduced phase transition, and it is in agreement with the narrow penetration depth of 800 nm laser in magnetite of the order of 10-20 nm (obtained from the absorption coefficient at 800 nm in [263] et and [264]).

We observe a similar quantitative trend in the decay of the intensity and the amplitude. The intensity decay for fluences corresponding to the saturation regime corresponds to $\sim$ 5%. If normalised to the value of $\sim$ 25% observed for the thermal transition, a factor of 0.2 is obtained. The peak amplitude presents a similar behaviour, with a narrowing of the $\sim$ 12% in the photoinduced transition and of the $\sim$

60% during the thermal one, again giving a normalised factor of 0.2. Following these observations, we propose as a rough approximation that only 1/5 of the probed volume undergoes the phase transition in the photoinduced experiment.

The most unexpected result in the photoinduced phase transition concerns the strain direction, which is the only parameter in qualitative disagreement with the thermal phase transition. While the thermal experiment and the calculation agree on an expansion of the observed family of planes, the photoinduced data show an evident contraction of the same. To explain the observed discrepancy, a scenario is proposed, related to a possible different statistical distribution of the twins population at the sample surface, for this particular sample and exposed family of planes. As sketched in figure 5.10, the $\mathbf{c}_m$ axis can indifferently establish along the $\mathbf{a}_c$, $\mathbf{b}_c$ and $\mathbf{c}_c$ axis while crossing the Verwey transition. However, due to the orientation of the sample, monoclinic cells orienting their $\mathbf{c}_m$ axis along directions with components in the out-of-plane coordinate would experience the impossibility to have a network of complete unit cell. This interruption of the long range network of stabilised trimerons would leave that particular superficial twin in a higher energy state than the ones orienting their $\mathbf{c}_m$ axis in the plane direction. So it is reasonable to assume that superficial twins preferentially show this latter configuration because of a more favourable energetic state. This orientation of the monoclinic cell statistically favours the exposition of the $[800]_m$ family of planes - the one undergoing a compressive strain during the phase transition. The surface sensitivity of our probe in the order of few tenth of nanometers would thus give a qualitative response to the observed strain dynamics. However, the proposed scenario is far from being quantitatively addressed, and the micrometer dimension of the twins does not completely fits into this model. A second possible explanation is the variation of the energy landscape due to photoexcitation, leading the system to different minima in case of photoinduced or thermally-driven phase transition (see figure 5.18).

To validate one or the other scenario, further experiments should be designed to explore magnetite samples crystallographically oriented in different ways. Proper evaluation of the cubic and monocline structure should be performed to carefully identify crystal orientations where certain twins are not energetically favoured as respect to the others.

5.7 CONCLUSIONS AND PERSPECTIVES

In this chapter, we studied the structural dynamics related to the Verwey transition in magnetite. Despite the manifested complexity due to the presence of the microtwinning phenomenon, we have been able to retrieve information concerning the phase transition dynamics. Ev-
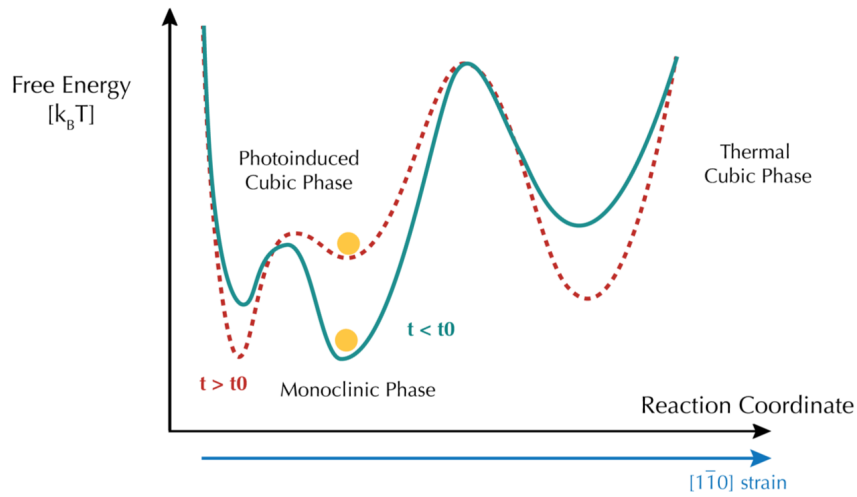
Figure 5.18: Qualitative rendering of the energy landscape variation across the Verwey Transition.

idence of the effective Verwey transition can be found in the qualitative agreement between the thermal and the photoinduced transition.

A composite dynamics of the peak intensity confirmed a previously formulated model of phase segregation during the Verwey transition. The anomalous direction of the strain across the phase transition have been explained through a surface-driven statistical distribution of the twins in the crystal or through the presence of a variable energy landscape, which differs between the thermally-driven and the photoinduced phase transition. Further investigation is required to prove the validity of the proposed scenario.

Moreover, as 400 nm light have been proved able to freeze the electronic states typical of the delocalised HT structure into the localised states of the LT phase [253], it would be desirable to repeat the performed experiment with the new pumping wavelength, resonant for the Fe-O electron transfer. The main interest feature for this experiment is to verify the eventual presence of a strong electron-lattice interplay, able to induce the Verwey transition from cubic to monoclinic, only by means of charge ordering processes.

CONCLUSIONS

This doctoral work was dedicated to the enhancement of the potential of a Ultrafast Electron Diffraction setup. After initial successful experiments on 2D-supracrystals, able to disclose order-disorder and local stiffness phenomena, a main accomplishment was the design and development of a pulse front tilting system able to increase the time resolution of the technique also for mm^2 size samples measured in reflection geometry.

The successful enhancement of this sub-500 fs time resolution allowed the investigation of two solid state systems of actual interest: graphite and magnetite. In graphite, we have been able to visualise the population of the SCOPs modes. Despite it has already been previously observed, we remark that it is the first time that the graphite ultrafast intensity decay was observed in a Ultrafast Electron Diffraction experiment operating in reflection geometry.

In magnetite, despite the complex problem due to microtwinning phenomena happening during the phase transition, we have been able to successfully identify features characteristic to the Verwey transition, happening in presence of phase segregation phenomena. During the investigation, a strong difference in the thermal and the photoinduced phase transition was observed and we propose a model to explain this discrepancy. Further experiments in magnetite would be needed to deepen the understanding of the complex interplay between structural and electronic degrees of freedom in this system.

In conclusion, I demonstrated the extreme versatility of the Ultrafast Electron Diffraction technique, whose insight have ranged from the characterisation of 2D-supracrystals of alkanethiol-capped gold nanoparticles and the disclosure of order-disorder phenomena to the observation of phase transitions in complex crystals, like magnetite.

This work open the pathway toward a better understanding of the structural dynamics at the surface of real bulky samples, needing a high electron flux and a sub-500 fs time resolution.

[1]   E. Muybridge. *Animals in Motion*. Dover Publications, 2012.

[2]   David Mitchell. *Cloud Atlas*. Hachette UK, 2008.

[3]   Beyoncé Knowles. *Run the World (Girls)*.

[4]   Bragg WH and Bragg WL. «The reflection of X-rays by crystals.» In: *Proceedings of the Royal Society of London. Series A, Containing Papers of a Mathematical and Physical Character* 88.605 (1913), pp. 428–438.

[5]   Laue Mv. «VI. Lorentz-Faktor und Intensitätsverteilung in Debye-Scherrer-Ringen.» In: *Zeitschrift für Kristallographie-Crystalline Materials* 64.1-6 (1926), pp. 115–142.

[6]   Thijs Van Oudheusden. «Electron source for sub-relativistic single-shot femtosecond diffraction.» PhD thesis. Technische Universiteit Eindhoven, 2010.

[7]   Ahmed H Zewail. «Femtochemistry: Atomic-scale dynamics of the chemical bond using ultrafast lasers (Nobel Lecture).» In: *Angewandte Chemie International Edition* 39.15 (2000), pp. 2586–2631.

[8]   Ahmed H Zewail. *Femtochemistry: ultrafast dynamics of the chemical bond*. Vol. 3. World Scientific, 1994.

[9]   M. Chergui and A.H. Zewail. «Electron and X-Ray Methods of Ultrafast Structural Dynamics: Advances and Applications.» In: *ChemPhysChem* 10.1 (2009), pp. 28–43.

[10] Andrea Cannizzo. «Ultrafast UV spectroscopy: from a local to a global view of dynamical processes in macromolecules.» In: *Physical Chemistry Chemical Physics* 14.32 (2012), pp. 11205–11223.

[11] Christian Bressler and Majed Chergui. «Ultrafast X-ray absorption spectroscopy.» In: *Chemical reviews* 104.4 (2004), pp. 1781–1812.

[12] Zewail AH. «4D ultrafast electron diffraction, crystallography, and microscopy.» In: *Annu. Rev. Phys. Chem.* 57 (2006), pp. 65–103.

[13] L Piazza, DJ Masiel, T LaGrange, BW Reed, B Barwick, and Fabrizio Carbone. «Design and implementation of a fs-resolved transmission electron microscope based on thermionic gun technology.» In: *Chemical Physics* 423 (2013), pp. 79–84.

[14] Yang DS, Gedik N, and Zewail AH. «Ultrafast electron crystallography. 1. Nonequilibrium dynamics of nanometer-scale structures.» In: *The Journal of Physical Chemistry C* 111.13 (2007), pp. 4889–4919.

[15]   Ruan CY, Vigliotti F, Lobastov VA, Chen S, and Zewail AH. «Ultrafast electron crystallography: Transient structures of molecules, surfaces, and phase transitions.» In: *Proceedings of the National Academy of Sciences of the United States of America* 101.5 (2004), pp. 1123–1128.

[16]   Sciaini G and Miller DRJ. «Femtosecond electron diffraction: heralding the era of atomically resolved dynamics.» In: *Reports on Progress in Physics* 74.9 (2011), p. 096101.

[17]   Baum P, Yang D-S, and Zewail AH. «4D visualization of transitional structures in phase transformations by electron diffraction.» In: *Science* 318.5851 (2007), pp. 788–792.

[18]   Gedik N, Yang D-S, Logvenov G, Bozovic I, and Zewail AH. «Nonequilibrium phase transitions in cuprates observed by ultrafast electron crystallography.» In: *Science* 316.5823 (2007), pp. 425–429.

[19]   Hu J, Vanacore GM, Yang Z, Miao X, and Zewail AH. «Transient structures and possible limits of data recording in phase-change materials.» In: *ACS nano* 9.7 (2015), pp. 6728–6737.

[20]   Morrison VR, Chatelain RP, Tiwari KL, Hendaoui A, A Bruhács, Chaker M, and Siwick BJ. «A photoinduced metal-like phase of monoclinic VO2 revealed by ultrafast electron diffraction.» In: *Science* 346.6208 (2014), pp. 445–448.

[21]   Sciaini G, Harb M, Kruglik SG, Payer T, Hebeisen CT, zu Heringdorf FJ-M, Yamaguchi M, Horn von Hoegen M, Ernstorfer R, and Miller DRJ. «Electronic acceleration of atomic motions and disordering in bismuth.» In: *Nature* 458.7234 (2009), p. 56.

[22]   Ruan CY, Lobastov VA, Vigliotti F, Chen S, and Zewail AH. «Ultrafast electron crystallography of interfacial water.» In: *Science* 304.5667 (2004), pp. 80–84.

[23]   Carbone F, Yang D-S, Giannini E, and Zewail AH. «Direct role of structural dynamics in electron-lattice coupling of superconducting cuprates.» In: *Proceedings of the National Academy of Sciences* 105.51 (2008), pp. 20161–20166.

[24]   Chatelain RP, Morrison VR, Klarenaar BLM, and Siwick BJ. «Coherent and incoherent electron-phonon coupling in graphite observed with radio-frequency compressed ultrafast electron diffraction.» In: *Physical review letters* 113.23 (2014), p. 235502.

[25]   Carbone F, Baum P, Rudolf P, and Zewail AH. «Structural preablation dynamics of graphite observed by ultrafast electron crystallography.» In: *Physical review letters* 100.3 (2008), p. 035501.

[26]   Mancini GF, Latychevskaia T, Pennacchio F, Reguera J, Stellacci F, and Carbone F. «Order/disorder dynamics in a dodecanethiol-capped gold nanoparticles supracrystal by small-angle ultrafast electron diffraction.» In: *Nano letters* 16.4 (2016), pp. 2705–2713.

[27] Vanacore GM, van der Veen RM, and Zewail AH. «Origin of axial and radial expansions in carbon nanotubes revealed by ultrafast diffraction and spectroscopy.» In: *ACS nano* 9.2 (2015), pp. 1721–1729.

[28] Vanacore GM, Hu J, Liang W, Bietti S, Sanguinetti S, and Zewail AH. «Diffraction of quantum dots reveals nanoscale ultrafast energy localization.» In: *Nano letters* 14.11 (2014), pp. 6148–6154.

[29] Frigge T, Hafke B, Tinnemann V, Witte T, and Horn von Hoegen M. «Spot profile analysis and lifetime mapping in ultrafast electron diffraction: Lattice excitation of self-organized Ge nanostructures on Si (001).» In: *Structural Dynamics* 2.3 (2015), p. 035101.

[30] Frigge T, Hafke B, Tinnemann V, Krenzer B, and Horn von Hoegen M. «Nanoscale heat transport from Ge hut, dome, and relaxed clusters on Si (001) measured by ultrafast electron diffraction.» In: *Applied Physics Letters* 106.5 (2015), p. 053108.

[31] Hu J, Vanacore GM, Cepellotti A, Marzari N, and Zewail AH. «Rippling ultrafast dynamics of suspended 2D monolayers, graphene.» In: *Proceedings of the National Academy of Sciences* 113.43 (2016), E6555–E6561.

[32] Streubühr C, Kalus A, Zhou P, Ligges M, Hanisch-Blicharski A, Kammler M, Bovensiepen U, Horn von Hoegen M, and von der Linde D. «Comparing ultrafast surface and bulk heating using time-resolved electron diffraction.» In: *Applied Physics Letters* 104.16 (2014), p. 161611.

[33] Mancini GF, Mansart B, Pagano S, Van Der Geer B, De Loos M, and Carbone F. «Design and implementation of a flexible beamline for fs electron diffraction experiments.» In: *Nuclear Instruments and Methods in Physics Research Section A: Accelerators, Spectrometers, Detectors and Associated Equipment* 691 (2012), pp. 113–122.

[34] Giulia Fulvia Mancini. *Femtosecond diffractive imaging of structures, charge and spin textures*. EPFL, 2015.

[35] Kiewiet FF, Kemper AH, Luiten OJ, Brussaard GJH, and Van der Wiel MJ. «Femtosecond synchronization of a 3GHz RF oscillator to a mode-locked Ti: sapphire laser.» In: *Nuclear Instruments and Methods in Physics Research Section A: Accelerators, Spectrometers, Detectors and Associated Equipment* 484.1 (2002), pp. 619–624.

[36] Mancini GF, Pennacchio F, Latychevskaia T, Reguera J, Stellacci F, and Carbone F. «Local photo-mechanical stiffness revealed in gold nanoparticles supracrystals by ultrafast small-angle electron diffraction.» In: (submitted work).

[37] Trustees of the British Museum. *Lycurgus Cup – British Museum*. 1997.

[38] Freestone I, Meeks N, Sax M, and Higgitt C. «The Lycurgus cup - a roman nanotechnology.» In: *Gold Bulletin* 40.4 (2007), pp. 270–277.

[39] Harden DB and Toynbee JMC. «VII.- The Rothschild Lycurgus Cup.» In: *Archaeologia* 97 (1959), pp. 179–212.

[40] Amendola V, Pilot R, Frasconi M, Maragò OM, and MA Iatì. «Surface plasmon resonance in gold nanoparticles: a review.» In: *Journal of Physics: Condensed Matter* 29.20 (2017), p. 203002.

[41] Brill RH. «The chemistry of the Lycurgus Cup.» In: (1965).

[42] Barber DJ and Freestone IC. «An investigation of the origin of the colour of the Lycurgus Cup by analytical transmission electron microscopy.» In: *Archaeometry* 32.1 (1990), pp. 33–45.

[43] Antonii F. «Panacea aurea-auro potabile.» In: *Hamburg: Ex Bibliopolio Frobeniano* 1618 (), p. 250.

[44] Kahn RL. «Serum diagnosis for syphilis.» In: *Colloid Chemistry* 2 (1928), p. 757.

[45] Gille Bertrand. *Histoire des techniques*. Gallimard, 1978.

[46] Kunckell J. «Nuetliche Observationes oder Anmerkungen von Auro und Argento Potabili, Schutzens, Hamburg, 1676.» In: *G. Savage, Glass and Glassware, Octopus Book, London* (1975).

[47] Hunt LB. «The true story of Purple of Cassius.» In: *Gold Bulletin* 9.4 (1976), pp. 134–139.

[48] Wilson R. «The use of gold nanoparticles in diagnostics and detection.» In: *Chemical Society Reviews* 37.9 (2008), pp. 2028–2045.

[49] Ueda A and Haruta M. «Nitric oxide reduction with hydrogen, carbon monoxide, and hydrocarbons over gold catalysts.» In: *Gold Bulletin* 32.1 (1999), pp. 3–11.

[50] Narayanan R and El-Sayed MA. *Catalysis with transition metal nanoparticles in colloidal solution: nanoparticle shape dependence and stability*. 2005.

[51] Chai F, Wang C, Wang T, Li L, and Su Z. «Colorimetric detection of Pb^{2+} using glutathione functionalized gold nanoparticles.» In: *ACS Applied Materials & Interfaces* 2.5 (2010), pp. 1466–1470.

[52] De la Fuente JM, Barrientos AG, Rojas TC, Rojo J, Fernández A, Penadés S, et al. «Gold Glyconanoparticles as Water-Soluble Polyvalent Models To Study Carbohydrate Interactions.» In: *Angewandte Chemie International Edition* 40.12 (2001), p. 2257.

[53] Saha K, Agasti SS, Kim C, Li X, and Rotello VM. «Gold nanoparticles in chemical and biological sensing.» In: *Chemical reviews* 112.5 (2012), pp. 2739–2779.

[54]   Rasheed PA and Sandhyarani N. «Electrochemical DNA sensors based on the use of gold nanoparticles: a review on recent developments.» In: *Microchimica Acta* 184.4 (2017), pp. 981–1000.

[55]   Venditti I. «Gold nanoparticles in photonic crystals applications: a review.» In: *Materials* 10.2 (2017), p. 97.

[56]   Dykman LA and Khlebtsov NG. «Gold nanoparticles in biology and medicine: recent advances and prospects.» In: *Acta Naturae* 3.2 (9) (2011).

[57]   Rosi NL and Mirkin CA. «Nanostructures in biodiagnostics.» In: *Chemical reviews* 105.4 (2005), pp. 1547–1562.

[58]   Kim C, Cho EC, Chen J, Song KH, Au L, Favazza C, Zhang Q, Cobley CM, Gao F, Xia Y, et al. «In vivo molecular photoacoustic tomography of melanomas targeted by bioconjugated gold nanocages.» In: *ACS nano* 4.8 (2010), pp. 4559–4564.

[59]   Huang X, Jain PK, El-Sayed IH, and El-Sayed MA. «Gold nanoparticles: interesting optical properties and recent applications in cancer diagnostics and therapy.» In: (2007).

[60]   Lal S, Clare SE, and Halas NJ. «Nanoshell-enabled photothermal cancer therapy: impending clinical impact.» In: *Accounts of chemical research* 41.12 (2008), pp. 1842–1851.

[61]   Her S, Jaffray DA, and Allen C. «Gold nanoparticles for applications in cancer radiotherapy: Mechanisms and recent advancements.» In: *Advanced drug delivery reviews* 109 (2017), pp. 84–101.

[62]   Wu X, Chen JY, Brech A, Fang C, Wang J, Helm PJ, and Peng Q. «The use of femto-second lasers to trigger powerful explosions of gold nanorods to destroy cancer cells.» In: *Biomaterials* 34.26 (2013), pp. 6157 –6162.

[63]   Levy R, Shaheen U, Cesbron Y, and See V. «Gold nanoparticles delivery in mammalian live cells: a critical review.» In: *Nano reviews* 1.1 (2010), p. 4889.

[64]   Papasani MR, Wang G, and Hill RA. «Gold nanoparticles: the importance of physiological principles to devise strategies for targeted drug delivery.» In: *Nanomedicine: Nanotechnology, Biology and Medicine* 8.6 (2012), pp. 804 –814.

[65]   Rana S, Bajaj A, Mout R, and Rotello VM. «Monolayer coated gold nanoparticles for delivery applications.» In: *Advanced Drug Delivery Reviews* 64.2 (2012), pp. 200 –216.

[66]   Shimizu T, TeranishiT, Hasegawa S, and Miyake M. «Size evolution of alkanethiol-protected gold nanoparticles by heat treatment in the solid state.» In: *The Journal of Physical Chemistry B* 107.12 (2003), pp. 2719–2724.

[67] Pong B-K, Elim HI, Chong J-X, Ji W, Trout BL, and Lee J-Y. «New insights on the nanoparticle growth mechanism in the citrate reduction of gold (III) salt: formation of the Au nanowire intermediate and its nonlinear optical properties.» In: *The Journal of Physical Chemistry C* 111.17 (2007), pp. 6281–6287.

[68] Sau TK and Murphy CJ. «Seeded high yield synthesis of short Au nanorods in aqueous solution.» In: *Langmuir* 20.15 (2004), pp. 6414–6420.

[69] Wang ZL, Mohamed MB, Link S, and El-Sayed MA. «Crystallographic facets and shapes of gold nanorods of different aspect ratios.» In: *Surface Science* 440.1-2 (1999), pp. L809–L814.

[70] Carbó-Argibay E, Rodríguez-González B, Pacifico J, Pastoriza-Santos I, Pérez-Juste J, and Liz-Marzán LM. «Chemical Sharpening of Gold Nanorods: The Rod-to-Octahedron Transition.» In: *Angewandte Chemie* 119.47 (2007), pp. 9141–9145.

[71] Oldenburg SJ, Averitt RD, Westcott SL, and Halas NJ. «Nanoengineering of optical resonances.» In: *Chemical Physics Letters* 288.2-4 (1998), pp. 243–247.

[72] Lu X, Au L, McLellan J, Li Z-Y, Marquez M, and Xia Y. «Fabrication of cubic nanocages and nanoframes by dealloying Au/Ag alloy nanoboxes with an aqueous etchant based on Fe (NO3) 3 or NH4OH.» In: *Nano letters* 7.6 (2007), pp. 1764–1769.

[73] Liang H-P, Wan L-J, Bai C-L, and Jiang L. «Gold hollow nanospheres: tunable surface plasmon resonance controlled by interior-cavity sizes.» In: *The Journal of Physical Chemistry B* 109.16 (2005), pp. 7795–7800.

[74] Kim F, Connor S, Song H, Kuykendall T, and Yang P. «Platonic gold nanocrystals.» In: *Angewandte Chemie* 116.28 (2004), pp. 3759–3763.

[75] Niu W, Zheng S, Wang D, Liu X, Li H, Han S, Chen J, Tang Z, and Xu G. «Selective synthesis of single-crystalline rhombic dodecahedral, octahedral, and cubic gold nanocrystals.» In: *Journal of the American Chemical Society* 131.2 (2008), pp. 697–703.

[76] Zhang J, Langille MR, Personick ML, Zhang K, Li S, and Mirkin CA. «Concave cubic gold nanocrystals with high-index facets.» In: *Journal of the American Chemical Society* 132.40 (2010), pp. 14012–14014.

[77] Ming T, Feng W, Tang Q, Wang F, Sun L, Wang J, and Yan C. «Growth of tetrahexahedral gold nanocrystals with high-index facets.» In: *Journal of the American Chemical Society* 131.45 (2009), pp. 16350–16351.

[78] Personick ML, Langille MR, Zhang J, Harris N, Schatz GC, and Mirkin CA. «Synthesis and isolation of {110}-faceted gold bipyramids and rhombic dodecahedra.» In: *Journal of the American Chemical Society* 133.16 (2011), pp. 6170–6173.

[79] Ma Y, Kuang Q, Jiang Z, Xie Z, Huang R, and Zheng L. «Synthesis of Trisoctahedral Gold Nanocrystals with Exposed High-Index Facets by a Facile Chemical Method.» In: *Angewandte Chemie International Edition* 47.46 (2008), pp. 8901–8904.

[80] Dreaden C, Alkilany AM, Huang X, Murphy CJ, and El-Sayed MA. «The golden age: gold nanoparticles for biomedicine.» In: *Chemical Society Reviews* 41.7 (2012), pp. 2740–2779.

[81] Boles MA, Engel M, and Talapin DV. «Self-assembly of colloidal nanocrystals: From intricate structures to functional materials.» In: *Chemical reviews* 116.18 (2016), pp. 11220–11289.

[82] Talapin DV, Lee J-S, Kovalenko MV, and Shevchenko EV. «Prospects of colloidal nanocrystals for electronic and optoelectronic applications.» In: *Chemical reviews* 110.1 (2010), pp. 389–458.

[83] Daniel MC and Astruc D. «Gold Nanoparticles: Assembly, Supramolecular Chemistry, Quantum-Size-Related Properties, and Applications toward Biology, Catalysis, and Nanotechnology.» In: *Chemical Reviews* 104.1, 293 (Aug. 2004), p. 346.

[84] Pileni M-P. «Self-assembly of inorganic nanocrystals: fabrication and collective intrinsic properties.» In: *Accounts of chemical research* 40.8 (2007), pp. 685–693.

[85] Fedlheim DL and Foss CA. *Metal Nanoparticles: Synthesis, Characterization, and Applications*. Taylor & Francis, 2001.

[86] Giner-Casares JJ and Reguera J. «Directed self-assembly of inorganic nanoparticles at air/liquid interfaces.» In: *Nanoscale* 8.37 (2016), pp. 16589–16595.

[87] Kim JY, Kwon SJ, Chang J-B, Ross CA, Hatton TA, and Stellacci F. «Two-Dimensional Nanoparticle Supracrystals: A Model System for Two-Dimensional Melting.» In: *Nano letters* 16.2 (2016), pp. 1352–1358.

[88] Badia A, Cuccia L, Demers L, Morin F, and Lennox RB. «Structure and dynamics in alkanethiolate monolayers self-assembled on gold nanoparticles: a DSC, FT-IR, and deuterium NMR study.» In: *Journal of the American Chemical Society* 119.11 (1997), pp. 2682–2692.

[89] Terrill RH, Postlethwaite TA, Chen C-H, Poon C-D, Terzis A, Chen A, Hutchison JE, Clark MR, and Wignall G. «Monolayers in three dimensions: NMR, SAXS, thermal, and electron hopping studies of alkanethiol stabilized gold clusters.» In: *Journal of the American Chemical Society* 117.50 (1995), pp. 12537–12548.

[90] Mueggenburg KE, Lin X-M, Goldsmith RH, and Jaeger HM. «Elastic membranes of close-packed nanoparticle arrays.» In: *Nature materials* 6.9 (2007), p. 656.

[91] *Langmuir and Langmuir-Blodgett Deposition Troughs*. KSV NIMA. 2012.

[92]   Whetten RL, Khoury JT, Alvarez MM, Murthy S, Vezmar I, Wang ZL, Stephens PW, Cleveland CL, Luedtke WD, and Landman U. «Nanocrystal gold molecules.» In: *Advanced materials* 8.5 (1996), pp. 428–433.

[93]   Brust M, Walker M, Bethell D, Schiffrin DJ, and Whyman R. «Synthesis of thiol-derivatised gold nanoparticles in a two-phase Liquid-Liquid system.» In: *Journal of the Royal Chemical Society , Chemical Communication* (7 1994), pp. 801–802.

[94]   Brust M and Kiely CJ. «Some recent advances in nanostructure preparation from gold and silver particles: a short topical review.» In: *Colloids and Surfaces A: Physicochemical and Engineering Aspects* 202.2-3 (2002), pp. 175–186.

[95]   Zheng N, Fan J, and Stucky GD. «One-step one-phase synthesis of monodisperse noble-metallic nanoparticles and their colloidal crystals.» In: *Journal of the American Chemical Society* 128.20 (2006), pp. 6550–6551.

[96]   Langmuir I and Schaefer VJ. «Activities of urease and pepsin monolayers.» In: *Journal of the American Chemical Society* 60.6 (1938), pp. 1351–1360.

[97]   Ong QK, Reguera J, Silva PJ, Moglianetti M, Harkness K, Longobardi M, Mali KS, Renner C, De Feyter S, and Stellacci F. «High-resolution scanning tunneling microscopy characterization of mixed monolayer protected gold nanoparticles.» In: *ACS nano* 7.10 (2013), pp. 8529–8539.

[98]   Van Oudheusden T, Pasmans PLEM, Van Der Geer SB, De Loos MJ, Van Der Wiel MJ, and Luiten OJ. «Compression of subrelativistic space-charge-dominated electron bunches for single-shot femtosecond electron diffraction.» In: *Physical review letters* 105.26 (2010), p. 264801.

[99]   Kiewiet FB, Kemper AH, Luiten OJ, Brussaard GJH, and Van der Wiel MJ. «Femtosecond synchronization of a 3 GHz RF oscillator to a mode-locked Ti: sapphire laser.» In: *Nuclear Instruments and Methods in Physics Research Section A: Accelerators, Spectrometers, Detectors and Associated Equipment* 484.1-3 (2002), pp. 619–624.

[100]   Musumeci P, Moody JT, Scoby CM, Gutierrez MS, and Westfall M. «Laser-induced melting of a single crystal gold sample by time-resolved ultrafast relativistic electron diffraction.» In: *Applied Physics Letters* 97.6 (2010), p. 063502.

[101]   Wochner P, Gutt C, Autenrieth T, Demmer T, Bugaev V, Ortiz AD, Duri A, Zontone F, Grübel G, and Dosch H. «X-ray cross correlation analysis uncovers hidden local symmetries in disordered matter.» In: *Proceedings of the National Academy of Sciences* 106.28 (2009), pp. 11511–11514.

[102]   Kurta RP, Altarelli M, Weckert E, and Vartanyants IA. «X-ray cross-correlation analysis applied to disordered two-dimensional systems.» In: *Physical Review B* 85.18 (2012), p. 184204.

[103]   Altarelli M, Kurta RP, and Vartanyants IA. «X-ray cross-correlation analysis and local symmetries of disordered systems: General theory.» In: *Physical Review B* 82.10 (2010), p. 104207.

[104]   Liu ACY, Neish MJ, Stokol G, Buckley GA, Smillie LA, de Jonge MD, Ott RT, Kramer MJ, and Bourgeois L. «Systematic mapping of icosahedral short-range order in a melt-spun Zr 36 Cu 64 metallic glass.» In: *Physical review letters* 110.20 (2013), p. 205505.

[105]   Kurta RP, Donatelli JJ, Yoon CH, Berntsen P, Bielecki J, Daurer BJ, DeMirci H, Fromme P, Hantke MF, Maia FRNC, et al. «Correlations in scattered x-ray laser pulses reveal nanoscale structural features of viruses.» In: *Physical review letters* 119.15 (2017), p. 158102.

[106]   Latychevskaia T, Mancini GF, and Carbone F. «The role of the coherence in the cross-correlation analysis of diffraction patterns from two-dimensional dense mono-disperse systems.» In: *Scientific reports* 5 (2015), p. 16573.

[107]   Latychevskaia T and Fink H-W. «Practical algorithms for simulation and reconstruction of digital in-line holograms.» In: *Applied optics* 54.9 (2015), pp. 2424–2434.

[108]   Bugayev A, Esmail A, Abdel-Fattah M, and Elsayed-Ali HE. «Coherent phonons in bismuth film observed by ultrafast electron diffraction.» In: *AIP Advances* 1.1 (2011), p. 012117.

[109]   Allen PB. «Theory of thermal relaxation of electrons in metals.» In: *Physical review letters* 59.13 (1987), p. 1460.

[110]   Raman RK, Murooka Y, Ruan C-Y, Yang T, Berber S, and Tománek D. «Direct observation of optically induced transient structures in graphite using ultrafast electron crystallography.» In: *Physical review letters* 101.7 (2008), p. 077401.

[111]   Esmail AR and Elsayed-Ali HE. «Anisotropic response of nano-sized bismuth films upon femtosecond laser excitation monitored by ultrafast electron diffraction.» In: *Applied Physics Letters* 99.16 (2011), p. 161905.

[112]   Ruan C-Y, Murooka Y, Raman RK, and Murdick RA. «Dynamics of size-selected gold nanoparticles studied by ultrafast electron nanocrystallography.» In: *Nano letters* 7.5 (2007), pp. 1290–1296.

[113]   Pennacchio F, Vanacore GM, Mancini GF, Oppermann M, Jayaraman R, Musumeci P, Baum P, and Carbone F. «Design and implementation of an optimal laser pulse front tilting scheme for ultrafast electron diffraction in reflection geometry with high temporal resolution.» In: *Structural Dynamics* 4.4 (2017), p. 044032.

[114]   Topp MR and Orner GC. «Group dispersion effects in picosecond spectroscopy.» In: *Optics Communications* 13.3 (1975), pp. 276–281.

[115] Schiller NH and Alfano RR. «Picosecond characteristics of a spectrograph measured by a streak camera/video readout system.» In: *Optics Communications* 35.3 (1980), pp. 451–454.

[116] Polland HJ, Elsaesser T, Seilmeier A, Kaiser W, Kussler M, Marx NJ, Sens B, and Drexhage KH. «Picosecond dye laser emission in the infrared between 1.4 and 1.8 μm.» In: *Applied Physics B: Lasers and Optics* 32.2 (1983), pp. 53–57.

[117] Bor Z, Szatmari S, and Müller A. «Picosecond pulse shortening by travelling wave amplified spontaneous emission.» In: *Applied Physics B: Lasers and Optics* 32.3 (1983), pp. 101–104.

[118] Barty CPJ, King DA, Yin GY, Hahn KH, Field JE, Young JF, and Harris SE. «96.9 nm Saturated Laser in Neutral Cesium.» In: *International Quantum Electronics Conference.* Optical Society of America. 1988, PD10.

[119] Kawachi T, Kado M, Tanaka M, Sasaki A, and Hasegawa N *et al.* «Gain saturation of nickel-like silver and tin x-ray lasers by use of a tabletop pumping laser system.» In: *Physical Review A* 66.3 (2002), p. 033815.

[120] Szabo G and Bor Z. «Broadband frequency doubler for femtosecond pulses.» In: *Applied Physics B: Lasers and Optics* 50.1 (1990), pp. 51–54.

[121] Fülöp JA, Major Z, Henig A, Kruber S, and Weingartner R *et al.* «Short-pulse optical parametric chirped-pulse amplification for the generation of high-power few-cycle pulses.» In: *New Journal of Physics* 9.12 (2007), p. 438.

[122] Kobayashi T and Shirakawa A. «Tunable visible and near-infrared pulse generator in a 5 fs regime.» In: *Applied Physics B: Lasers and Optics* 70.7 (2000), S239–S246.

[123] Hu BB, Darrow JT, Zhang X-C, Auston DH, and Smith PR. «Optically steerable photoconducting antennas.» In: *Applied Physics Letters* 56.10 (1990), pp. 886–888.

[124] Hebling J, Almasi G, Kozma IZ, and Kuhl J. «Velocity matching by pulse front tilting for large-area THz-pulse generation.» In: *Optics Express* 10.21 (2002), pp. 1161–1166.

[125] Stepanov AG, Hebling J, and Kuhl J. «Efficient generation of subpicosecond terahertz radiation by phase-matched optical rectification using ultrashort laser pulses with tilted pulse fronts.» In: *Applied physics letters* 83.15 (2003), pp. 3000–3002.

[126] Yeh K-L, Hoffmann MC, Hebling J, and KA Nelson. «Generation of 10 μ J ultrashort terahertz pulses by optical rectification.» In: *Applied Physics Letters* 90.17 (2007), p. 171121.

[127] Fülöp JA and Hebling J. «Applications of Tilted-Pulse-Front Excitation.» In: *Recent Optical and Photonic Technologies.* Ed. by Ki Young Kim. Rijeka: InTech, 2010. Chap. 11.

[128]   Torres JP, M Hendrych, and A Valencia. «Angular dispersion: an enabling tool in nonlinear and quantum optics.» In: *Applied Physics Letters* 2.2 (2010), pp. 319–369.

[129]   Baum P and Zewail AH. «Breaking resolution limits in ultrafast electron diffraction and microscopy.» In: *Proceedings of the National Academy of Sciences* 103.44 (2006), pp. 16105–16110.

[130]   Bor Z and Rácz B. «Group velocity dispersion in prisms and its application to pulse compression and travelling-wave excitation.» In: *Optics Communications* 54.3 (1985), pp. 165 –170. ISSN: 0030-4018.

[131]   Martinez OE. «Pulse distortions in tilted pulse schemes for ultrashort pulses.» In: *Optics communications* 59.3 (1986), pp. 229–232.

[132]   Hebling J. «Derivation of the pulse front tilt caused by angular dispersion.» In: *Optical and Quantum Electronics* 28.12 (1996), pp. 1759–1763.

[133]   Jenkins FA, White HE, et al. *Fundamentals of physical optics.* McGraw-Hill Book Company, 1937.

[134]   Kreier D and Baum P. «Avoiding temporal distortions in tilted pulses.» In: *Optics letters* 37.12 (2012), pp. 2373–2375.

[135]   Chanteloup J-C, Salmon E, Sauteret C, Migus A, and Zeitoun P *et al.* «Pulse-front control of 15-TW pulses with a tilted compressor, and application to the subpicosecond traveling-wave pumping of a soft-x-ray laser.» In: *Journal of the Optical Society of America B* 17.1 (2000), pp. 151–157.

[136]   Scoby CM, Li RK, and Musumeci P. «Effect of an ultrafast laser induced plasma on a relativistic electron beam to determine temporal overlap in pump–probe experiments.» In: *Ultramicroscopy* 127 (2013), pp. 14–18.

[137]   Park H, Hao Z, Wang X, Nie S, Clinite R, and Cao J. «Synchronization of femtosecond laser and electron pulses with sub-picosecond precision.» In: *Review of scientific instruments* 76.8 (2005), p. 083905.

[138]   Barwick B, Park HS, Kwon O-H, Baskin JS, and Zewail AH. «4D imaging of transient structures and morphologies in ultrafast electron microscopy.» In: *Science* 322.5905 (2008), pp. 1227–1231.

[139]   Dantus M, Kim SB, Williamson JC, and Zewail AH. «Ultrafast electron diffraction. 5. Experimental time resolution and applications.» In: *The Journal of Physical Chemistry* 98.11 (1994), pp. 2782–2796.

[140]   *Encyclopaedia Britannica.* URL: https://www.britannica.com.

[141]   Geckeler KE and Samal S. «Syntheses and properties of macromolecular fullerenes, a review.» In: *Polymer international* 48.9 (1999), pp. 743–757.

[142]   Various Author. *Mindat – the Hudson Institute of Mineralogy.* 1993. URL: https://www.mindat.org/min-2538.html.

[143]   Bernal BAJD. «The structure of graphite.» In: *Proc. R. Soc. Lond. A.* Vol. 106. 740. The Royal Society. 1924, pp. 749–773.

[144]   Wyckoff RWG. «Crystal Structures, vol. 2Wiley.» In: *New York, NY* 1 (1963).

[145]   Chung DDL. «Review graphite.» In: *Journal of materials science* 37.8 (2002), pp. 1475–1489.

[146]   Saito R, Jorio A, Souza Filho AG, Dresselhaus G, Dresselhaus MS, and Pimenta MA. «Probing phonon dispersion relations of graphite by double resonance Raman scattering.» In: *Physical review letters* 88.2 (2001), p. 027401.

[147]   Maultzsch J, Reich S, Thomsen C, Requardt H, and Ordejón P. «Phonon dispersion in graphite.» In: *Physical review letters* 92.7 (2004), p. 075501.

[148]   Kampfrath T, Perfetti L, Schapper F, Frischkorn C, and Wolf M. «Strongly coupled optical phonons in the ultrafast dynamics of the electronic energy and current relaxation in graphite.» In: *Physical review letters* 95.18 (2005), p. 187403.

[149]   Breusing M, Ropers C, and Elsaesser T. «Ultrafast carrier dynamics in graphite.» In: *Physical review letters* 102.8 (2009), p. 086809.

[150]   Moos G, Gahl C, Fasel R, Wolf M, and Hertel T. «Anisotropy of quasiparticle lifetimes and the role of disorder in graphite from ultrafast time-resolved photoemission spectroscopy.» In: *Physical review letters* 87.26 (2001), p. 267402.

[151]   Yang D-S, Baum P, and Zewail AH. «Ultrafast electron crystallography of the cooperative reaction path in vanadium dioxide.» In: *Structural Dynamics* 3.3 (2016), p. 034304.

[152]   *Optigraph GmbH.* URL: http://www.optigraph.eu.

[153]   Blackman LCF. «Stress recrystallization of graphite.» In: *Proc. R. Soc. Lond. A.* Vol. 266. 1324. The Royal Society. 1962, pp. 20–32.

[154]   Park H and J-M Zuo. «Comment on "Structural Preablation Dynamics of Graphite Observed by Ultrafast Electron Crystallography".» In: *Physical review letters* 105.5 (2010), p. 059603.

[155]   Carbone F, Baum P, Rudolf P, and Zewail AH. «Carbone et al. Reply.» In: *Physical Review Letters* 105.5 (2010), p. 059604.

[156]   Schäfer S, Liang W, and Zewail AH. «Structural dynamics and transient electric-field effects in ultrafast electron diffraction from surfaces.» In: *Chemical Physics Letters* 493.1 (2010), pp. 11–18.

[157]   Carbone F, O-H Kwon, and Zewail AH. «Dynamics of chemical bonding mapped by energy-resolved 4D electron microscopy.» In: *Science* 325.5937 (2009), pp. 181–184.

[158]   Carbone F. «The interplay between structure and orbitals in the chemical bonding of graphite.» In: *Chemical Physics Letters* 496.4 (2010), pp. 291–295.

[159]   Carbone F, Aubock G, Cannizzo A, Van Mourik F, Nair RR, Geim AK, Novoselov KS, and Chergui M. «Femtosecond carrier dynamics in bulk graphite and graphene paper.» In: *Chemical Physics Letters* 504.1 (2011), pp. 37–40.

[160]   Yan X-Q, Liu F, Kong X-T, Yao J, Zhao X, Liu Z-B, and Tian J-G. «Polarization dependence of graphene transient optical response: interplay between incident direction and anisotropic distribution of nonequilibrium carriers.» In: *Journal of the Optical Society of America B* 34.1 (2017), pp. 218–226.

[161]   Ishioka K, Hase M, Kitajima M, Wirtz L, Rubio A, and Petek H. «Ultrafast electron-phonon decoupling in graphite.» In: *Physical Review B* 77.12 (2008), p. 121402.

[162]   Pagliara S, Galimberti G, Mor S, Montagnese M, Ferrini G, Grandi MS, Galinetto P, and Parmigiani F. «Photoinduced π-π* Band Gap Renormalization in Graphite.» In: *Journal of the American Chemical Society* 133.16 (2011), pp. 6318–6322.

[163]   Schäfer S, Liang W, and Zewail AH. «Primary structural dynamics in graphite.» In: *New Journal of Physics* 13.6 (2011), p. 063030.

[164]   Yakovlev VS, Stockman MI, Krausz F, and Baum P. «Atomic-scale diffractive imaging of sub-cycle electron dynamics in condensed matter.» In: *Scientific reports* 5 (2015).

[165]   Harb M, Enquist H, Jurgilaitis A, Tuyakova FT, Obraztsov AN, and Larsson J. «Phonon-phonon interactions in photoexcited graphite studied by ultrafast electron diffraction.» In: *Physical Review B* 93.10 (2016), p. 104104.

[166]   Plutarch. *Moralia - On Isis and Osiris*. Vol. V. Parisiis - Editore Ambrosio Firmin Didot, 1841, p. 98.

[167]   Bostock J *et al.* «The wonders of various countries collected together.» In: *Naturalis Historiae. Pliny the Elder* II (1855), p. 98.

[168]   Germa Pierre. *Depuis quand? : le dictionnaire des inventions*. Solar, 1992.

[169]   Wilhelm Karl von Haidinger. *Handbuch der bestimmenden Mineralogie*. Wien – Braumüller and Seidel, 1845.

[170]   David Barthelmy. *Webmineral – the Mineralogy Database*. 1997. URL: http://webmineral.com/data/Magnetite.shtml.

[171]   Wallace R. «Amaze Your Friends! Lucretius on Magnets.» In: *Greece and Rome* 43.2 (1996), 178?187.

[172]   Du Trémolet de Lacheisserie E, Gignoux D, and Schlenker M. *Magnetism*. Collection Grenoble Sciences v. 1. Springer, 2005.

[173]   Pierre Pelerin de Maricourt. *Epistola Petri Peregrini de Maricourt ad Sygerum de Foucaucourt, militem, de magnete*. 1269.

[174]   William Gilbert. *De Magnete*. 1601.

[175]   Cornell RM and Schwertmann U. *The iron oxides*. 1996.

[176]   Kirschvink JL. «South-seeking magnetic bacteria.» In: *Journal of Experimental Biology* 86.1 (1980), pp. 345–347.

[177]   Blakemore R. «Magnetotactic bacteria.» In: *Science* 190.4212 (1975), pp. 377–379.

[178]   Bazylinski DA, Schlezinger DR, Howes BH, Frankel RB, and Epstein SS. «Occurrence and distribution of diverse populations of magnetic protists in a chemically stratified coastal salt pond.» In: *Chemical Geology* 169.3 (2000), pp. 319–328.

[179]   Walker MM and Bitterman ME. «Conditioned responding to magnetic fields by honeybees.» In: *Journal of comparative physiology A* 157.1 (1985), pp. 67–71.

[180]   Shcherbakov D, Winklhofer M, Petersen N, Steidle J, Hilbig R, and Blum M. «Magnetosensation in zebrafish.» In: *Current Biology* 15.5 (2005), R161–R162.

[181]   Meyer CG, Holland KN, and Papastamatiou YP. «Sharks can detect changes in the geomagnetic field.» In: *Journal of the Royal Society Interface* 2.2 (2005), pp. 129–130.

[182]   Mouritsen H and Ritz T. «Magnetoreception and its use in bird navigation.» In: *Current opinion in neurobiology* 15.4 (2005), pp. 406–414.

[183]   Walker MM, Kirschvink JL, Ahmed G, and Dizon AE. «Evidence that fin whales respond to the geomagnetic field during migration.» In: *Journal of Experimental Biology* 171.1 (1992), pp. 67–78.

[184]   Kirschvink JL, Walker MM, and Diebel CE. «Magnetite-based magnetoreception.» In: *Current opinion in neurobiology* 11.4 (2001), pp. 462–467.

[185]   Wiltschko R. *Magnetic orientation in animals*. Vol. 33. Springer Science & Business Media, 2012.

[186]   Kirschvink JL, Kobayashi-Kirschvink A, and Woodford BJ. «Magnetite biomineralization in the human brain.» In: *Proceedings of the National Academy of Sciences* 89.16 (1992), pp. 7683–7687.

[187]   Kirschvink JL, Kobayashi-Kirschvink A, Diaz-Ricci JC, and Kirschvink SJ. «Magnetite in human tissues: a mechanism for the biological effects of weak ELF magnetic fields.» In: *Bioelectromagnetics* 13.S1 (1992), pp. 101–113.

[188]   Banaclocha MAM, Bókkon I, and Banaclocha HM. «Long-term memory in brain magnetite.» In: *Medical hypotheses* 74.2 (2010), pp. 254–257.

[189]   Størmer FC. «Is magnetite a universal memory molecule?» In: *Medical hypotheses* 83.5 (2014), pp. 549–551.

[190]   Needham J, Ling W, and Robinson KG. *Science and Civilisation in China. Vol. 4: Physics and Physical Technology. Part. 1: Physics*. Cambridge, 1962.

[191] Benjamin P. *The intellectual rise in electricity: a history*. Longmans, Green, 1895.

[192] Daniel ED, Mee CD, and Clark MH. *Magnetic Recording: The First 100 Years*. Wiley, 1999.

[193] Hoagland AS. «History of magnetic disk storage based on perpendicular magnetic recording.» In: *IEEE transactions on magnetics* 39.4 (2003), pp. 1871–1875.

[194] Coey JMD and Chien CL. «Half-metallic ferromagnetic oxides.» In: *Mrs Bulletin* 28.10 (2003), pp. 720–724.

[195] Terris BD and Thomson T. «Nanofabricated and self-assembled magnetic structures as data storage media.» In: *Journal of physics D: Applied physics* 38.12 (2005), R199.

[196] Alivisatos P. «The use of nanocrystals in biological detection.» In: *Nature biotechnology* 22.1 (2004), pp. 47–52.

[197] Stephen ZR, Kievit FM, and Zhang M. «Magnetite nanoparticles for medical MR imaging.» In: *Materials Today* 14.7 (2011), pp. 330–338.

[198] Du Y, Lai PT, Leung CH, and Pong PWT. «Design of superparamagnetic nanoparticles for magnetic particle imaging (MPI).» In: *International journal of molecular sciences* 14.9 (2013), pp. 18682–18710.

[199] Mornet S, Vasseur S, Grasset F, and Duguet E. «Magnetic nanoparticle design for medical diagnosis and therapy.» In: *Journal of Materials Chemistry* 14.14 (2004), pp. 2161–2175.

[200] Schütt D. «Magnetite colloids for drug delivery and magnetic resonance imaging.» In: *Institute Angewandte Polymerforschung: thesis Selim MS, Cunningham LP, Srivastava R, Olson JM (1997)* (2004), pp. 108–111.

[201] Cui D, Han Y, Li Z, Song H, Wang K, He R, Liu B, Liu H, Bao C, and Huang P *et al.* «Fluorescent magnetic nanoprobes for in vivo targeted imaging and hyperthermia therapy of prostate cancer.» In: *Nano Biomed Eng* 1.1 (2009), pp. 94–112.

[202] Veiseh O, Gunn JW, and Zhang M. «Design and fabrication of magnetic nanoparticles for targeted drug delivery and imaging.» In: *Advanced drug delivery reviews* 62.3 (2010), pp. 284–304.

[203] Bakhtiary Z, Saei AA, Hajipour MJ, Raoufi M, Vermesh O, and Mahmoudi M. «Targeted superparamagnetic iron oxide nanoparticles for early detection of cancer: Possibilities and challenges.» In: *Nanomedicine: Nanotechnology, Biology and Medicine* 12.2 (2016), pp. 287–307.

[204] Revia RA and Zhang M. «Magnetite nanoparticles for cancer diagnosis, treatment, and treatment monitoring: recent advances.» In: *Materials Today* 19.3 (2016), pp. 157–168.

[205]   Sincai M, Ganga D, Ganga M, Argherie D, and Bica D. «Anti-tumor effect of magnetite nanoparticles in cat mammary adenocarcinoma.» In: *Journal of magnetism and magnetic materials* 293.1 (2005), pp. 438–441.

[206]   Bañobre-López M, Teijeiro A, and Rivas J. «Magnetic nanoparticle-based hyperthermia for cancer treatment.» In: *Reports of Practical Oncology & Radiotherapy* 18.6 (2013), pp. 397–400.

[207]   Cao S-W, Zhu Y-J, Ma M-Y, Li L, and Zhang L. «Hierarchically nanostructured magnetic hollow spheres of Fe3O4 and γ-Fe2O3: preparation and potential application in drug delivery.» In: *The Journal of Physical Chemistry C* 112.6 (2008), pp. 1851–1856.

[208]   Barry BW. «Drug delivery routes in skin: a novel approach.» In: *Advanced drug delivery reviews* 54 (2002), S31–S40.

[209]   Roger J, Pons JN, Massart R, Halbreich A, and Bacri JC. «Some biomedical applications of ferrofluids.» In: *The European Physical Journal Applied Physics* 5.3 (1999), pp. 321–325.

[210]   Kurinobu S, Uesugi J, Utumi Y, and Kasahara H. «Performance of HGMS filter and recycling of magnetic seeding material on magnetic seeding method.» In: *IEEE transactions on magnetics* 35.5 (1999), pp. 4067–4069.

[211]   Ebner AD, Ritter JA, Ploehn HJ, Kochen RL, and Navratil JD. «New magnetic field-enhanced process for the treatment of aqueous wastes.» In: *Separation Science and Technology* 34.6-7 (1999), pp. 1277–1300.

[212]   Rikers RA, Voncken JHL, and Dalmijn WL. «Cr-polluted soil studied by high gradient magnetic separation and electron probe.» In: *Journal of Environmental Engineering* 124.12 (1998), pp. 1159–1164.

[213]   Honda H, Kawabe A, Shinkai M, and Kobayashi T. «Development of chitosan-conjugated magnetite for magnetic cell separation.» In: *Journal of fermentation and bioengineering* 86.2 (1998), pp. 191–196.

[214]   Berger P, Adelman NB, Beckman KJ, Campbell DJ, Ellis AB, and Lisensky GC. «Preparation and properties of an aqueous ferrofluid.» In: *J. Chem. Educ* 76.7 (1999), p. 943.

[215]   Ferrotec USA. *Ferrofluidic Seals and Vacuum Technology*. 2001-2018. URL: https://seals.ferrotec.com/technology/.

[216]   Blaney L. «Magnetite (Fe3O4): Properties, synthesis, and applications.» In: *Lehigh University Review* (2007).

[217]   Rosensweig RE. «Magnetic fluids.» In: *Annual review of fluid mechanics* 19.1 (1987), pp. 437–461.

[218]   Tsori Y and Steiner U. *Polymers, Liquids and Colloids in Electric Fields: Interfacial Instabilities, Orientation and Phase Transitions.* Series in soft condensed matter. World Scientific, 2009.

[219]   Bragg William Henry. «XXX. The structure of the spinel group of crystals.» In: *The London, Edinburgh, and Dublin Philosophical Magazine and Journal of Science* 30.176 (1915), pp. 305–315.

[220]   Claassen AA. «The scattering power of oxygen and iron for X-rays.» In: *Proceedings of the Physical Society of London* 38.1 (1926), p. 482.

[221]   Verwey EJW and De Boer JH. «Cation arrangement in a few oxides with crystal structures of the spinel type.» In: *Recueil des Travaux Chimiques des Pays-Bas* 55.6 (1936), pp. 531–540.

[222]   Fleet ME. «The structure of magnetite.» In: *Acta Crystallographica Section B: Structural Crystallography and Crystal Chemistry* 37.4 (1981), pp. 917–920.

[223]   Néel ML. «Propriétés magnétiques des ferrites; ferrimagnétisme et antiferromagnétisme.» In: *Annales de Physique*. Vol. 12. 1948, pp. 137–198.

[224]   Shull CG, Wollan EO, and Koehler WC. «Neutron scattering and polarization by ferromagnetic materials.» In: *Physical Review* 84.5 (1951), p. 912.

[225]   Goodenough JB and Loeb AL. «Theory of ionic ordering, crystal distortion, and magnetic exchange due to covalent forces in spinels.» In: *Physical Review* 98.2 (1955), p. 391.

[226]   Verwey EJW. «Electronic conduction of magnetite (Fe_3O_4) and its transition point at low temperatures.» In: *Nature* 144.3642 (1939), pp. 327–328.

[227]   Verwey EJ, Haayman PW, and Romeijn FC. «Physical properties and cation arrangement of oxides with spinel structures II. Electronic conductivity.» In: *The Journal of Chemical Physics* 15.4 (1947), pp. 181–187.

[228]   Walz F. «The Verwey transition-a topical review.» In: *Journal of Physics: Condensed Matter* 14.12 (2002), R285.

[229]   Weiss P and Forrer R. «The absolute saturation of ferro-magnetic and laws of approach according to the field and the temperature.» In: *Ann. Physique* 12.10 (1929), p. 279.

[230]   Millar RW. «The heat capacities at low temperatures of ferrous oxide, magnetite and cuprous and cupric oxides.» In: *Journal of the American Chemical Society* 51.1 (1929), pp. 215–222.

[231]   Okamura T. «Transformation of Magnetite at a Low Temperature.» In: *Scientific Reports of the Research Institutes of Tohoku University* 21 (1932), p. 231.

[232]   Bickford Jr LR. «The low temperature transformation in ferrites.» In: *Reviews of Modern Physics* 25.1 (1953), p. 75.

[233]   Karl Renger. «Die anfängliche Suszeptibilität von Eisen und Magnetit in Abhängigkeit von der Temperatur.» PhD thesis. 1913.

[234]   Parks GS and Kelley KK. «The heat capacities of some metallic oxides.» In: *The Journal of Physical Chemistry* 30.1 (1926), pp. 47–55.

[235]   Tombs NC and Rooksby HP. «Structure transition and antiferromagnetism in magnetite.» In: *Acta Crystallographica* 4.5 (1951), pp. 474–475.

[236]   Abrahams SC and Calhoun BA. «The low-temperature transition in magnetite.» In: *Acta Crystallogr.* 6.1 (Jan. 1953), pp. 105–106.

[237]   Hamilton WC. «Neutron diffraction investigation of the 119 K transition in magnetite.» In: *Physical Review* 110.5 (1958), p. 1050.

[238]   Abrahams SC and Calhoun BA. «A magneto–X-ray study of magnetite at 78°K.» In: *Acta Crystallogr.* 8.5 (1955), pp. 257–260.

[239]   Samuelsen EJ, Bleeker EJ, Dobrzynski L, and Riste T. «Neutron scattering from magnetite below 119 K.» In: *Journal of Applied Physics* 39.2 (1968), pp. 1114–1115.

[240]   Shirane G, Chikazumi S, Akimitsu J, Chiba K, Matsui M, and Fujii Y. «Neutron Scattering from Low-Temperature Phase of Magnetite.» In: *J. Phys. Soc. Jpn.* 39.4 (1975), pp. 949–957.

[241]   Yoshida J and Iida S. «X-Ray Diffraction Study on the Low Temperature Phase of Magnetite.» In: *J. Phys. Soc. Jpn.* 42.1 (Jan. 1977), pp. 230–237.

[242]   Iizumi M, Koetzle TF, Shirane G, Chikazumi S, Matsui M, and Todo S. «Structure of magnetite (Fe_3O_4) below the Verwey transition temperature.» In: *Acta Crystallographica Section B: Structural Crystallography and Crystal Chemistry* 38.8 (1982), pp. 2121–2133.

[243]   Wright JP, Attfield JP, and Radaelli PG. «Long range charge ordering in magnetite below the Verwey transition.» In: *Physical review letters* 87.26 (2001), p. 266401.

[244]   Wright JP, Attfield JP, and Radaelli PG. «Charge ordered structure of magnetite Fe_3O_4 below the Verwey transition.» In: *Physical Review B* 66.21 (2002), p. 214422.

[245]   Senn MS, Wright JP, and Attfield JP. «Charge order and three-site distortions in the Verwey structure of magnetite.» In: *Nature* 481.7380 (2012), pp. 173–176.

[246]   Fukushima T, Yamauchi K, and Picozzi S. «Ab initio investigations of Fe2+/Fe3+ bond dimerization and ferroelectricity induced by intermediate site/bond-centered charge ordering in magnetite.» In: *Journal of the Physical Society of Japan* 80.1 (2011), p. 014709.

[247]   Zhou F, Ceder G, et al. «First-principles determination of charge and orbital interactions in Fe 3 O 4.» In: *Physical Review B* 81.20 (2010), p. 205113.

[248] Seo H, Ogata M, and Fukuyama H. «Aspects of the Verwey transition in magnetite.» In: *Physical Review B* 65.8 (2002), p. 085107.

[249] Crystalmaker. URL: http://www.crystalmaker.com.

[250] Senn MS, Wright JP, Cumby J, and Attfield JP. «Charge localization in the Verwey structure of magnetite.» In: *Physical Review B* 92.2 (2015), p. 024104.

[251] De Jong S, Kukreja R, Trabant C, Pontius N, Chang CF, Kachel T, Beye M, Sorgenfrei F, Back CH, and Bräuer B *et al.* «Speed limit of the insulator–metal transition in magnetite.» In: *Nature materials* 12.10 (2013), pp. 882–886.

[252] Randi F, Vergara I, Novelli F, Esposito M, Dell'Angela M, Brabers VAM, Metcalf P, Kukreja R, Dürr HA, and Fausti D *et al.* «Phase separation in the nonequilibrium Verwey transition in magnetite.» In: *Physical Review B* 93.5 (2016), p. 054305.

[253] Borroni S, Baldini E, Katukuri VM, Mann A, Parlinski K, Legut D, Arrell C, van Mourik F, Teyssier J, and Kozlowski A *et al.* «Coherent generation of symmetry-forbidden phonons by light-induced electron-phonon interactions in magnetite.» In: *Physical Review B* 96.10 (2017), p. 104308.

[254] Mark Stephen Senn. «Charge, orbital and magnetic ordering in transition metal oxides.» PhD thesis. 2013.

[255] Borroni S, Tucker GS, Pennacchio F, Rajeswari J, Stuhr U, Pisoni A, Lorenzana J, Rønnow HM, and Carbone F. «Mapping the lattice dynamical anomaly of the order parameters across the Verwey transition in magnetite.» In: *New Journal of Physics* 19.10 (2017), p. 103013.

[256] Simone Borroni. «New Insights into the Verwey Transition in Magnetite.» PhD thesis. École Polytechnique Fédérale de Lausanne, 2018.

[257] Kasama T, Church NS, Feinberg JM, Dunin-Borkowski RE, and Harrison RJ. «Direct observation of ferrimagnetic/ferroelastic domain interactions in magnetite below the Verwey transition.» In: *Earth and Planetary Science Letters* 297.1 (2010), pp. 10–17.

[258] Coe RS, Egli R, Gilder SA, and Wright JP. «The thermodynamic effect of nonhydrostatic stress on the Verwey transition.» In: *Earth and Planetary Science Letters* 319 (2012), pp. 207–217.

[259] Surface Preparation Laboratory. URL: https://www.spl.eu.

[260] Prince E and Wilson AJC. «International tables for crystallography. Volume C: Mathematical, Physical and Chemical Tables.» In: (2004).

[261]   Pontius N, Kachel T, Schüßler-Langeheine C, Schlotter WF, Beye M, Sorgenfrei F, Chang CF, Foehlisch A, Wurth W, Metcalf P, et al. «Time-resolved resonant soft x-ray diffraction with free-electron lasers: Femtosecond dynamics across the Verwey transition in magnetite.» In: *Applied Physics Letters* 98.18 (2011), p. 182504.

[262]   Sharma SS. «Thermal expansion of crystals.» In: *Proceedings of the Indian Academy of Sciences-Section A*. Vol. 31. 4. Springer. 1950, pp. 261–274.

[263]   Querry MR. *Optical constants*. Tech. rep. Missouri University - Kansas City, 1985.

[264]   Schlegel A, Alvarado SF, and Wachter P. «Optical properties of magnetite (Fe_3O_4).» In: *Journal of Physics C: Solid State Physics* 12.6 (1979), p. 1157.

FRANCESCO PENNACCHIO

Chemin de Barberine 3, 1004 Lausanne, Switzerland
francesco.pennacchio89@gmail.com | +41 78 878 82 75 | Skype : francesco.g.pennacchio
https://www.linkedin.com/in/francesco-pennacchio

PERSONAL INFO

Italian nationality • 28 y.o.
Unmarried

SKILLS

PHYSICS AND CHEMISTRY

Optics • • • • •
Condensed Matter • • •
Solid State Physics • • • •
Crystallography • • • •
Nanomaterials • • •
Electron Diffraction • • • • •
Ultrafast Physics • • • • •
Ultra High Vacuum • • • •
Materials Science • • • •
Biomaterials • • •
Photomedicine • •
Data Analysis • • • •
Mechanics • • •
Thermodynamics • • • • •

INFORMATICS

MATLAB • • • •
Origin • • •
CrystalMaker • • •
LaTeX • • •
Adobe Lightroom • • • • •
Adobe Illustrator • • • • •
Blender • • •
Adobe Photoshop • • •
Powerpoint & Keynote • • • •
Microsoft Office • • •
WordPress •
Slack • • • •
Evernote • • • •
iMovie • • •

EDUCATION

ÉCOLE POLYTECHNIQUE FÉDÉRALE DE LAUSANNE

PhD Chemistry and Chemical Engineering (EDCH) – Mars 2018
Dec 2012 - Present | Lausanne, Switzerland

- Thesis : Spatio-temporal observation of dynamical structures in order-disorder phenomena and phase transitions via Ultrafast Electron Diffraction.
- Master Thesis project in the Laboratory for Ultrafast Microscopy and Electron Scattering (LUMES), via Erasmus Placement scolarship.

UNIVERSITÀ DEGLI STUDI DI PAVIA

Physical Chemistry | (MSc.)
Sept 2011 – Sept 2013 | Pavia, Italy
Dynamical ordering in an alkanethiols-coated gold nanoparticles 2D-assembly observed via Coherent Femtosecond Electron Diffraction
Final Note | 110/110

Chemistry | (BSc.)
Sept 2008 – Jul 2011 | Pavia, Italy
Organic-inorganic composite scaffolds for tissue engineering applications
Final Note | 110/110

RESEARCH EXPERIENCE

Ultrafast Electron Diffraction

Transition of an Ultrafast Electron Diffraction setup from transition to reflection geometry, to allow experiments on mm-sized samples surface with high temporal and spatial resolution. Full characterization of the system.

Order-disorder phenomena in 2D supracrystals

Investigation of photo-induced ordering phenomena in 2D supracrystals of capped gold nanoparticles with different cappiung ligands, by means of Ultrafast Electron Diffraction and Ultrafast Small-Angle Scattering alanysis. Experiments performed in transmission geometry.

Nonlinear Optics

Design, implementation and full characterization of a tilting scheme for URHEED experiments at 30 keV with optimized temporal pulse distortions to investigate structural dynamics in mm-sized samples, for both λ = 400 and 800 nm.

Out-of-equilibrium dynamics in graphite

Direct spatio-temporal visualization of electron-phonon coupling and successive phonon modes relaxation in a strongly-correlated system as graphite.

Light-control of the phase transitions in solids

Study of the Verwey transition in magnetite on a mm-sized sample. Evidence of different phase transition mechanisms between thermal- and photo-induced transition. Investigation via Ultrafast Reflection High-Energy Electron Diffraction.

LANGUAGES

ITALIAN
Native language

FRENCH
Full Professional Proficiency (C1)

ENGLISH
Full Professional Proficiency (C1)

SPANISH
Advanced Level (B2-C1)

GERMAN
Intermediate level (A2-B1)

ADDITIONAL COMPETENCES

COMMUNICATION

Photography • • • • •
Digital Photography • • • • •
Documentary Photography • • • •
Image Processing • • • •
Visual communication • • • • •
Graphics • • • •

SOFT SKILLS

Team Working
Team Leading
Negotiating
Problem Solving
Decision Making
Enthusiasm
Resilience
Flexibility
Independence
Creativity

TEACHING, TUTORING AND TRAINING

Teaching Responsible for the course *Thermodynamics*, for civil engineers. Spring term 2014, 2015, 2016.

Tutor for the course *Physics I*, for informatics engineers. Fall terms 2014, 2015, 2016.

Supervision of the students Brice Boissonneault and Andrea Muni during summer internships.

Supervision of the student Andrea Muni for his annual project, report "Ultrafast Electron Diffraction" evaluation.

Trained 4 users in a Ultrafast Electron Diffraction laboratory.

PUBLICATIONS

Design and implementation of an optimal laser pulse front tilting scheme for ultrafast electron diffraction in reflection geometry with high temporal resolution.
Pennacchio F, Vanacore GM, Mancini GF, Oppermann M, Jayaraman R, Musumeci P, Baum P, and Carbone F.
In: *Structural Dynamics* 4.4, p. 044032, 2017.

Order/disorder dynamics in a dodecanethiol- capped gold nanoparticles supracrystal by small-angle ultra- fast electron diffraction.
Mancini GF, Latychevskaia T, Pennacchio F, Reguera J, Stellacci F and Carbone F.
In: Nano letters 16.4, pp. 2705–2713, 2016.

Mapping the lattice dynamical anomaly of the order parameters across the Verwey transition in magnetite.
Borroni S, Tucker GS, Pennacchio F, Rajeswari J, Stuhr U, Pisoni A, Lorenzana J, Rønnow HM, and Carbone F.
In: New Journal of Physics 19.10, p. 103013, 2017.

Local photo-mechanical stiffness re- vealed in gold nanoparticles supracrystals by ultrafast small- angle electron diffraction.
Mancini GF, Pennacchio F, Latychevskaia T, Reguera J, Stellacci F, and Carbone F.
Submitted work.

Light-induced control of the Verwey transition in magnetite.
Pennacchio F, Sala V, Borroni S, Vanacore GM and Carbone F.
In preparation.

COMPLEMENTARY EXPERIENCE

PRESIDENT
Sep 2016 - Nov 2017 | Photo Club EPFL | Lausanne, Switzerland
Coordinating a team of around 100 passionate photographers and a committee of 12 people.

Main achievements: organization of four workshops, teaching photography class, organization of photo expositions and competitions, doubling of the association funds and associates, management of a film photography development laboratory.

CREATIVE & MARKETING DIRECTOR, PROJECT MANAGER
Oct 2016 - Present | Innovation Forum Lausanne (IFL) | Lausanne, Switzerland
In charge of the association creative department, taking care of the creative decisions concerning the main activities (graphics, event organization and advertisement, web marketing).

Graphic and creative support to the global association, based in London, and for the other local branches.

Project manager of the event "Digital photography: how to quantify beauty?". To be held in september 2018.